Universitat Politècnica de Catalunya
Programa de Doctorat en Enginyeria Civil

Departament de Matemàtica Aplicada III

Phase-field modeling of fracture in ferroelectric materials

by Amir Abdollahi

Doctoral Thesis
Advisor: Irene Arias

Barcelona, April 2012

Abstract

Phase-field modeling of fracture in ferroelectric materials

Amir Abdollahi

The unique electro-mechanical coupling properties of ferroelectrics make them ideal materials for use in micro-devices as sensors, actuators and transducers. Nevertheless, because of the intrinsic brittleness of ferroelectrics, the optimal design of the electro-mechanical devices is strongly dependent on the understanding of the fracture behavior in these materials. Fracture processes in ferroelectrics are notoriously complex, mostly due to the interactions between the crack tip stress and electric fields and the localized switching phenomena in this zone (formation and evolution of domains of different crystallographic variants). Phase-field models are particularly interesting for such a complex problem, since a single partial differential equation governing the phase-field accomplishes at once (1) the tracking of the interfaces in a smeared way (cracks, domain walls) and (2) the modeling of the interfacial phenomena such as domain-wall energies or crack face boundary conditions. Such a model has no difficulty for instance in describing the nucleation of domains and cracks or the branching and merging of cracks. Furthermore, the variational nature of these models makes the coupling of multiple physics (electrical and mechanical fields in this case) very natural.

The main contribution of this thesis is to propose a phase-field model for the coupled simulation of the microstructure formation and evolution, and the nucleation and propagation of cracks in single crystal ferroelectric materials. The model naturally couples two existing energetic phase-field approaches for brittle fracture and ferroelectric domain formation and evolution. The finite element implementation of the theory is described. Simulations show the interactions between the microstructure and the crack under mechanical and electro-mechanical loadings. Another objective of this thesis is to encode different crack face boundary conditions into the phase-field framework since these conditions strongly affect the fracture behavior of ferroelectrics. The smeared imposition of these conditions are discussed and the results are compared with that of sharp crack models to validate the proposed approaches. Simulations show the effects of different conditions, electro-mechanical

loadings and media filling the crack gap on the crack propagation and the microstructure of the material. In a third step, the coupled model is modified by introducing a crack non-interpenetration condition in the variational approach to fracture accounting for the asymmetric behavior in tension and compression. The modified model makes it possible to explain anisotropic crack growth in ferroelectrics under Vickers indentation loading. This model is also employed for the fracture analysis of multilayer ferroelectric actuators, which shows the potential of the model for future application. The coupled phase-field model is also extended to polycrystals by introducing realistic polycrystalline microstructures in the model. Inter- and trans-granular crack propagation modes are observed in the simulations. Finally and for completeness, the phase-field theory is extended for the simulation of conducting cracks and some preliminary simulations are also performed in three dimensions. Salient features of the crack propagation phenomenon predicted by the simulations of this thesis are directly compared with experimental observations.

Acknowledgments

First and foremost I offer my sincerest gratitude to my supervisor, Professor Irene Arias, who has supported me throughout my research and thesis with her patience and knowledge whilst allowing me the room to work in my own way. It has been an honor and a privilege to work with her and I am deeply grateful for the opportunity to have done so. I am also truly indebted and thankful to Professor Marino Arroyo for his guidance and support.

I would like to appreciate the faculty of Departament de Matemàtica Aplicada III, in particular Professor Antonio Huerta, who gives me this opportunity to be a member of LaCàN (Laboratori de Càlcul Numèric). My gratitude also goes to Professors Pedro Díez, Antonio Rodríguez and Sonia Fernández for their support. I would also like to thank the reviewers of the thesis and the members of the committee for their useful comments and advice. I humbly acknowledge the assistance of administrative staff Imma, Esther, Àngels and Carmen Lopez and the technical support of David.

It has been a privilege to share so many moments with my officemates and fellow post-graduate students in the group of LaCàN. Among them I want to mention especially Adrian, Daniel, Mohammad, Behrooz, Christian, Kuan, Susanta and Lindaura. I am very grateful for their true friendship and support through the years.

I owe sincere and earnest thankfulness to my family, especially my mother, for their unconditional love, patience, support and encouragement through all my life. Their love has provided me with the enthusiasm to face new projects and constantly seek novel challenges.

The simulations of this thesis have been carried out using the finite element library of the Kratos multi-physics package. I cannot forget to express appreciation to the Kratos team in CIMNE (International Center for Numerical Methods in Engineering), in particular Pooyan, Riccardo and Kazem for their support.

I gratefully acknowledge the support of the Ministerio de Ciencia e Innovación (DPI2007-61054), (DPI2010-19145), and (DPI2011-26589).

Finally, my thanks also go to those who, directly or indirectly, helped me to finish my thesis.

Contents

List of Figures

List of Tables

Thesis body

1 Introduction

Ferroelectric ceramics are prominent materials for micro-sensors, actuators and transducers because of their unique electro-mechanical coupling properties. However, most ferroelectrics exhibit a fracture toughness similar to that of glass, on the order of 1 MPa$\sqrt{m}$. Their inherent brittleness makes them susceptible to fracture. Since practical applications often involve strong mechanical and electrical loading conditions, it is important to understand the fracture behavior of ferroelectric components, and this has been the subject of numerous investigations , see (Zhang and Gao, 2004; Schneider, 2007; Kuna, 2010) for excellent theoretical and experimental reviews. Ferroelectric ceramics exhibit ferroelectric and ferroelastic switching behavior with macroscopic dielectric and butterfly hystereses due to the underlying microscopic mechanisms. The reviews by (Kamlah, 2001; Landis, 2004b; Huber, 2005) present related modeling approaches. The formation and evolution of the microstructure are more probable under high electro-mechanical loadings and near load concentrations such as the vicinity of cracks (Hackemann and Pfeiffer, 2003; Jones et al., 2007; Pojprapai et al., 2011). Nonlinear interactions between the microstructure and the localized stress and electric fields near the crack tip lead to the complexity of fracture in ferroelectric materials (Han et al., 2002; Rajapakse and Zeng, 2001; Beom and Atlurib, 2003; Sheng and Landis, 2007). This suggests that the microscopic phenomena should be taken into account in the analysis of the global reliability of ferroelectric components.

A number of theoretical approaches have been developed to understand fracture phenomena in ferroelectric ceramics. Researchers have proposed approaches based on linear theory of piezoelectricity where microstructure effects are not taken into account. Due to simplicity, these models are useful to study the basic concepts of the linear theory in the context of fracture mechanics and to evaluate the effects of individual and coupled electro-mechanical fields and different crack-face boundary conditions (McMeeking, 1999, 2004; Landis, 2004a; Li et al., 2008). These approaches have been developed to identify the effect of remanent polarization on energy release rates in poled ferroelectrics (Haug and McMeeking, 2006). However the intrinsic nature of ferroelectric materials demands the consideration of the nonlinear microstructure effects in more realistic approaches. These include models inspired in plasticity theory and aimed at polycrystalline ferroelectric ceramics (McMeeking and Landis, 2002). These models do not intend to describe explicitly the domain formation, but rather the effective phenomenology (Landis, 2003; Sheng and Landis, 2007; Wang and

Landis, 2006). Other models rely on a simple local switching criterion (Hwang et al., 1995), which under the assumption of small-scale switching, have allowed researchers to analyze the local phase transformations near the crack tip (Zhu and Yang, 1997; Yang and Zhu, 1998; Zhu and Yang, 1999; Beom and Atlurib, 2003). Recently, phase-field or time-dependent Devonshire-Ginzburg-Landau (TDGL) models are gaining a growing attention. These models explicitly describe the formation and evolution of individual ferroelectric domains in the framework of continuum mechanics (Shu and Bhattacharya, 2001; Zhang and Bhattacharya, 2005a; Schrade et al., 2007; Su and Landis, 2007; Dayal and Bhattacharya, 2007; Xu et al., 2009). Recently, a phase-field model accurately accounting for the stray fields (Yang and Dayal, 2011a) has been proposed. Related models have also been developed in micromagnetics (DeSimone et al., 2001; DeSimone and James, 2002). The nucleation and growth of domains near crack tips have been studied using these microstructural models and the influence on the stress field (Yang and Dayal, 2011b) and the mechanical and electro-mechanical $J-$integrals have been reported (Song et al., 2007; Wang and Zhang, 2007; Wang and Kamlah, 2009; Xu et al., 2010; Li and Landis, 2011; Li and Kuna, 2011). For completeness, we mention that cohesive theories aimed at fracture in ferroelectric materials have also been proposed (Gao et al., 1997; Arias et al., 2006).

Several experiments have been done to study the fracture behavior of ferroelectric ceramics. However there are a number of contradictions and inconsistencies between reported results. Experiments on insulating cracks have shown that a positive electric field promotes crack extension perpendicular to the poling axis of the material, whereas a negative electric field retards it (Tobin and Pak, 1993; Sun and Park, 2000; Lynch, 1998; Schneider and Heyer, 1999). Other tests have indicated an opposite phenomenon, where their results show that a positive applied electric field inhibits crack propagation, whereas crack propagation is enhanced under a negative applied electric field (Wang and Singh, 1997; Shindo et al., 2002; Ricoeur and Kuna, 2003; Jiang et al., 2009). On the other hand, experiments do not show a clear shielding or weakening effect of the microstructure on insulating cracks oriented parallel to the poling and electric field direction (Sun and Park, 2000; Tobin and Pak, 1993). This behavior is not expected since experiments without electric field indicate that in this configuration a pronounced domain switching zone is developed during crack growth (Schneider, 2007). Some experiments have been also performed to investigate the fracture mechanisms of electrically conducting cracks, where the electric field is applied parallel to

the crack orientation and it is able to fracture ferroelectric specimens without additional mechanical load (Fu et al., 2000; Zhang et al., 2004). However it is not understood why the electrical field intensity factors obtained in these works are four times larger than that of reported in the experiments of (Heyer et al., 1998; Gehrig et al., 2008). These contradictions and ambiguities confirm that the fracture of ferroelectric materials is a complex phenomenon and more sophisticated modeling approaches and experiments are required to create a sound basis of results for the understanding of the fracture behavior in these materials.

All of the above mentioned models of ferroelectric fracture consider fixed or stationary crack configurations. With this assumption it is not possible to capture the effects of the microstructure on the crack propagation behavior, specially when the crack tip fields interact with obstacles such as defects or grain boundaries. Recently, a phase-field model (Miehe et al., 2010a; Linder and Miehe, 2012) and a strong discontinuity approach (Rosato et al., 2011) have been proposed to simulate propagating cracks in linear piezoelectric solids, thus not accounting for the effect of ferroelectric domain microstructures. Towards more realistic approaches, we propose a family of coupled phase-field models for both the brittle crack propagation and the microstructure evolution by tackling the full complexity of the fracture phenomenon in ferroelectric materials (Abdollahi and Arias, 2012c,b, 2011a,b). This thesis extends the current state of the art in fracture of ferroelectric ceramics by presenting these models and their developments which are outlined as follows:

1. **Coupled phase-field model.** A coupled phase-field model is proposed based on two existing energetic phase-field approaches for brittle fracture and ferroelectric domain formation and evolution. Using this model, the interactions between the microstructure and the crack propagation are investigated in ferroelectric single crystals under mechanical and electro-mechanical loadings. See Section 3 and Appendix A.

2. **Modeling of different crack-face boundary conditions.** Different electromechanical conditions, introduced as crack-face boundary conditions in sharp models, are encoded into the phase-field framework. The smeared imposition of these conditions are discussed and the results are compared with that of the sharp crack models to validate the proposed approaches. Numerical simulations are performed to show the effects of different conditions, electro-mechanical loadings and media filling the crack gap on the crack propagation and the microstructure of the material. See Section 4 and Appendix B.

3. **Phase-field simulation of anisotropic crack propagation.** The coupled phase-field model is developed by introducing a crack non-interpenetration condition in the variational approach to fracture accounting for the asymmetric behavior in tension and compression. The developed model makes it possible to explain anisotropic crack growth in ferroelectrics under Vickers indentation loading. See Section 5 and Appendix C.

4. **Crack initiation patterns at electrode edges in multilayer actuators.** The phase field model, introduced in Section 5, is employed for the fracture analysis of multilayer ferroelectric actuators. In particular, the objective of this section is to study the crack initiation at electrode edges during the poling process of the actuators. Considering different bonding conditions between the ceramic and electrode layers, different crack initiation patterns are obtained, which are useful to understand the fracture processes and to guide the design of this type of actuators. See Section 6 and Appendix D.

5. **Inter- and trans-granular crack propagation in ferroelectric polycrystals.** The coupled phase-field model is extended to ferroelectric polycrystals. Different polycrystalline microstructures are obtained by implementing a computer simulation of grain growth model. By incorporating the differential fracture toughness of the bulk and the grain boundaries, and the different crystal orientations of the grains, the phase-field fracture model of ferroelectric single crystals is extended to polycrystals. Simulation results show intergranular crack propagation in fine-grain microstructures while transgranular crack propagation is observed in coarse grains. See Section 7 and Appendix E.

6. **Conducting crack propagation driven by electric fields.** The aim of this section is to extend the phase-field theory for the simulation of conducting crack propagation and investigating the crack propagation mechanisms under purely electrical loading. This is done by introducing the electrical enthalpy of a diffuse conducting layer into the phase-field formulation. The results imply that the major driving force to propagate the conducting cracks is the electrostatic force due to the accumulation of charges with the same sign at the crack tip. See Section 8.

7. **Numerical simulations of 3-D crack propagation.** We present some preliminary 3-D simulations of the crack propagation in ferroelectric single crystals. This is done

by extending the phase-field model to three dimensions and running the simulations on a parallel machine. See Section 9.

The structure of this thesis is as follows. The background information regarding the ferroelectric materials and phase-field models is presented in Section 2. Sections 3 - 9 expand on the seven contributions mentioned above. The idea of these sections is to describe concisely the goals of the contribution, provide representative results and conclusions, and refer to (accepted or submitted) papers attached as appendices for the details. In each of these sections the most significant contributions are also highlighted, as well as research ideas emerging from the work performed. Sections 8 and 9 present some preliminary results of conducting crack propagation and 3-D simulations, which are two papers under preparation. The last section is the conclusion of the thesis.

2 Background

2.1 Ferroelectric Materials

Ferroelectrics are a family of multi-phase crystalline materials with exceptional electro-mechanical properties. These materials are classified as a subcategory of piezoelectric materials, possessing dielectric hysteretic behavior. Applications for ferroelectric materials include sensors, capacitors, non-volatile memories, ultrasound imaging and actuators, electro-optic materials for data storage applications, thermistors, switches known as trans-chargers or trans-polarizers, oscillators and filters, light deflectors, modulators and displays (Kanzig, 1957; Lines and Glass, 1979). These materials possess a spontaneous electric polarization below a certain phase transition temperature, called the Curie temperature. This is due to dipoles formed by displacements of charged ions inside the crystal unit cell. Figure 1 presents the unit cell of ferroelectric lead titanate (PbTiO3) with a non-polar cubic symmetry above the Curie temperature. In the room temperature, the central atom of the unit cell (Ti) tends to one of the Oxygen atoms (O), hence stretching the cubic lattice along one of its lattice vectors. This atomic displacement produces a dipole per unit cell, and therefore a spontaneous electrical polarization. If the spontaneous polarization can be reversed by the application of an electric field opposite to its direction, these crystal structures are called ferroelectrics. The polarization can be oriented along six equivalent directions which give rise to six equivalent tetragonal phases in ferroelectrics presented in Fig. 2.

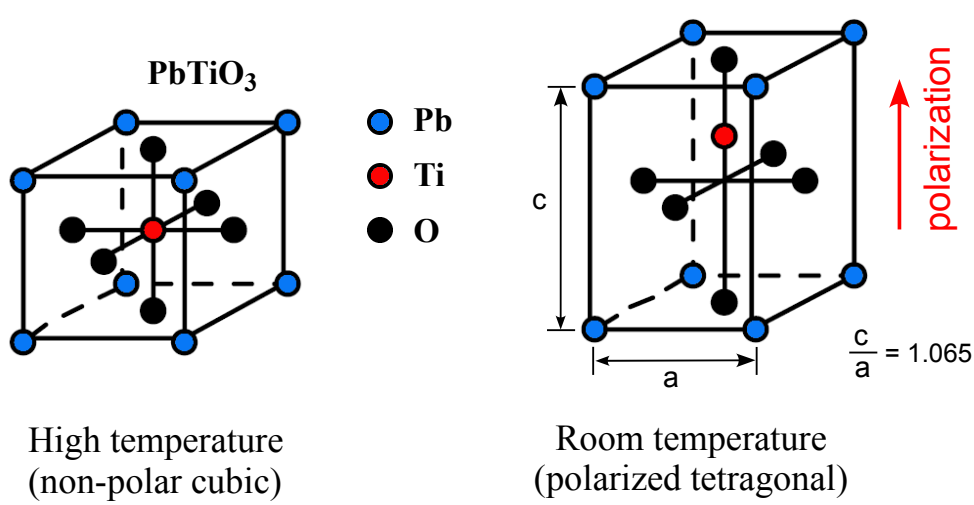

Figure 1: Ferroelectric unit cell in (left) high temperature and (right) room temperature

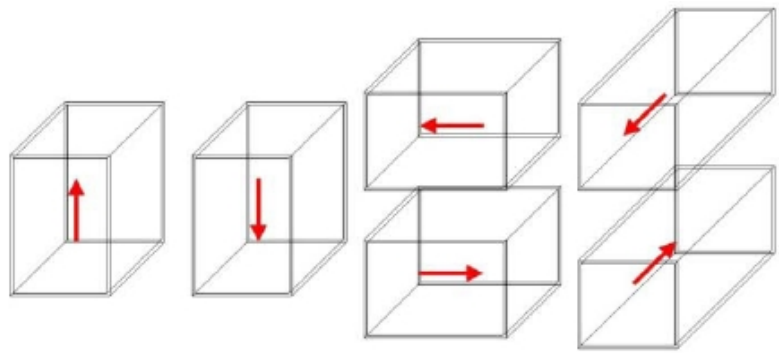

Figure 2: Six equivalent tetragonal phases in ferroelectric crystals.

Application of a small mechanical or electrical load parallel to the polarization elongates the unit cell along the applied load and increases the polarization. In opposite, a small anti-parallel load results in a shrinkage of the unit cell and decreasing the polarization, see Fig. 3. In fact in response to a low applied mechanical load, a ferroelectric material will produce an electric charge proportional to the load. Similarly, the material will produce a mechanical deformation in response to a low applied electric field. These behaviors represent the linear piezoelectric responses of ferroelectric materials under low electrical and mechanical loads.

By increasing the magnitude of the applied load opposite to the polarization, the unit cell is reoriented along other tetragonal phases to accommodate the large load. In the case of a large applied electric field, the polarization of the unit cell is reversed, parallel to the applied field. This polarization reorientation is called 180^o domain switching in ferroelectrics. On the other hand, a large compressive stress reorients the polarization by 90^o, along one of the adjacent tetragonal phases. This phenomenon is defined as 90^o ferroelastic domain switching, see Fig. 4.

A combination of the tetragonal phases form a multi-domain structure of ferroelectric crystals. The boundary separating the phases is classified into 90^o and 180^o domain walls. Figure 5 presents a sample of the multi-domain structure in two dimensions. Application of an external mechanical or electrical load can rearrange this domain pattern through domain switching. In an unpoled ferroelectric material, the polarization of domains is random through the material and it is distributed in such way that the net macroscopic polarization is zero. By applying an electric field, the polarization of domains starts to align along the applied field. If the electric field is strong enough, the material shifts into the polar

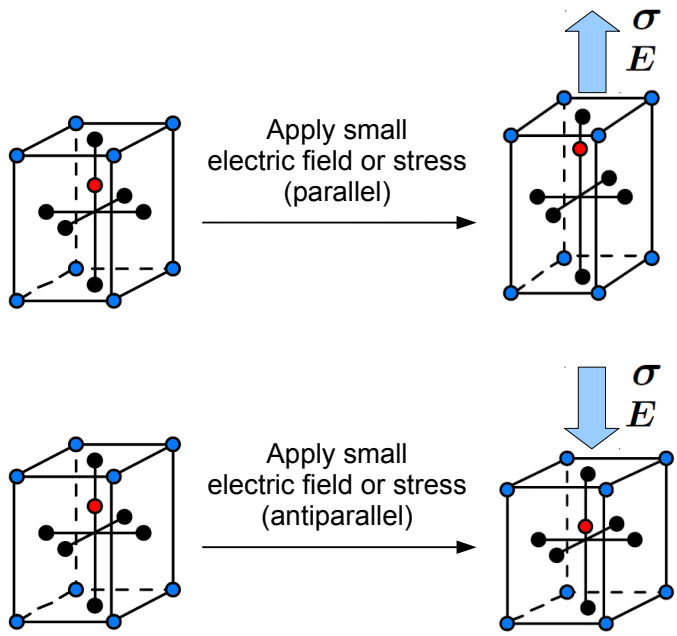

Figure 3: Schematic of the ferroelectric until cell under a small electric field or stress: (top) parallel to the polarization, and (bottom) anti-parallel to the polarization .

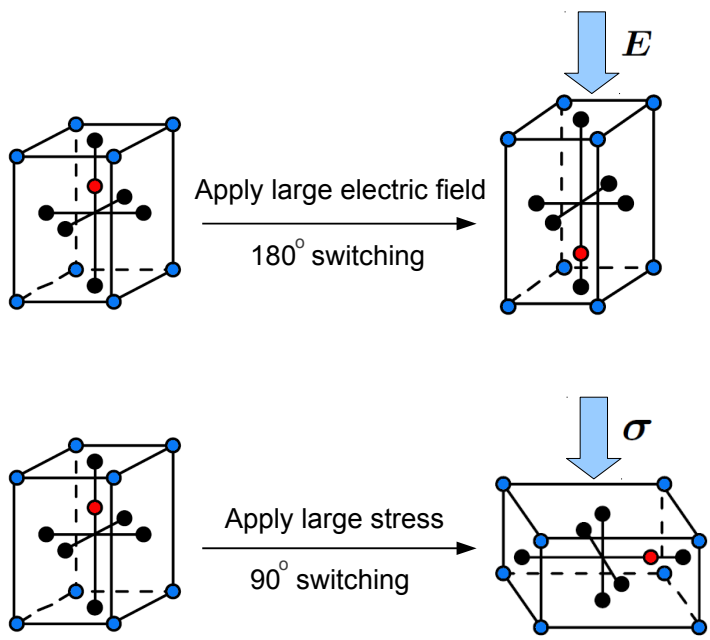

Figure 4: Schematic of 180^0 ferroelectric and 90^0 ferroelastic switching at the unit cell level from large applied electric field and stress.

state. Figure 6 presents the net polarization as a function of the applied electric field. The transition from the unpoled state (point U) to the polar state (point A) is highlighted by the red curve. Point A shows a maximum polarization in the unit cell under a strong applied electric field. When the field is decreased, the polarization decreases and it reaches the remanent polarization $\mathbf{P_r}$ after removal of the electric field.

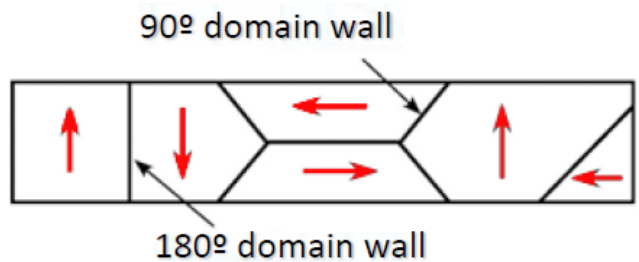

Figure 5: A multi-domain ferroelectric structure in two dimensions.

One consequence of the domain switching in ferroelectric materials is the occurrence of the ferroelectric hysteresis loop and butterfly hysteresis curve depicted in Fig. 6. When a negative electric field is applied (anti-parallel to the polarization), the polarization decreases from the remanent value until a level where the polarization of some domains starts to reverse. A further increase of the field in the negative direction will cause the total reversal of the polarization. The polarization and strain responses in this region are strongly nonlinear. The field necessary to reverse the polarization is called the coercive field with the magnitude of $\mathbf{E_c}$. As the magnitude of the reverse field increases, the polarization reaches another maximum in the opposite direction (point -A). After that, if the field is again reversed, the polarization can be brought back to the previous maximum point depending on the field strength. Considerable changes of the polarization and strain under an alternative electric field are beneficial for many electro-mechanical applications.

2.2 Phase-field models

Phase-field models are powerful tools to deal with moving interface problems (Landau, 1937). Recently, phase-field models have gained a growing interest in physics and materials science, see (Sekerka, 2004; Steinbach, 2009) and references therein. They are also employed in a wide range of applications in applied science and engineering such as fracture (Francfort and Marigo, 1998; Miehe et al., 2010b), growth of thin films (Ratz et al., 2006) and grain

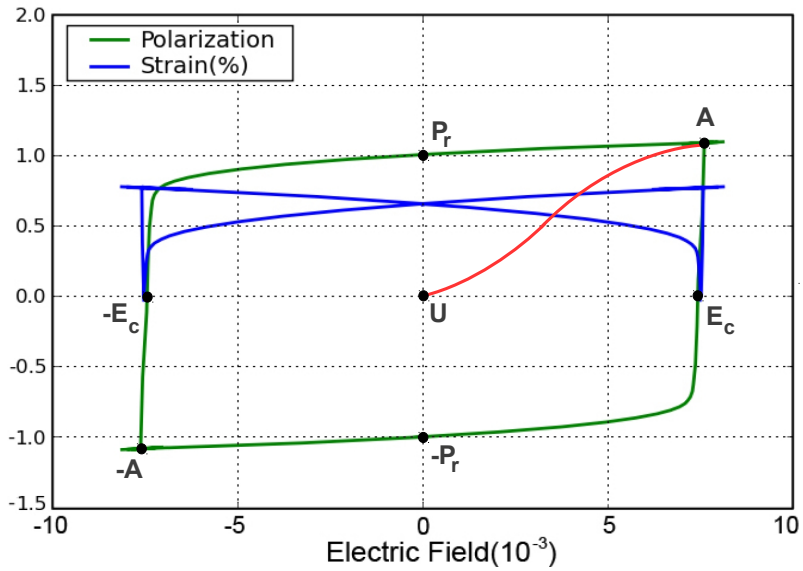

Figure 6: Hysteresis loop (Polarization-Electric field) and butterfly hysteresis curve (Strain-Electric field) in poled ferroelectrics. The red curve indicates the transition from the unpoled state (point U) to the polar state (point A).

structures (Krill and Chen, 2002), image segmentation (Benes et al., 2004), vesicle biomembranes (Wang, 2005) and multi-phase flows (Jacqmin, 1999), to mention a few. This thesis also presents another application of phase-field models for microstructure formation and fracture evolution in ferroelectric materials (Abdollahi and Arias, 2012c,b, 2011a,b).

The idea behind phase-field modeling is to replace the sharp description of the interface by a smeared continuous layer. For this purpose, an auxiliary field, called order parameter or phase-field variable, is introduced to represent the phases (e.g. inside and outside of the crack), and also the interface. The phase-field variable adopts distinct values, say 0 and 1, in each of the phases, and smoothly varies between these values in the diffuse interface, see Fig. 7. This approach is also called diffuse-interface modeling.

Phase-field models are typically defined by an energy functional associated with different energy terms based on the physics of the problem. A general energy function E for these models can be constructed as

$$E[\boldsymbol{\eta}, \boldsymbol{\vartheta}] = F_1(\nabla \boldsymbol{\eta}) + F_{11}[\boldsymbol{\eta}, \boldsymbol{\vartheta}] \tag{1}$$

where $\boldsymbol{\eta}$ is the order parameter and $\boldsymbol{\vartheta}$ represents a set of physical variables in the problem

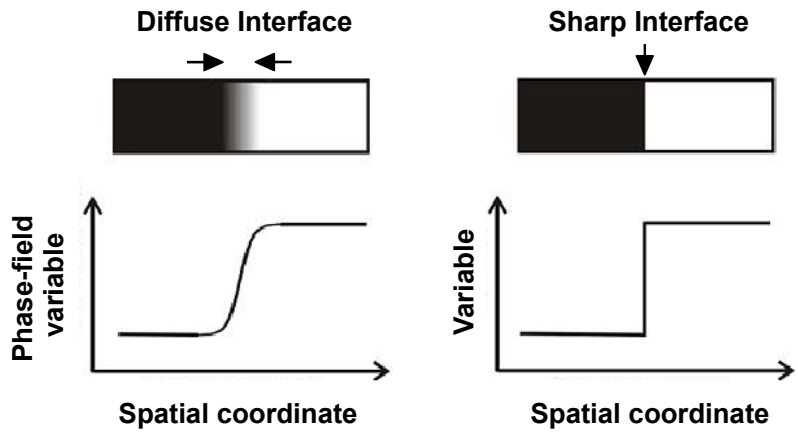

Figure 7: Illustration of a (left) diffuse and (right) sharp interface.

under consideration. Function F_1 is the common energy term in the phase-field models associated with the gradient of the order parameter. This function penalizes sharp variations in the order parameter, hence introducing the interfacial energy between the phases. A positive regularization constant regulates the size of the interface in this energy term. Function F_{11} characterizes the physical properties of the phases and it is associated with the order and physical parameters of the problem. In general, this energy furnishes a multi-well energy landscape with respect to the order parameter $\boldsymbol{\eta}$ with minima corresponding to the phases. Figure 8 presents a schematic of this energy landscape where m indicates the number of phases. This number can be one in single-phase problems such as fracture (Francfort and Marigo, 1998; Miehe et al., 2010b) or it can be as high as 100 in the model of grain growth in polycrystalline materials (Krill and Chen, 2002).

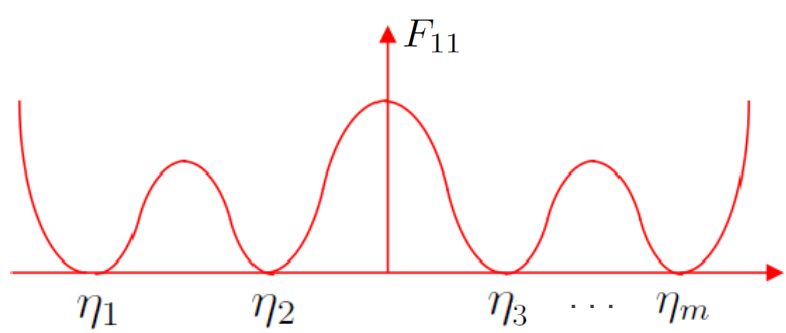

Figure 8: Schematic of a multi-well energy landscape.

In complex moving interface problems such as fracture in ferroelectric ceramics, phase-field models are particularly interesting since a single partial differential equation governing the phase-field accomplishes at once (1) the tracking of the interfaces in a smeared way (cracks, domain walls) and (2) the modeling of the interfacial phenomena such as domain-wall energies or crack-face boundary conditions. Furthermore, the variational nature of these models makes the coupling of multiple physics very natural. Such a model has no difficulty in describing the nucleation of domains and cracks, and tracking the evolution of the domain boundaries and crack tips. This flexibility comes at the expense of a high computational cost, since the width of the phase-field regularizations of the domain wall and the crack must be resolved by the discretization for an accurate approximation of the sharp-interface model. Furthermore, the specific interface boundary or jump conditions under consideration must be encoded into the phase-field framework.

2.3 Phase-field model for ferroelectric single crystals

In the field of ferroelectric materials, given the extreme difficulty of tracking the interfaces (the domain walls) explicitly with a sharp interface model, phase-field models are the current standard models for simulations of microstructure formation and evolution. According to these models, the Helmholtz free energy density of a ferroelectric material is stated as (Zhang and Bhattacharya, 2005a; Su and Landis, 2007)

$$\psi(\boldsymbol{\varepsilon}, \boldsymbol{p}, \nabla \boldsymbol{p}, \boldsymbol{D}) = U(\nabla \boldsymbol{p}) + W(\boldsymbol{p}, \boldsymbol{\varepsilon}) + \chi(\boldsymbol{p}) + \frac{1}{2\varepsilon_0}(\boldsymbol{D} - \boldsymbol{p}) \cdot (\boldsymbol{D} - \boldsymbol{p}), \tag{2}$$

where $\boldsymbol{\varepsilon}$ is the strain tensor associated with the mechanical displacement $\boldsymbol{u}$, $\boldsymbol{\varepsilon} = 1/2(\nabla \boldsymbol{u} + \nabla^T \boldsymbol{u})$, $\boldsymbol{p}$ is the polarization, U is the domain wall energy density penalizing sharp variations in the polarization, χ is the phase separation potential, and W is the electroelastic energy density. These two last energy densities penalize deviations from the spontaneous polarizations and strains of the material, hence introducing the anisotropy and nonlinearity of ferroelectric materials. The first three terms in Eq. (2) indicate the free energy of the material. The last term is the free energy of the free space occupied by the material or the depolarization energy density (Li, 2009). It involves the polarization and the electric displacement $\boldsymbol{D} = \boldsymbol{p} - \varepsilon_0 \nabla \phi$, where ϕ is the electric potential and ε_0 is the permittivity of free space. Following a Legendre transformation, the electro-mechanical enthalpy density

$\mathcal{H}$ is obtained (Su and Landis, 2007)

$$\begin{aligned}\mathcal{H}(\boldsymbol{\varepsilon}, \boldsymbol{p}, \nabla \boldsymbol{p}, \boldsymbol{E}) &= \min_{\boldsymbol{D}} \left[\psi(\boldsymbol{\varepsilon}, \boldsymbol{p}, \nabla \boldsymbol{p}, \boldsymbol{D}) - \boldsymbol{E} \cdot \boldsymbol{D}\right] \\ &= U(\nabla \boldsymbol{p}) + W(\boldsymbol{p}, \boldsymbol{\varepsilon}) + \chi(\boldsymbol{p}) - \frac{\varepsilon_0}{2}|\boldsymbol{E}|^2 - \boldsymbol{E} \cdot \boldsymbol{p},\end{aligned} \tag{3}$$

where $\boldsymbol{E}$ is the electric field defined as $\boldsymbol{E} = -\nabla\phi$. The stresses and electric displacements are derived from the electrical enthalpy as $\boldsymbol{\sigma} = \partial\mathcal{H}/\partial\boldsymbol{\varepsilon}$ and $\boldsymbol{D} = -\partial\mathcal{H}/\partial\boldsymbol{E}$. The energy functions U, W and χ in Eq. (3) are chosen following (Devonshire, 1949, 1951), adapted to a plane polarization and plane strain state:

$$U(p_{i,j}) = \frac{a_0}{2}(p_{1,1}^2 + p_{1,2}^2 + p_{2,1}^2 + p_{2,2}^2), \tag{4}$$

$$\begin{aligned}W(p_i, \varepsilon_{jk}) = &-\frac{b_1}{2}(\varepsilon_{11}p_1^2 + \varepsilon_{22}p_2^2) - \frac{b_2}{2}(\varepsilon_{11}p_2^2 + \varepsilon_{22}p_1^2) - b_3(\varepsilon_{21} + \varepsilon_{12})p_1p_2 \\ &+ \frac{c_1}{2}(\varepsilon_{11}^2 + \varepsilon_{22}^2) + c_2\varepsilon_{11}\varepsilon_{22} + \frac{c_3}{2}(\varepsilon_{12}^2 + \varepsilon_{21}^2),\end{aligned} \tag{5}$$

$$\begin{aligned}\chi(p_i) = &\alpha_1(p_1^2 + p_2^2) + \alpha_{11}(p_1^4 + p_2^4) + \alpha_{12}(p_1^2p_2^2) + \alpha_{111}(p_1^6 + p_2^6) + \alpha_{112}(p_1^2p_2^4 + p_2^2p_1^4) \\ &+ \alpha_{1111}(p_1^8 + p_2^8) + \alpha_{1112}(p_1^6p_2^2 + p_2^6p_1^2) + \alpha_{1122}(p_1^4p_2^4),\end{aligned} \tag{6}$$

where the combination of energy functions χ and W is the total Landau-Devonshire energy density, a_0 is the scaling parameter of the domain wall energy, $b_i (i = 1, 2, 3)$ are the constants of the coupling terms between strain and polarization and $c_i (i = 1, 2, 3)$ are the elastic constants. The coupling constants $b_i (i = 1, 2, 3)$ are obtained by fitting the spontaneous strains of the tetragonal phase relative to the cubic phase. The phase separation energy χ is improved by adding the eighth-order terms with coefficients α_{1111}, α_{1112} and α_{1122} to reproduce the dielectric behavior of barium titanate ($BaTiO_3$) single crystals (Li et al., 2005; Wang et al., 2007). The eighth-order term with coefficient α_{1122} enables the model to fit the dielectric constants while retaining a reasonable energy barrier for 90^0 domain switching in the tetragonal phase (Zhang and Bhattacharya, 2005a). α_1 is linearly dependent on temperature and its negative value makes the cubic phase unstable. α_{111} is estimated by

fitting the spontaneous polarization of the tetragonal phase. α_{112} and α_{1112} are fitted to the dielectric permitivity perpendicular to the spontaneous polarization. α_{11}, α_{12} and α_{1111} are evaluated from linear and nonlinear dielectric measurements above the Curie temperature (Wang et al., 2007).

For convenience, dimensionless variables are selected through the following normalizations: $x_i' = x_i\sqrt{c_0/a_0}/p_0$, $p_i' = p_i/p_0$, $t' = tc_0/\mu p_0^2$, $\varepsilon_0' = \varepsilon_0 c_0/p_0^2$, $\phi' = \phi/\sqrt{a_0 c_0}$, $\alpha_1' = \alpha_1 p_0^2/c_0$, $\alpha_{11}' = \alpha_{11}p_0^4/c_0$, $\alpha_{12}' = \alpha_{12}p_0^4/c_0$, $\alpha_{111}' = \alpha_{111}p_0^6/c_0$, $\alpha_{112}' = \alpha_{112}p_0^6/c_0$, $\alpha_{1111}' = \alpha_{1111}p_0^8/c_0$, $\alpha_{1112}' = \alpha_{1112}p_0^8/c_0$, $\alpha_{1122}' = \alpha_{1122}p_0^8/c_0$, $b_i' = b_i p_0^2/c_0$ and $c_i' = c_i/c_0$, where i = 1,2,3. The constants are chosen to fit the behavior of single crystals of barium titanate ($BaTiO_3$) at room temperature, taking c_0 = 1 GPa, a value for the spontaneous polarization of p_0=0.26 C/m^2, the relative spontaneous strains ε_a = -0.44% along a-axis and ε_c = 0.65% along c-axis (Zhang and Bhattacharya, 2005a; Wang et al., 2007). The domain wall scaling parameter is set to $a_0 = 3.7 \times 10^{-9}\mathrm{Vm^3C^{-1}}$ which leads to the value of 0.5 nanometer for the normalized unit length $\Delta x' = 1$. The normalized parameters are presented in Table 1.

Table 1: Normalized parameters

c_1'	c_2'	c_3'	b_1'	b_2'	b_3'	α_1'	α_{11}'
185	111	74	1.4282	-0.185	0.8066	-0.0023	-0.0029

α_{12}'	α_{111}'	α_{112}'	α_{1111}'	α_{1112}'	α_{1122}'	ε_0'
-0.0011	0.003	-0.00068	0.001	0.0093	1.24	0.131

With the selected parameters, the normalized Landau-Devonshire energy is presented in Fig. 9 as a function of the normalized polarization p_1' and p_2', for a stress-free state ($\sigma_{ij} = 0$). Positive values of the energy are truncated to zero in the plot, to highlight the energy landscape near the minima. The four minima in Fig. 9 correspond to the four variants of the tetragonal phase with normalized polarization p' = (1,0),(0,1),(-1,0) and (0,-1).

2.4 Phase-field model for brittle fracture

To analyze quasi-static brittle fracture, we consider a variational regularized model of Griffith's fracture that admits a straightforward numerical implementation (Francfort and Marigo, 1998; Bourdin et al., 2000; Bourdin, 2007; Bourdin et al., 2008; Amor et al., 2009). This model and its numerical discretization allows naturally for crack nucleation, branching, and interaction between multiple cracks. It smears the crack in contrast with cohesive

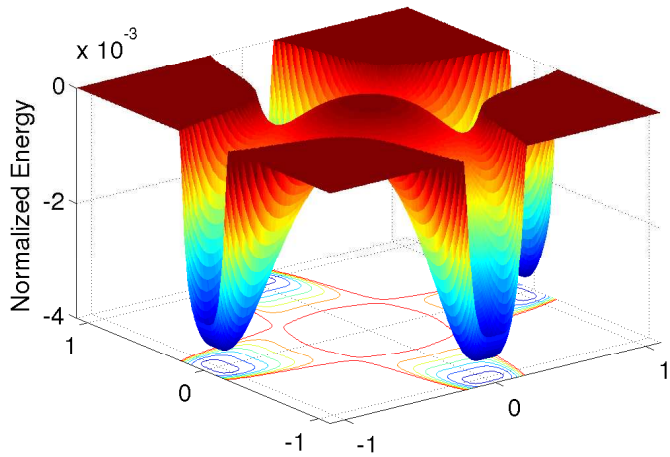

Figure 9: Normalized Landau-Devonshire energy density as a function of the normalized polarization components p_1' and p_2' in a stress-free state. Positive values are truncated to zero for clarity.

methods (Xu and Needleman, 1994; Camacho and Ortiz, 1996) and other sharp crack models such as the extended finite element method (XFEM) (Moes et al., 1999) and the strong discontinuity approach (Oliver et al., 2002). If the mesh is sufficiently fine, the method used here is mesh independent, and it avoids difficulties of XFEM approaches to fracture, notably nucleation and branching. These difficulties have been tackled combining XFEM with damage models (Belytschko et al., 2003).

Following (Bourdin et al., 2000), we adopt a variational regularized view of Griffith's fracture theory. The total energy of a body made of brittle material and occupying a region Ω is written as:

$$E_\kappa[\boldsymbol{u}, v] = \int_\Omega (v^2 + \eta_\kappa) F(\boldsymbol{\varepsilon}(\boldsymbol{u}))\, \mathrm{d}\Omega + G_c \int_\Omega \left[\frac{(1-v)^2}{4\kappa} + \kappa |\nabla v|^2 \right] \mathrm{d}\Omega - \int_{\Gamma_{N,\boldsymbol{u}}} \boldsymbol{t} \cdot \boldsymbol{u}\, \mathrm{d}S, \quad (7)$$

where F is the elastic potential as a function of the strain $\boldsymbol{\varepsilon}$, and G_c is the critical energy release rate or the surface energy density in Griffith's theory (Griffith, 1921). The elastic potential F is the stored energy density as a result of deformation of an elastic body. For a linear elastic material, this potential is a quadratic function of the strain, i.e. $F(\boldsymbol{\varepsilon}(\boldsymbol{u})) = \frac{1}{2}\boldsymbol{\varepsilon}(\boldsymbol{u}) : \boldsymbol{C} : \boldsymbol{\varepsilon}(\boldsymbol{u})$, where $\boldsymbol{C}$ is the elastic stiffness tensor. The scalar field v provides a diffuse representation of the fracture zone, κ is a positive regularization constant to regulate the size

of the fracture zone and η_κ is a small (relative to κ) residual stiffness to avoid the singularity of the first part of the energy in fully fractured regions of the domain. Natural boundary conditions are adopted for v. This functional is minimized in subsequent load increments, imposing additionally an irreversibility condition, namely that the field v (informally, a measure of the integrity of the material) can only decrease at any point in space during the incremental process. The minimizers of the total energy develop localized features, in particular localized regions with low or zero values of v, where the smeared crack is located.

It has been shown that, as long as η_κ converges to zero faster than κ, this regularized theory converges to the sharp theory of brittle fracture. Furthermore, it has been shown that the finite element discretization of this theory converges to Griffith's fracture theory when the mesh size and κ tend to zero in a concerted manner (Bourdin et al., 2008; Amor et al., 2009)

The scalar field v is the phase-field parameter describing a smooth transition in space between unbroken ($v = 1$) and broken ($v = 0$) states of the material. By noting that v^2 multiplies the elastic potential F, it is clear that the value $v = 0$ effectively reduces the stiffness of the material to zero. When the regularization parameter κ tends to zero, this transition becomes sharper. It can be seen that in the limit of vanishingly small regularization parameter, the phase-field model exhibits traction-free solutions on the crack faces, as expected in the sharp crack model. For a finite but small value of the regularization parameter, as used in practical computations, the resulting solutions are very close to being traction-free in the smeared crack. For ferroelectric materials, similar conditions can also be considered for the electrical fields, as discussed in Section 3.

The first term in Eq. (7) can be interpreted as the bulk stored elastic energy, while the second takes the role of the surface energy. The crack propagation results from the competition between these two energy terms. When the elastic energy density F increases close to a critical value in a given region, it may become energetically favorable for the system to decrease the value of v towards zero in that region in order to release elastic energy. This comes at the expense of increasing the second term in the energy, since deviations from 1 are penalized. It is understandable then that the optimal solutions will release elastic energy by forming narrow regions of small values of v. However, since variations of v are also penalized in this second term, this model produces smeared cracks, whose width is governed by the regularization parameter κ. The critical value for the elastic energy density

is the energy level required to overcome the surface energy and to develop the fracture zone. By increasing the value of the critical energy release rate G_c of the material, the surface energy increases proportionally and it consequently requires a higher value of the elastic energy density to nucleate or propagate cracks. It can be checked mathematically that the integrand of the surface energy term converges to the surface area of the crack when κ tends to zero, as expected in the sharp interface model. For a finite but small value of κ, as used in practical computations, the second term will be a good approximation of the surface area of the smeared crack.

An illustration of the diffuse crack is presented in Fig. 10. This figure is obtained from the minimizer of the surface energy in two dimensions which is an optimal profile as a function of v and a point x on the crack. Consider a line orthogonal to the crack and passing through x with a distance function of $d(x)$, then this profile is stated as (Bourdin et al., 2008)

$$v_\kappa(x) := \begin{cases} 0 & \text{if } d(x) \leq \alpha \\ \\ 1 - \exp(-\frac{d(x)-\alpha}{2\kappa}) & \text{otherwise,} \end{cases} \tag{8}$$

where 2α indicates the fully fractured region where $v = 0$. The semicircular area in front of the crack is obtained by considering a distance function of $d(r)$ along the radius of the circle r. The resulting contour in Fig. 10 initializes the scalar field v and introduces a pre-crack as an internal layer in a test specimen. This is in contrast to the sharp-crack models, where the crack faces are geometrically defined in the computational model. The diffuse pre-cracks are used to control and facilitate crack initiation and to determine energy release rates.

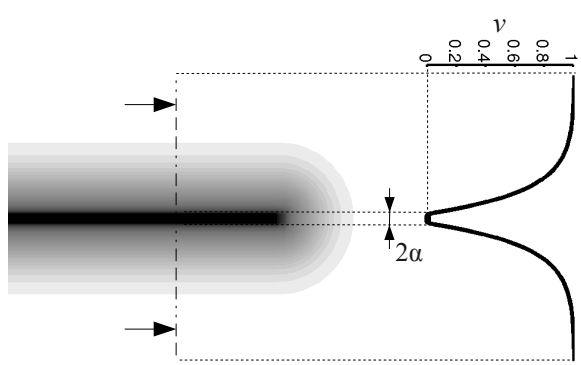

Figure 10: A sample of the smeared crack using the profile in Eq. (8).

The total energy in Eq. (7) is quadratic and convex in v and $\boldsymbol{u}$ separately. In fact, for a fixed v or $\boldsymbol{u}$, the minimizer of either $E_\kappa(\boldsymbol{u}, \bullet)$ or $E_\kappa(\bullet, v)$ exists, is unique, and can be efficiently computed solving a linear system of equations, with the appropriate boundary conditions. As a consequence, the numerical implementation of this theory is straightforward by means of an iterative algorithm of two minimizers in subsequent load increments. For each load increment, the iterations continue until the field v reaches a steady state. An irreversibility condition is also imposed in this algorithm, namely that the field v can only decrease at any point in space during the incremental process (Bourdin, 2007; Bourdin et al., 2008).

3 Coupled phase-field model of fracture in ferroelectric single crystals

To study the quasi-static crack propagation in ferroelectric materials, we propose a phase-field model which couples two energetic phase-field approaches for ferroelectric domain formation and evolution and brittle fracture, summarized in Sections 2.3 and 2.4, respectively. The coupling is done by forming a total electro-mechanical enthalpy that includes the enthalpy of a possibly fractured ferroelectric material, together with the fracture surface energy. From a physical point of view, the presence of the crack affects only some of the contributions to the electro-mechanical enthalpy density $\mathcal{H}$ in Eq. (3). The coupling between the field v representing the crack and the other fields depends on the particular electrical and mechanical boundary conditions adopted for the crack. Note that in the phase-field model, these boundary conditions become part of the field equations since the crack faces are represented by an internal layer. By way of example, most of the crack models assume that the crack faces are mechanically traction-free, i.e. $\boldsymbol{\sigma} \cdot \boldsymbol{n} = 0$ on the crack faces, $\boldsymbol{n}$ being the unit outward normal. This condition is satisfied in the phase-field model for brittle fracture by multiplying the elastic energy density F by the jump set function $(v^2 + \eta_\kappa)$ (see Eq. (7)). Working by analogy, in the case of the proposed electro-mechanical model, we multiply the electro-elastic energy density W in Eq. (3), which involves the elastic strains in all its terms, by the jump set function. We illustrate in Section 4 that indeed this method produces numerical solutions satisfying the traction-free boundary conditions at the crack faces in an approximate but accurate way for a small yet finite value of the regularization parameter.

When it comes to the electrical boundary conditions, there are two classical extreme assumptions, namely permeable and impermeable boundary conditions. The former assume that crack faces are closed and the electric field is not perturbed by the presence of the crack. In order to encode these conditions in the phase-field model, the last two terms in the electro-mechanical enthalpy density $\mathcal{H}$ in Eq. (3), which involve the electric field $\boldsymbol{E}$, should remain unmodified. In addition, free-polarization boundary conditions (Vendik and Zubko, 2000) are commonly assumed, implying that the gradients normal to the crack faces of the polarization components vanish at the crack faces. In the phase-field framework, we introduce this condition by multiplying the only term in $\mathcal{H}$ involving the gradient of

polarization, i.e. the domain wall energy density U, by the jump set function $(v^2+\eta_\kappa)$. The phase separation energy χ is not modified since it does not involve gradients of polarization. Besides, note that modifying also the phase separation energy would lead to an indeterminacy of the polarization inside the fracture zone. See Section 4 for mathematical description of different crack-face boundary conditions.

In summary, for a *traction-free, electrically permeable*, and *free-polarization* crack, the electro-mechanical enthalpy density $\mathcal{H}$ follows

$$\mathcal{H}(\boldsymbol{\varepsilon}, \boldsymbol{p}, \nabla\boldsymbol{p}, \boldsymbol{E}, v) = (v^2+\eta_\kappa)\left[U(\nabla\boldsymbol{p}) + W(\boldsymbol{p}, \boldsymbol{\varepsilon})\right] + \chi(\boldsymbol{p}) - \frac{\varepsilon_0}{2}|\boldsymbol{E}|^2 - \boldsymbol{E}\cdot\boldsymbol{p} \tag{9}$$

where $(v^2+\eta_\kappa)W + \chi$ is the modified Landau-Devonshire energy.

In the other extreme case, impermeable boundary conditions were proposed to define an open and electrically defective crack by assuming zero permittivity for the crack gap (Deeg, 1980). In this model, the crack faces are treated as charge-free surfaces, i.e. the normal component of the electric displacement vanishes on both crack faces. In contrast to the permeable crack, the impermeable crack does not sustain any electric displacement inside the fractured zone ($v = 0$) and thus the last two terms of the electro-mechanical enthalpy density $\mathcal{H}$ in Eq. (3) are multiplied by the jump set function $(v^2+\eta_\kappa)$ accordingly. Numerical results in Section 4 indicate that indeed the desired boundary condition on the crack faces is obtained with this method. Thus, for a *traction-free, electrically impermeable*, and *free-polarization* crack, the electro-mechanical enthalpy density $\mathcal{H}$ takes the form

$$\mathcal{H}(\boldsymbol{\varepsilon}, \boldsymbol{p}, \nabla\boldsymbol{p}, \boldsymbol{E}, v) = (v^2+\eta_\kappa)\left[U(\nabla\boldsymbol{p}) + W(\boldsymbol{p}, \boldsymbol{\varepsilon}) - \frac{\varepsilon_0}{2}|\boldsymbol{E}|^2 - \boldsymbol{E}\cdot\boldsymbol{p}\right] + \chi(\boldsymbol{p}) \tag{10}$$

For both crack models, the total electro-mechanical enthalpy for a ferroelectric body occupying a region Ω is then

$$\begin{aligned} H[\boldsymbol{u}, v, \boldsymbol{p}, \phi] &= \int_\Omega \mathcal{H}(\boldsymbol{\varepsilon}(\boldsymbol{u}), \boldsymbol{p}, \nabla\boldsymbol{p}, \boldsymbol{E}(\phi), v)\ \mathrm{d}\Omega \\ +G_c\int_\Omega \left[\frac{(1-v)^2}{4\kappa} + \kappa|\nabla v|^2\right]\ \mathrm{d}\Omega &- \int_{\Gamma_{N,\boldsymbol{u}}} \boldsymbol{t}\cdot\boldsymbol{u}\ \mathrm{d}S + \int_{\Gamma_{N,\phi}} \omega\phi\ \mathrm{d}S. \end{aligned} \tag{11}$$

where the electro-mechanical enthalpy density $\mathcal{H}$ is given for permeable and impermeable cracks in Eqs. (9) and (10), respectively. The form of the variations of the electro-mechanical enthalpy along with a simple algorithm to solve the coupled system are presented in Ap-

pendix A.

To perform numerical simulations, a rectangular domain is considered and a monotonically increasing mechanical load is applied by pulling the top and bottom sides of the model with a uniform vertical mechanical displacement. The four snapshots of the evolution of the microstructure and the crack are presented in Fig. 11. By increasing the load, domain switching propagates through the whole sample and the formation of multiple twins is obvious in Fig. 11(b). To evaluate the effect of twinning on the crack propagation, the evolution of the total surface energy is presented in Fig. 12 as a function of the load step. The graph of the permeable model is marked with letters **a** - **d** which correspond to four snapshots presented in Fig. 11. The surface energy graph is also obtained for a single-phase material by running the simulation with a frozen polarization field, which can be viewed as a reference to be compared with the multi-phase model and assess the effect of twinning.

Multi-phase models show a slower growth rate than the single-phase one in Fig. 12. This deviation is attributed to the retarding effect on the crack propagation of the 90^o ferroelastic domain switching in the vicinity of the crack tip. This toughening mechanism is also reported in experiments of crack propagation in $BaTiO_3$ (Meschke et al., 1997, 2000). A sequence of abrupt crack propagation events, subsequent crack arrest, and slow crack propagation periods can also be observed in Fig. 12. These stages reflect the following sequence of events. As the crack cuts a set of twins, it can propagate easily until it feels the compressive stresses of the next set of twins ahead of the tip, and it is arrested. Subsequently, it propagates slowly until the loading is high enough to overcome the compressive stresses due to the twins, and the process repeats itself. The snapshots in Fig. 11(b)-(d) correspond to slow propagation periods arrested by the twins ahead of the crack represented with bold white arrows. The corresponding points **b** - **d** in Fig. 12 indicate the starting points of the slow propagation periods. It is noteworthy that the experimental results in Fang et al. (2007) show a similar slow-fast crack propagation behavior in a poled $BaTiO_3$ single crystal specimen under mechanical loading.

Electro-Mechanical Loading. Simulations are also performed under combined electro-mechanical loading. The behavior of the system is more complex in this case, since the electric field influences the size and position of the twins, as well as the polarization intensity. Our simulation results show that, by increasing the magnitude of the electric field, the coercive stress σ_c for 90^o ferroelastic domain switching increases and twinning becomes more

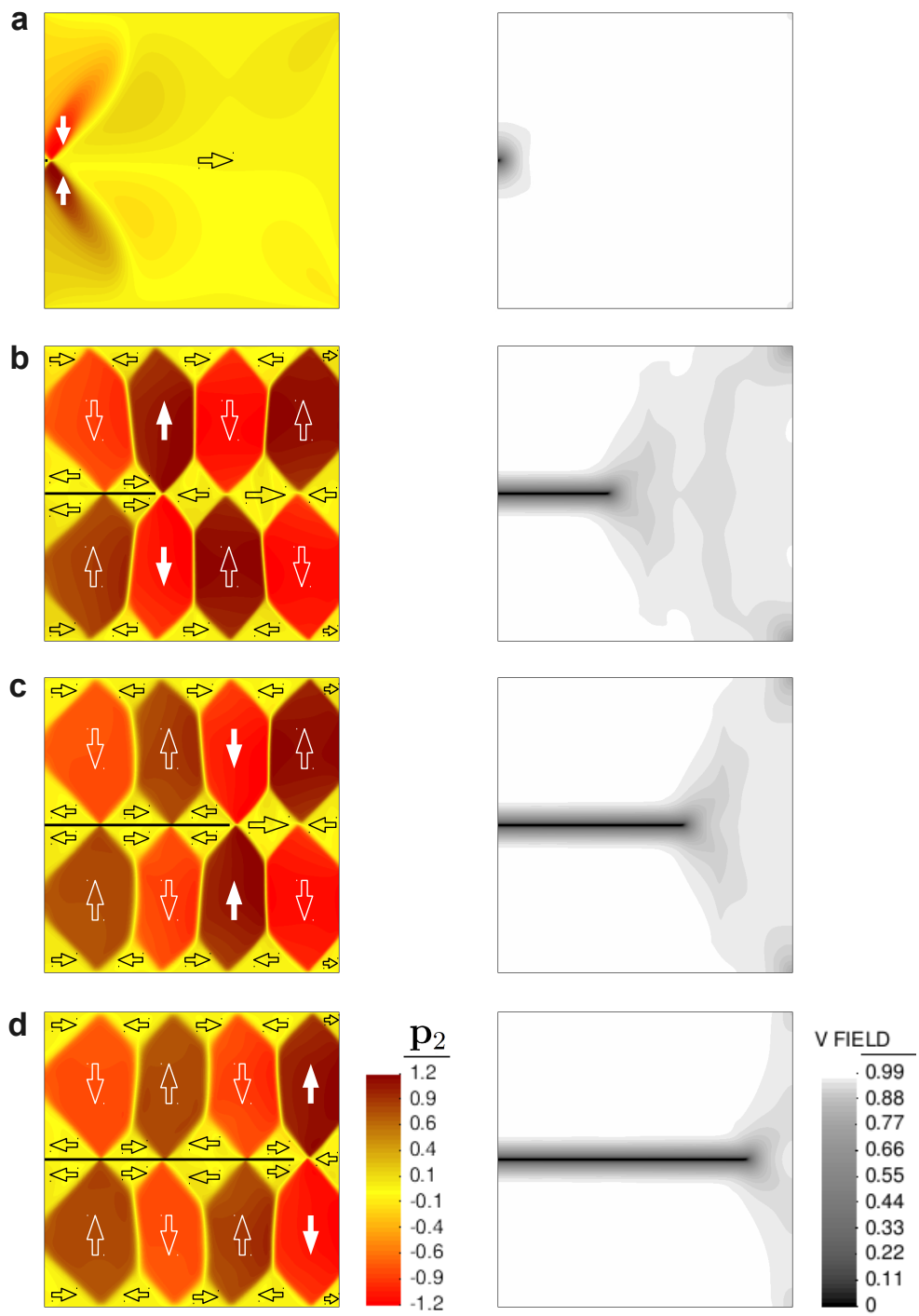

Figure 11: Four snapshots of the evolution of the microstructure and the permeable crack. The left column shows the vertical polarization field $\boldsymbol{p}_2$, which highlights the domain structure, and the right column shows the field v representing the fractured area. Domain orientations are indicated with large arrows, which are bold white for the twins ahead of the crack. The points where $v = 0$ are represented in black in the polarization maps to show the crack position.

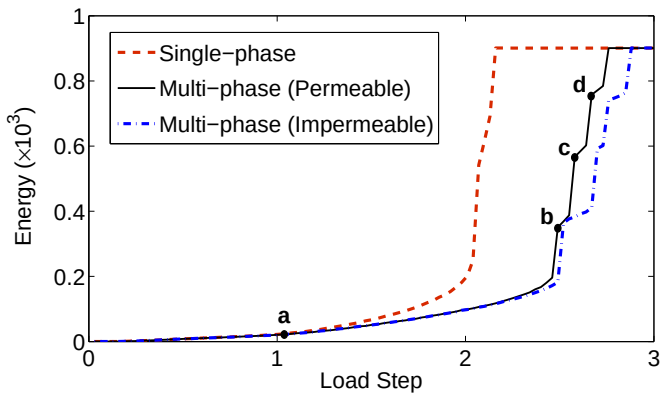

Figure 12: Evolution of the normalized surface energy as a function of the load step.

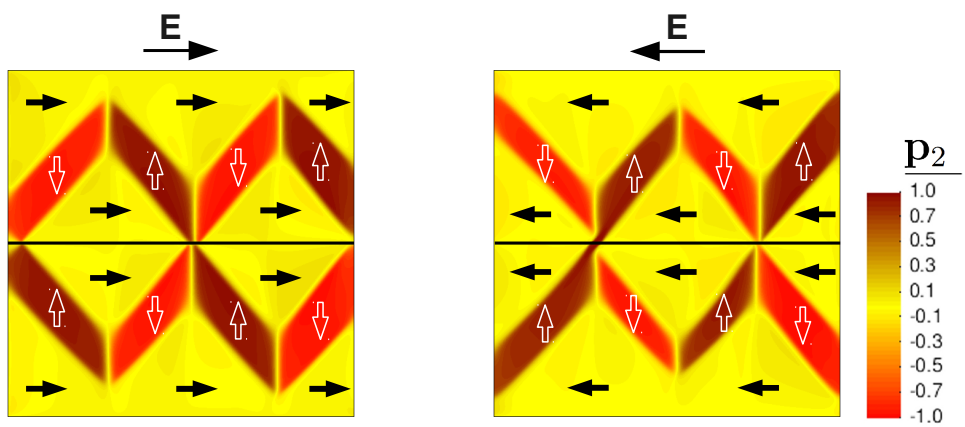

(a) (b)

Figure 13: Twinning in the permeable crack model under electro-mechanical loading (a) positive (b) negative electric fields. The black line shows the crack path and the bold black arrows indicate the domains aligned with the applied electric field.

difficult. A physical consequence is the gradual shrinking of the twins, de-twinning, ahead of the crack. An illustration of the twins forming under positive and negative electric fields is shown in Fig. 13. It is apparent from this figure that the vertical twins (white arrows) decrease in size with respect to Fig. 11(d), while the horizontal domains (bold black arrows), which align as much as possible with the applied electric field, are significantly larger. Due to the de-twinning effect, the crack splits the model under a lower load and the effective fracture toughness decreases approaching the single-phase model.

Contributions

We summarize here the most significant contributions of this work, which has been published as a research paper in (Abdollahi and Arias, 2011a):

1. A phase-field model is presented for the coupled nucleation and evolution of cracks and domains in ferroelectric materials. The model naturally couples two energetic phase-field models for fracture and for the microstructure of such materials. The simulations reported here are, to the best of our knowledge, the first calculations for the fully coupled interaction between the crack propagation and the formation and evolution of microstructure in ferroelectric materials.

2. We reproduce experimental observations, such as the slow-fast crack propagation due to the formation of twins in the vicinity of the crack tip (Fang et al., 2007) and the weakening effect of de-twinning for high magnitudes of applied electric field (Schneider and Heyer, 1999).

3. Our simulations reveal a wealth of complex phenomena, for which competing effects make it difficult to interpret the experimental record. In particular, the simulations explain why for low applied electric fields below the coercive field, there is not a clear shielding or weakening effect of the microstructure (Sun and Park, 2000; Tobin and Pak, 1993).

Open lines for research

We next discuss some open ideas for research derived from the work performed:

1. Experimental observations by (Fang et al., 2007) reveal that the crack propagates along the cleavage plane [101] in $BaTiO_3$, following a zig-zag path that matches the domain pattern. This can be included in our model by considering an anisotropic critical energy release rate G_c, resulting in a lower surface energy or fracture toughness along the cleavage planes.

2. Another important issue is the quantification and relative magnitude of the mobility parameters, which can have an important effect on the resulting response.

4 Modeling of different crack face boundary conditions

The specific coupling between the phase-field models of ferroelectric ceramics and brittle fracture depends on the particular electrical and mechanical boundary conditions adopted for the crack. We are particularly interested in different crack-face boundary conditions because they have a strong effect on the fracture behavior of piezoelectrics and ferroelectrics, and ultimately on the reliability of the devices. We have presented two coupled phase-field models in Section 3 considering some of these conditions. In this section, we propose a general framework encompassing all the usual crack-face boundary conditions in the context of phase-field models. The phase-field model of brittle fracture is viewed as a regularization of Griffith's sharp-crack model. In this sense, the aim here is to converge to the corresponding sharp-crack solutions of the specific fracture problem. For that purpose, we consider the different crack-face boundary conditions proposed in the literature for sharp-crack models in electro-mechanical materials and formulate them in the regularized phase-field model. Again, note that here the cracks are not boundaries of the computational domain, and hence the different sharp-crack conditions have to be modeled in the bulk partial differential equations.

In the context of sharp-crack models in electro-mechanical materials, the most common crack-face boundary conditions in the literature can be classified as follows:

A. Uncoupled electrical/mechanical crack-face conditions

   Mechanical boundary conditions: these are mainly: (1) traction-free crack faces and (2) cohesive zone models (Xu and Needleman, 1994; Camacho and Ortiz, 1996) introducing a traction-separation law on the crack faces. Here, we consider only traction-free crack boundary conditions. The encoding of the cohesive crack-face conditions in the context of the phase-field models is beyond the scope of this section and is the object of a future work.

   Electrical boundary conditions: these are mainly (1) permeable, (2) impermeable and (2) semi-permeable crack models, each assuming different electrical properties of the crack gap (Li et al., 2008). The permeable crack boundary conditions were first proposed for electro-mechanical materials (Parton, 1976). These conditions assume that the crack does not exist electrically, i.e. crack faces are closed and electrical fields are not perturbed by the presence of the crack. As the opposite assumption, impermeable

boundary conditions were proposed to define an open and electrically defective crack by assuming zero permittivity for the crack gap (Deeg, 1980). However, both the permeable and impermeable crack boundary conditions are not physically justifiable in many cases, since the effect of the medium filling the crack gap is neglected. As an improvement, semi-permeable boundary conditions were introduced to treat the crack gap as a linear dielectric material with a finite permittivity (Hao and Shen, 1994). As a result, the electric charge can penetrate the crack gap. A physical inconsistency of the semi-permeable conditions is that the stored electric charge in the crack gap induces a closing traction on the crack faces which is not considered in these conditions.

B. Coupled electro-mechanical crack-face conditions

The Energetically Consistent (EC) crack model was first proposed to overcome the inconsistency of the semi-permeable boundary conditions by considering not only the electric charge inside the crack gap, but also the corresponding induced closing traction on the crack faces (Landis, 2004a). In fact, the crack acts as a capacitor inside the material. EC conditions are believed to be the most physically realistic conditions on the crack faces in electro-mechanical materials.

C. Polarization boundary conditions.

In contrast to piezoelectrics, the modeling of cracks in ferroelectric materials requires the imposition of some condition for the polarization distribution on the crack faces (Wang and Kamlah, 2010). There are two usual choices, namely (1) free-polarization and (2) zero-polarization crack conditions. The former is a homogeneous Neumann boundary condition for the polarization, leaving it unaffected by the presence of the crack, and hence dictated by the bulk material model. The latter is a homogeneous Dirichlet boundary condition for the polarization, thereby modeling an open crack filled with free space.

Table 2 summarizes different crack-face boundary conditions as described above along with related mathematical descriptions.

In the following, we first focus on the phase-field formulation of these conditions for fracture in piezoelectrics based on the linear theory of piezoelectricity where microstructure

Table 2: Crack-face boundary conditions in electro-mechanical materials.

Crack-face boundary conditions			Mathematical description
Uncoupled	Mechanical	Traction-free	$\boldsymbol{\sigma}^+ \cdot \boldsymbol{n}^+ = \boldsymbol{\sigma}^- \cdot \boldsymbol{n}^- = \boldsymbol{0}$
		Cohesive zone	$\boldsymbol{\sigma}^+ \cdot \boldsymbol{n}^+ = \boldsymbol{\sigma}^- \cdot \boldsymbol{n}^- = \boldsymbol{t}$
	Electrical	Permeable	$\phi^+ = \phi^-$ $\boldsymbol{D}^+ \cdot \boldsymbol{n}^+ = \boldsymbol{D}^- \cdot \boldsymbol{n}^-$
		Impermeable	$\boldsymbol{D}^+ \cdot \boldsymbol{n}^+ = \boldsymbol{D}^- \cdot \boldsymbol{n}^- = 0$
Coupled	Electro-mechanical	Energetically Consistent (EC)	$\boldsymbol{D}^+ \cdot \boldsymbol{n}^+ = \boldsymbol{D}^- \cdot \boldsymbol{n}^- = D_c = \varepsilon_0 E_c$ $\sigma_c = \varepsilon_0 E_c^2/2$ $\mathcal{H}_c = -\varepsilon_0 E_c^2/2$
Polarization	Free-polarization		$\nabla \boldsymbol{p} \cdot \boldsymbol{n}^+ = \nabla \boldsymbol{p} \cdot \boldsymbol{n}^- = \boldsymbol{0}$
	Zero-polarization		$\boldsymbol{p}^+ = \boldsymbol{p}^- = \boldsymbol{0}$

$\boldsymbol{p}$: Polarization, $\boldsymbol{\sigma}$: Stress, $\boldsymbol{D}$: Electric displacement, ϕ: Electric potential
$\boldsymbol{t}$: Mechanical traction governed by a traction-separation law
$\boldsymbol{n}$: Unit normal to top (+) and bottom (-) crack faces
E_c and D_c : Electric field and electric displacement induced in the crack gap
$\mathcal{H}_c$: Electrical enthalpy density of the crack gap

effects are not taken into account. Due to their simplicity, these models are useful to study the basic concepts of the linear theory in the context of fracture mechanics and to evaluate the effects of individual and coupled electro-mechanical fields (McMeeking, 1999, 2004; Landis, 2004a; Li et al., 2008).

According to the linear theory of piezoelectricity, the electro-mechanical enthalpy density $\mathcal{H}$ of a piezoelectric material is stated as (Tieresten, 1969)

$$\mathcal{H}(\boldsymbol{\varepsilon}, \boldsymbol{E}) = \frac{1}{2}(\boldsymbol{\varepsilon} - \boldsymbol{\varepsilon}^r) : \mathbb{C} : (\boldsymbol{\varepsilon} - \boldsymbol{\varepsilon}^r) - (\boldsymbol{\varepsilon} - \boldsymbol{\varepsilon}^r) : \boldsymbol{e}^T \cdot \boldsymbol{E} - \boldsymbol{p}^r \cdot \boldsymbol{E} - \frac{1}{2}\boldsymbol{E} \cdot \boldsymbol{K}\boldsymbol{E}, \tag{12}$$

where $\boldsymbol{e}$ is the tensor of piezoelectric coupling constants, $\boldsymbol{\varepsilon}^r$ is the remanent strain, $\boldsymbol{p}^r$ is the remanent polarization, and $\boldsymbol{K}$ is the dielectric tensor. The electric field $\boldsymbol{E}$ is defined as $\boldsymbol{E} = -\nabla\phi$, ϕ being the electric potential. In order to encode different crack-face boundary conditions, different terms of the electro-mechanical enthalpy density in Eq. (12) are multiplied by the jump set function $(v^2 + \eta_\kappa)$. For traction-free and impermeable conditions, the jump set should be multiplied by the energy terms associated with strain $\boldsymbol{\varepsilon}$ and electric field $\boldsymbol{E}$, respectively. In contrast, the permeable conditions imply that the energy terms associated with electric field $\boldsymbol{E}$ remain unmodified by the jump set. EC conditions assume that

the crack behaves electrically similar to a capacitor, storing electrical charge between the capacitor plates. Here, we develop the general formulation of this enthalpy in the context of the phase-field model. The proposed enthalpy is stated as

$$H_c = -\frac{\varepsilon_0}{2}\int_\Omega \left(1-v^2\right)|\boldsymbol{F}^{-T}\nabla\phi|^2 J \,\mathrm{d}\Omega, \tag{13}$$

where $\boldsymbol{F}$ is the deformation gradient tensor defined as $\boldsymbol{F} = \boldsymbol{I} + \nabla\boldsymbol{u}$, $\boldsymbol{I}$ is the identity matrix and J is the Jacobian of the deformation defined as $J = \det\boldsymbol{F}$. The jump set function $\left(1-v^2\right)$ restricts the added enthalpy to the fracture zone. The electric field in the deformed configuration of the fracture zone is $\boldsymbol{E}_c = -\boldsymbol{F}^{-T}\nabla\phi$ and the enthalpy density is integrated over the area of the deformed body using the Jacobian of the deformation J. Then the electro-mechanical enthalpy density of the EC crack model is obtained by adding the proposed electro-mechanical enthalpy of the diffuse crack in Eq. (13) to the enthalpy of the impermeable crack model. Table 3 summarizes the electro-mechanical enthalpy density, stresses and electric displacements for different crack-face boundary conditions in piezoelectric materials.

The linear approach for piezoelectric materials assumes a fixed polarization and strain state under any applied electro-mechanical load. In contrast, this state can be altered in ferroelectrics in a nonlinear fashion and the additional polarization boundary conditions should also be considered. To encode the zero- and free-polarization conditions, the energy terms in Eq. (3) associated with polarization $\boldsymbol{p}$ and the gradient of polarization $\nabla\boldsymbol{p}$ should be multiplied by the jump set function $(v^2+\eta_\kappa)$, respectively. Table 4 summarizes the electro-mechanical enthalpy density, stresses and electric displacements for different crack-face boundary conditions in ferroelectric materials. See Appendix B for a detailed discussion on different crack-face boundary conditions, corresponding governing equations and a general solution algorithm for the fracture models of piezoelectric and ferroelectric materials.

Verification. We present a set of numerical simulations aimed at verifying different aspects of the proposed models. In all cases stationary cracks are considered for simplicity. We study the convergence of the energy-release rate as computed with the phase-field models summarized in Table 3 for piezoelectrics. Figure 14 presents the energy-release rates in a four-point bending setup using two mesh sizes. In the case of a permeable crack, contrary

Table 3: Electro-mechanical enthalpy density, stresses and electric displacements for piezoelectric materials with different electro-mechanical crack conditions.

	Electro-mechanical enthalpy density	Stresses and Electric displacements
Per	$\mathcal{H} = (v^2+\eta_\kappa)(\frac{1}{2}\boldsymbol{\varepsilon}:\mathbb{C}:\boldsymbol{\varepsilon}-\boldsymbol{\varepsilon}:\boldsymbol{e}^T\cdot\boldsymbol{E}) - \frac{1}{2}\boldsymbol{E}\cdot\boldsymbol{K}\boldsymbol{E}$	$\boldsymbol{\sigma} = (v^2+\eta_\kappa)(\mathbb{C}:\boldsymbol{\varepsilon}-\boldsymbol{e}^T\cdot\boldsymbol{E})$ $\boldsymbol{D} = (v^2+\eta_\kappa)\boldsymbol{e}:\boldsymbol{\varepsilon}+\boldsymbol{K}\boldsymbol{E}$
Imp	$\mathcal{H} = (v^2+\eta_\kappa)(\frac{1}{2}\boldsymbol{\varepsilon}:\mathbb{C}:\boldsymbol{\varepsilon}-\boldsymbol{\varepsilon}:\boldsymbol{e}^T\cdot\boldsymbol{E}) - (v^2+\eta_\kappa)(\frac{1}{2}\boldsymbol{E}\cdot\boldsymbol{K}\boldsymbol{E})$	$\boldsymbol{\sigma} = (v^2+\eta_\kappa)(\mathbb{C}:\boldsymbol{\varepsilon}-\boldsymbol{e}^T\cdot\boldsymbol{E})$ $\boldsymbol{D} = (v^2+\eta_\kappa)(\boldsymbol{e}:\boldsymbol{\varepsilon}+\boldsymbol{K}\boldsymbol{E})$
EC	$\mathcal{H} = (v^2+\eta_\kappa)(\frac{1}{2}\boldsymbol{\varepsilon}:\mathbb{C}:\boldsymbol{\varepsilon}-\boldsymbol{\varepsilon}:\boldsymbol{e}^T\cdot\boldsymbol{E}) - (v^2+\eta_\kappa)(\frac{1}{2}\boldsymbol{E}\cdot\boldsymbol{K}\boldsymbol{E}) - \frac{\varepsilon_0}{2}\left(1-v^2\right)\left\|\boldsymbol{F}^{-T}\boldsymbol{E}\right\|^2 J$	$\boldsymbol{\sigma} = (v^2+\eta_\kappa)(\mathbb{C}:\boldsymbol{\varepsilon}-\boldsymbol{e}^T\cdot\boldsymbol{E}) + \frac{J}{2}\left(1-v^2\right)\boldsymbol{\sigma}_c$ $\boldsymbol{D} = (v^2+\eta_\kappa)(\boldsymbol{e}:\boldsymbol{\varepsilon}+\boldsymbol{K}\boldsymbol{E}) + J\left(1-v^2\right)\boldsymbol{F}^{-1}\boldsymbol{D}_c$

Per: Permeable (traction-free), Imp: Impermeable (traction-free)
EC: Energetically Consistent

$$\begin{aligned}\boldsymbol{D}_c &= \varepsilon_0\boldsymbol{E}_c = \varepsilon_0\boldsymbol{F}^{-T}\boldsymbol{E},\\ \boldsymbol{\sigma}_c &= \boldsymbol{F}^{-1}\left(\boldsymbol{D}_c\otimes\boldsymbol{E}_c\right)+\left(\boldsymbol{D}_c\otimes\boldsymbol{E}_c\right)\boldsymbol{F}^{-T}-\frac{\varepsilon_0}{2}|\boldsymbol{E}_c|^2\left(\boldsymbol{F}^{-1}+\boldsymbol{F}^{-T}\right)\end{aligned}$$

to one's intuition, the energy release rate computed for the coarse mesh decreases as the magnitude of the applied electric field increases. This situation is readily corrected by refining the mesh and thereby reducing the regularization parameter κ. Indeed, for the resolved (fine) mesh it is interesting to observe that the value of energy release rate is insensitive to the magnitude of the applied electric field, in agreement with the results of the sharp-crack model obtained by (Li et al., 2008). In contrast, the impermeable conditions indicate a significant decrease of the energy release rate in the presence of applied electric fields. This behavior is interpreted as a strong retarding effect on the crack propagation.

Table 4: Electro-mechanical enthalpy density, stresses and electric displacements for ferroelectric materials with different electro-mechanical crack conditions.

	Electro-mechanical enthalpy density	Stresses and Electric displacements
	Free-polarization	
Per	$\mathcal{H} = (v^2+\eta_\kappa)(U+W)+\chi - \frac{\varepsilon_0}{2}\lvert\boldsymbol{E}\rvert^2 - \boldsymbol{E}\cdot\boldsymbol{p}$	$\boldsymbol{\sigma} = (v^2+\eta_\kappa)\frac{\partial W}{\partial \boldsymbol{\varepsilon}}$ $\boldsymbol{D} = \varepsilon_0\boldsymbol{E}+\boldsymbol{p}$
Imp	$\mathcal{H} = (v^2+\eta_\kappa)(U+W)+\chi - (v^2+\eta_\kappa)(\frac{\varepsilon_0}{2}\lvert\boldsymbol{E}\rvert^2 + \boldsymbol{E}\cdot\boldsymbol{p})$	$\boldsymbol{\sigma} = (v^2+\eta_\kappa)\frac{\partial W}{\partial \boldsymbol{\varepsilon}}$ $\boldsymbol{D} = (v^2+\eta_\kappa)(\varepsilon_0\boldsymbol{E}+\boldsymbol{p})$
EC	$\mathcal{H} = (v^2+\eta_\kappa)(U+W)+\chi - (v^2+\eta_\kappa)(\frac{\varepsilon_0}{2}\lvert\boldsymbol{E}\rvert^2 + \boldsymbol{E}\cdot\boldsymbol{p}) - \frac{\varepsilon_0}{2}\left(1-v^2\right)\lvert\boldsymbol{F}^{-T}\boldsymbol{E}\rvert^2 J$	$\boldsymbol{\sigma} = (v^2+\eta_\kappa)\frac{\partial W}{\partial \boldsymbol{\varepsilon}} + \frac{J}{2}\left(1-v^2\right)\boldsymbol{\sigma}_c$ $\boldsymbol{D} = (v^2+\eta_\kappa)(\varepsilon_0\boldsymbol{E}+\boldsymbol{p}) + J\left(1-v^2\right)\boldsymbol{F}^{-1}\boldsymbol{D}_c$
	Zero-polarization	
Per	$\mathcal{H} = U + (v^2+\eta_\kappa)(W+\chi-\boldsymbol{E}\cdot\boldsymbol{p}) - \frac{\varepsilon_0}{2}\lvert\boldsymbol{E}\rvert^2 - (1-v^2)\frac{\varepsilon_r-\varepsilon_0}{2}\lvert\boldsymbol{E}\rvert^2$	$\boldsymbol{\sigma} = (v^2+\eta_\kappa)\frac{\partial W}{\partial \boldsymbol{\varepsilon}}$ $\boldsymbol{D} = \varepsilon_0\boldsymbol{E} + (v^2+\eta_\kappa)\boldsymbol{p} + (1-v^2)(\varepsilon_r-\varepsilon_0)\boldsymbol{E}$
Imp	$\mathcal{H} = U + (v^2+\eta_\kappa)(W+\chi) - (v^2+\eta_\kappa)(\frac{\varepsilon_0}{2}\lvert\boldsymbol{E}\rvert^2 + \boldsymbol{E}\cdot\boldsymbol{p})$	$\boldsymbol{\sigma} = (v^2+\eta_\kappa)\frac{\partial W}{\partial \boldsymbol{\varepsilon}}$ $\boldsymbol{D} = (v^2+\eta_\kappa)(\varepsilon_0\boldsymbol{E}+\boldsymbol{p})$
EC	$\mathcal{H} = U + (v^2+\eta_\kappa)(W+\chi) - (v^2+\eta_\kappa)(\frac{\varepsilon_0}{2}\lvert\boldsymbol{E}\rvert^2 + \boldsymbol{E}\cdot\boldsymbol{p}) - \frac{\varepsilon_0}{2}\left(1-v^2\right)\lvert\boldsymbol{F}^{-T}\boldsymbol{E}\rvert^2 J$	$\boldsymbol{\sigma} = (v^2+\eta_\kappa)\frac{\partial W}{\partial \boldsymbol{\varepsilon}} + \frac{J}{2}\left(1-v^2\right)\boldsymbol{\sigma}_c$ $\boldsymbol{D} = (v^2+\eta_\kappa)(\varepsilon_0\boldsymbol{E}+\boldsymbol{p}) + J\left(1-v^2\right)\boldsymbol{F}^{-1}\boldsymbol{D}_c$

Per: Permeable (traction-free), Imp: Impermeable (traction-free), EC: Energetically Consistent

The behavior of the EC model is very close to that of the impermeable model for the coarse mesh, while showing a less significant retarding effect for the fine mesh. The converged results of the phase-field models corresponding to the different crack-face conditions for the fine mesh, presented in Fig. 14, agree qualitatively with the results of the sharp-crack model obtained by (Li et al., 2008).

We also present numerical evidence that indeed the phase-field solutions, both for piezoelectrics and ferroelectrics, satisfy the corresponding crack-face conditions in a diffuse sense, i.e. in the limit of vanishingly small regularization parameter κ, and converge to the solutions of the corresponding sharp-crack model as the mesh size h and κ tend to zero in a concerted manner. Figure 15 presents the results for the case of the traction-free, impermeable crack model along a cross section of the four-point bending sample normal to the crack and behind the crack tip. The v field is also plotted along the same section in Fig. 15(a) to indicate the cross-section of the diffuse cracks. For comparison purposes, the same problem is solved with the corresponding sharp-crack model by geometrically introducing a pre-crack of the same length in the computational model. It is obvious in Fig. 15 that by decreasing

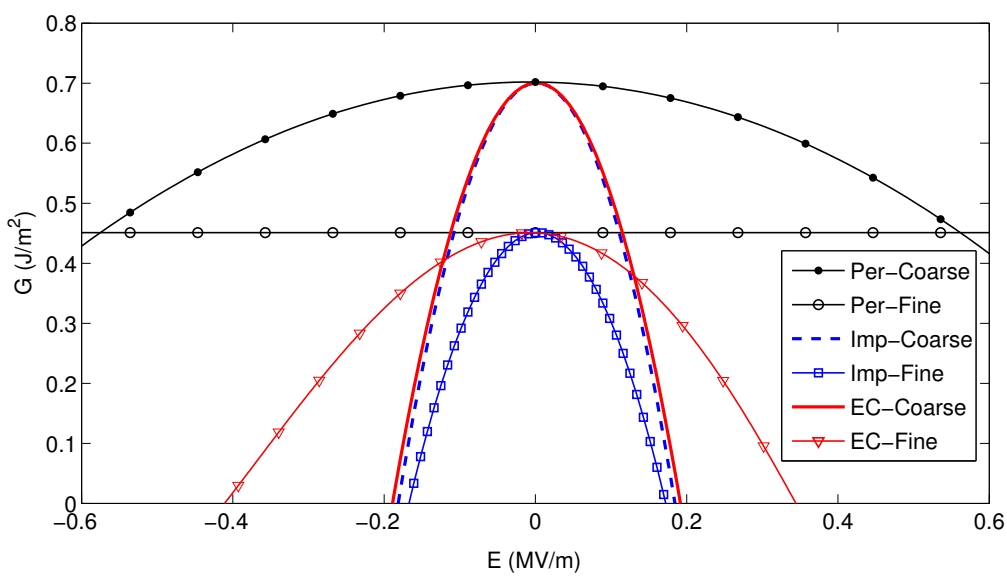

Figure 14: Energy release rates for different crack face conditions: Permeable (Per), Impermeable (Imp) and air-filled Energetically Consistent (EC) as a function of applied electric field. A mechanical loading $P = 2000$ N is applied and the change of crack length is considered as $\Delta a = 0.05$. The results are presented for a coarse mesh ($\kappa = 4 \times 10^{-2}$ mm, $h = 10^{-2}$ mm) and a fine mesh ($\kappa = 4 \times 10^{-4}$ mm, $h = 10^{-4}$ mm), respectively.

the value of the regularization parameter with the mesh size, the transition of the field v between the intact ($v = 1$) and fractured ($v = 0$) zones becomes sharper and the stresses and electric displacements recover the solutions of the sharp-crack model near the edges of the smeared crack.

In the case of the phase-field models of fracture in ferroelectrics summarized in Table 4, we have conducted analogous verification tests. We have obtained similar conclusions from the comparison of the profiles of stresses and electric displacements across of the diffuse crack with those computed for the sharp-crack, for the case of the permeable and impermeable crack models and both for free-polarization and zero-polarization conditions. As expected, since the crack-face boundary conditions are encoded for ferroelectrics by analogy to piezoelectrics, we are able to show that the phase-field solutions (1) satisfy the corresponding crack-face conditions in a diffuse manner and (2) converge to the corresponding sharp-crack solutions. Some of these results are presented in our recent work (Abdollahi and Arias, 2011a) in Appendix A.

Numerical simulations of propagating cracks. We examine the effects of the different crack-face conditions on the crack propagation. Figure 16 presents the crack growth as a function of the time in the piezoelectric four-point bending specimen. External electric fields $E = \pm 1$ MV/m are applied from time $t = 190$ s. It is apparent that the impermeable crack is completely arrested by the application of both the positive and negative electrical load while the permeable crack remains unaffected by it. The crack growth rate for the EC conditions lies between that of the permeable and impermeable conditions. While the permeable and impermeable crack models show no sensitivity to the sign of the applied electric field, the air-filled EC crack is less retarded under the negative applied electric field than under the positive one. These observations, and in particular the asymmetric response of the EC crack model with respect of the sign of the applied electric field, are also apparent from the converged results of energy release rate in Fig. 14.

Similar simulations have also been carried out for ferroelectric materials and the effect of domain switching in the vicinity of the crack on the crack propagation is evaluated. The results are presented in Fig. 17 for the different crack-face conditions and under various applied electric fields. It is obvious that the crack growth increases with the application of the negative normalized electric field $E = -5 \times 10^{-3}$ for all the crack conditions. This

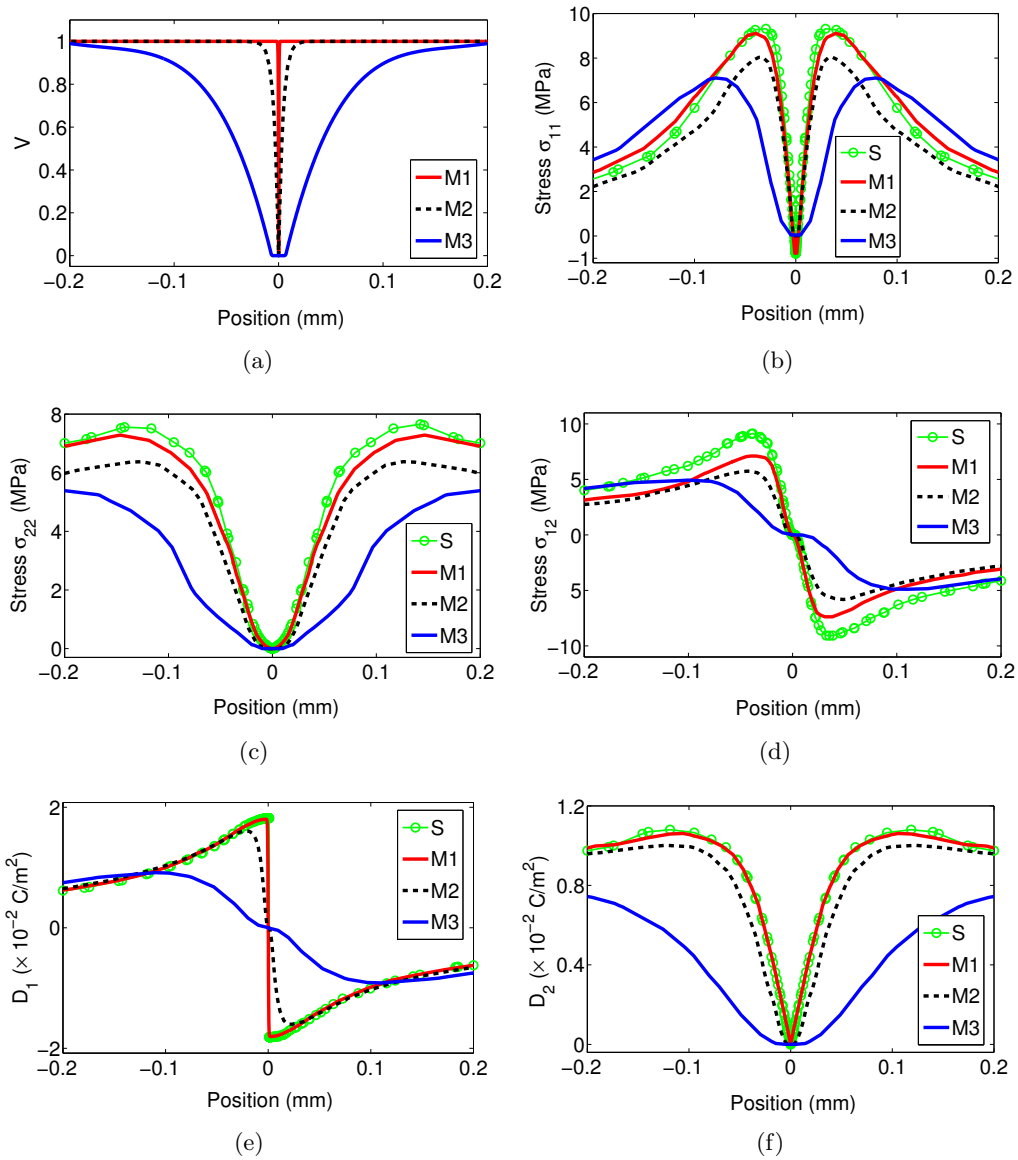

Figure 15: (a) Field v along a cross section of the four-point bending sample normal to the crack and behind the crack tip, (b)-(f) Stresses and electric displacements along the same section. The results are obtained for a traction-free, electrically impermeable pre-crack. Different values of the regularization parameter κ and mesh sizes h are chosen near the smeared crack for each simulation: M1 ($\kappa = 4 \times 10^{-2}$, $h = 10^{-2}$) , M2 ($\kappa = 0.4$, $h = 0.1$) and M3 ($\kappa = 4$, $h = 1$). A simulation is also done for the sharp-crack model (marked with S) with mesh size $h = 10^{-2}$ near the crack faces. Both κ and h are normalized by the value of 10^{-2} mm.

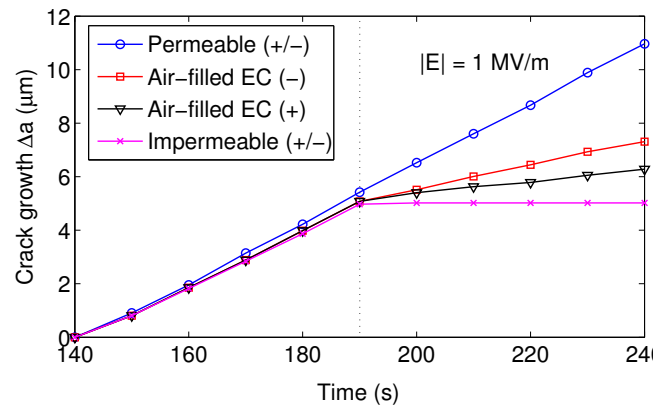

Figure 16: Crack growth (Δa) as a function of the time in the piezoelectric material considering the permeable, impermeable and air-filled EC crack face conditions. External electric fields $E = \pm 1$ MV/m are applied from time $t = 190$ s. The + and - signs indicate a positive and negative applied electric field.

weakening effect is more pronounced for the EC crack model. The normalized electric field $E = -10^{-2}$ (above the coercive field in magnitude) decreases the crack growth significantly and it shows a similar toughening effect to that of the positive applied electric fields. Similarly to piezoelectric materials, the strongest retarding effect on the crack propagation is observed for the impermeable conditions. According to Fig. 17, the impermeable crack is almost arrested under the normalized electric field $E = 10^{-2}$.

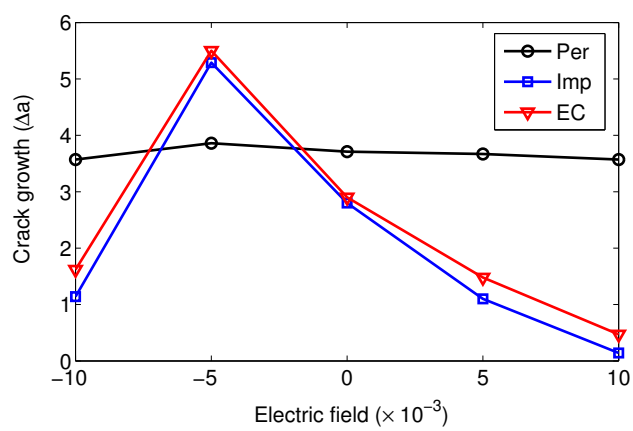

Figure 17: Crack growth (Δa) as a function of the magnitude and sign of the electric field in the ferroelectric material. The results are obtained for the different crack face conditions: Permeable (Per), Impermeable (Imp) and air-filled Energetically Consistent (EC).

Contributions

We summarize here the most significant contributions of this work, which has been submitted for publication as a research paper in (Abdollahi and Arias, 2012c):

1. We present a family of phase-field models of fracture in piezoelectric and ferroelectric materials. Different electro-mechanical crack conditions (defined as crack-face boundary conditions in sharp-crack models) are encoded into the phase-field framework. A set of simulations is performed to verify the proposed phase-field models against the corresponding sharp-crack models. The results provide numerical evidence that for small enough values of the regularization parameter, the proposed models recover the solutions of the sharp-crack models near the edges of the diffuse cracks.

2. We have also conducted simulations to examine the effects of the different crack-face conditions, electro-mechanical loadings and crack-gap filling media on the crack propagation and the microstructure evolution of the material. Simulation results show that a negative electric field (below the coercive field) enhances the crack propagation perpendicular to the initial polarization in ferroelectrics, while a positive electric field retards it, which is in agreement with experiments (Ricoeur and Kuna, 2003; Wang and Singh, 1997; Shindo et al., 2002; Jiang et al., 2009).

Open lines for research

We next discuss some open ideas for research derived from the work performed:

1. We have provided numerical evidence that the phase-field solutions converge to those of the corresponding sharp-crack models for small enough values of the fracture regularization parameter and the mesh size. However, a rigorous mathematical analysis would be desirable to prove this convergence.

2. Three dimensional simulations and an extension to polycrystalline materials along the lines of (Abdollahi and Arias, 2012b) are necessary.

5 Phase-field simulation of anisotropic crack propagation in ferroelectric single crystals

Formation and evolution of ferroelectric domains near the crack tip is responsible for changes in the fracture behavior of ferroelectric materials such as fracture toughness anisotropy. The Vickers indentation technique is commonly used in determining this anisotropy (Sun and Park, 2000; Pisarenko et al., 1985; Tobin and Pak, 1993; Wang and Singh, 1997; Lynch, 1998; Schneider and Heyer, 1999). These experimental observations show that the cracking along the poling direction of the material has a shorter length and consequently higher fracture toughness, and that normal to the poling direction has a longer length and lower fracture toughness. Ferroelastic domain switching is known as the main cause of the anisotropy. The main objective of this section is to introduce a model which can simulate the anisotropic crack growth under Vickers indentation loading with the goal of linking the microstructural details with the macroscopic observable response. For this purpose, the model proposed in Section 3 is modified following (Amor et al., 2009) by introducing a crack non-interpenetration condition in the variational approach to fracture accounting for the asymmetric behavior in tension and compression in the framework of linearized elasticity. This condition is essential for the simulation of the Vickers indentation test since the indentation loading induces high compressive stresses near the indenter contact faces. Without the crack non-interpenetration condition, the variational approach would lead to crack propagation and interpenetration in the compression zones, along the indenter faces. Furthermore, radial crack propagation in tension zones is only obtained when this condition is considered in the model. For the ferroelectric response, we follow the Devonshire-Ginzburg-Landau phase-field model presented in (Zhang and Bhattacharya, 2005a) just as in the coupled phase-field model presented in Section 3.

We briefly describe here the coupled phase-field formulation with emphasis on the modification introduced to account for the asymmetric behavior in tension and compression. We form a total electro-mechanical enthalpy of a possibly fractured ferroelectric material occupying a region Ω as

$$H[\boldsymbol{u},\boldsymbol{p},\phi,v] = \int_\Omega [W_e(\boldsymbol{\varepsilon}(\boldsymbol{u}),v) + W_f(\boldsymbol{\varepsilon}(\boldsymbol{u}),\boldsymbol{p},\phi,v)]\ \mathrm{d}\Omega \\ +G_c \int_\Omega \left[\frac{(1-v)^2}{4\kappa} + \kappa|\nabla v|^2\right]\ \mathrm{d}\Omega, \tag{14}$$

where body loads, volume charges, tractions and surface charges have been ignored for simplicity. In this functional, the bulk energy (first integral) competes with the surface energy (second integral). All the constants and parameters are defined in Section 3. In the bulk energy, W_e is the part of the bulk energy density associated with the strain $\boldsymbol{\varepsilon}$ and W_f is the electro-mechanical energy density associated with the ferroelectric response. To account for the quite different fracture behavior in tension and compression, the energy density W_e is written in (Amor et al., 2009) as

$$W_e(\boldsymbol{\varepsilon}, v) = \kappa_0 \frac{\mathrm{tr}^-(\boldsymbol{\varepsilon})^2}{2} + (v^2 + \eta_\kappa)\Big(\kappa_0 \frac{\mathrm{tr}^+(\boldsymbol{\varepsilon})^2}{2} + \mu\, \boldsymbol{\varepsilon}_D \cdot \boldsymbol{\varepsilon}_D\Big), \tag{15}$$

where κ_0 and μ are the bulk and shear modulus of the material, respectively. The decomposition of the trace of the strain tensor $\boldsymbol{\varepsilon}$ in positive and negative parts are $\mathrm{tr}^+ = \max(\mathrm{tr}(\boldsymbol{\varepsilon}), 0)$ and $\mathrm{tr}^- = \max(-\mathrm{tr}(\boldsymbol{\varepsilon}), 0)$ and $\boldsymbol{\varepsilon}_D$ are the deviatoric components of the strain tensor. This decomposition is introduced to distinguish the contributions to the strain energy due to compression, expansion, and shear. In contrast to (Abdollahi and Arias, 2011a) and Section 3, here only the expansion and shear terms are multiplied by the jump set function $(v^2+\eta_\kappa)$ to prevent crack nucleation, propagation and interpenetration in compressed regions.

The electro-mechanical energy density W_f associated with polarization $\boldsymbol{p}$, electric potential ϕ, $\boldsymbol{\varepsilon}$ and v is formulated as

$$W_f(\boldsymbol{\varepsilon}, \boldsymbol{p}, \phi, v) = (v^2 + \eta_\kappa)[U(\nabla \boldsymbol{p}) + W(\boldsymbol{p}, \boldsymbol{\varepsilon})] + \chi(\boldsymbol{p}) - \frac{\varepsilon_0}{2}|\nabla\phi|^2 + \nabla\phi \cdot \boldsymbol{p}, \tag{16}$$

where energy functions U , χ and W are defined in Appendix C. This particular formulation of the phase-field model encodes the asymmetric fracture response in tension and compression, as well as the assumed crack conditions. We assume the crack to be traction-free and electrically permeable. The governing equations and a solution algorithm are presented in detail in Appendix C.

We consider an indentation impression lying inside a ferroelectric single crystal in two dimensions. A monotonically increasing mechanical load is applied by pulling the indentation faces with uniform displacement. It is also assumed that the indenter faces are connected to the ground, therefore the electric potential is fixed to zero on the indentation faces. All

the material parameters are selected to fit the behavior of single crystals of barium titanate ($BaTiO_3$). Figure 18 presents a snapshot of the crack propagation. The value of v starts to decrease towards zero around the vertices of the indentation as the load increases. After reaching the zero value, the fracture zone grows along the four radial directions as shown in Fig. 18.

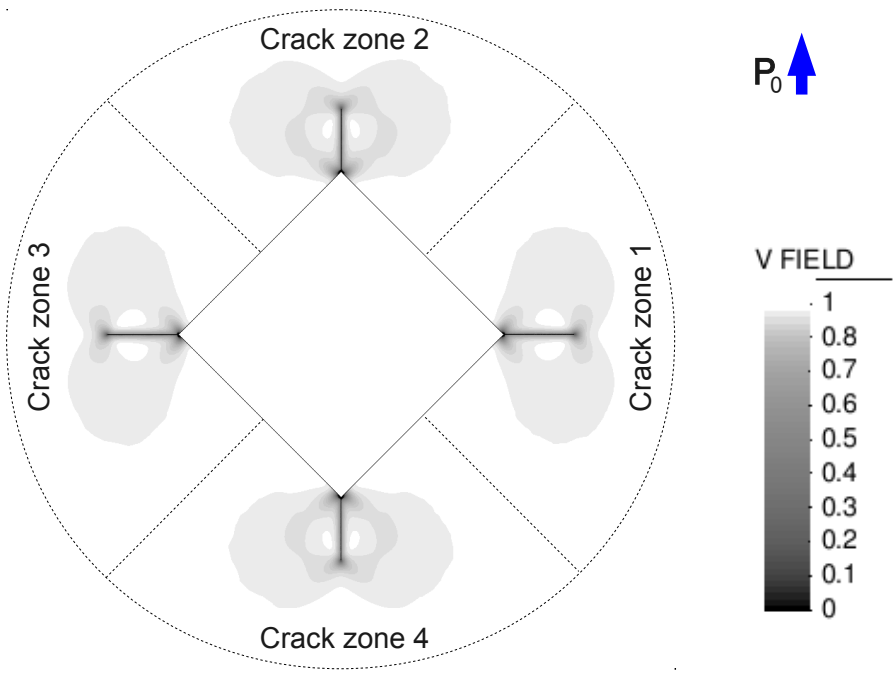

Figure 18: Snapshot of the fracture evolution. Field v represents the fracture area. Four equally large areas around the corners of the indentation are considered to obtain the surface energy evolution of the four radial cracks (crack zones $1-4$) shown in Fig. 19.

To evaluate the radial crack growth, four equally large areas around the corners of the indentation are considered in Fig. 18 and the value of surface energy (the second integral in Eq. (14) is obtained for each zone. Note that the surface energy is an indirect measure of the crack length. The surface energy graphs are shown in Fig. 19. It is obvious in this figure that surface energies of zones 1 and 3 follow nearly the same path. This also holds for zones 2 and 4. Interestingly, the surface energies of zones 1 and 3 are larger than those of zones 2 and 4, i.e. the perpendicular cracks to the polarization are longer than the parallel ones. This is a clear evidence of the anisotropic crack propagation in agreement with experimental observations. For comparison purposes, we also compute the surface

energy for an elastic single-phase material by fixing the initial polarization to zero. The energy graphs of all the four zones for the single-phase material fall on top of each other, a testament of the isotropic crack propagation. One of these graphs is presented in Fig. 19 (marked as single-phase graph).

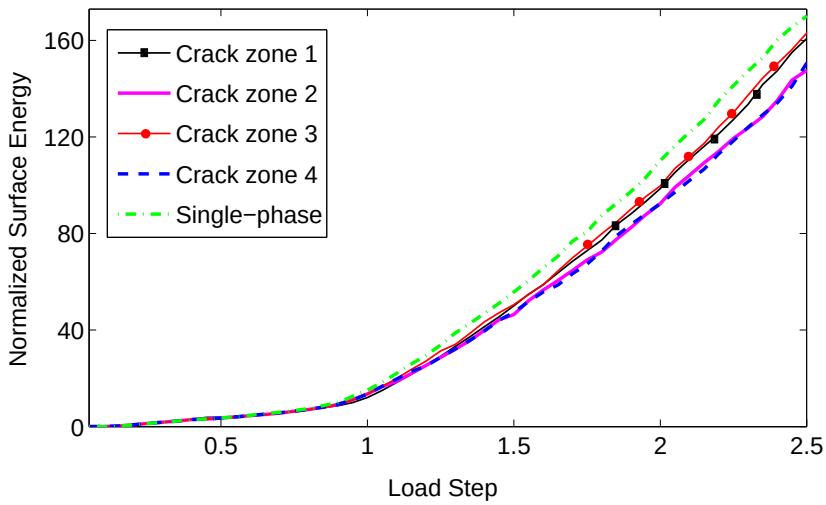

Figure 19: Evolution of the normalized surface energy of the four zones (crack zones $1-4$) marked in Fig. 18 as a function of the load step. The single-phase graph is obtained for one of these zones considering the elastic material with zero fixed polarization.

The origin of the observed fracture toughness anisotropy can be found in the domain switching during crack growth. Figure 20 presents a snapshot of the domain evolution in an area around the indentation. Ferroelastic domain switching occurs around the tip of the parallel cracks (cracks 2 and 4), where the horizontal components of the polarization vectors indicate wing-shaped domains or twins. This kind of switching is induced by the high tensile stresses near the crack tip tending to elongate the material in the horizontal direction in front of the parallel cracks. Due to the absence of ferroelastic domain switching, the perpendicular cracks grow more than parallel ones and the effective fracture toughness is lower perpendicular to the poling direction. It is also obvious in Fig. 19 that the elastic single-phase material has the lowest fracture toughness due to the absence of the microstructure effect.

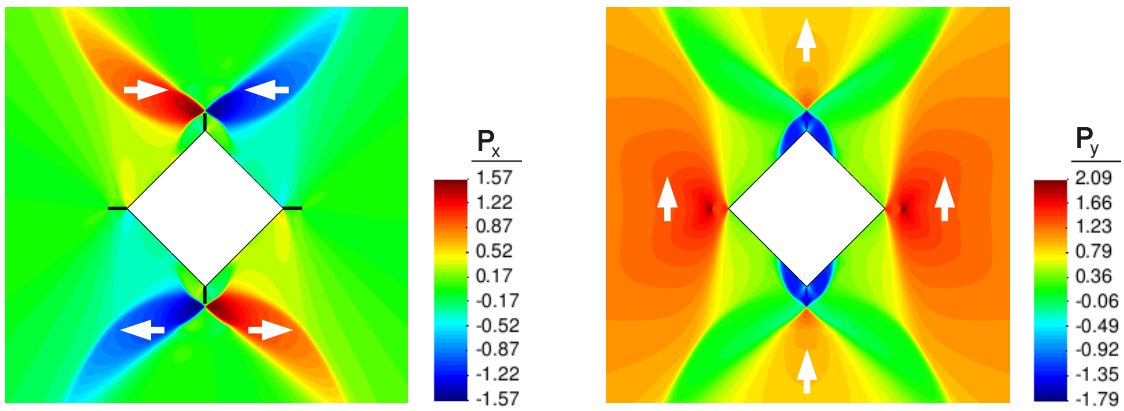

Figure 20: Snapshot of the microstructure evolution in an area near the indentation. The left and right columns show the horizontal and vertical components of the polarization, respectively. The black lines in the left column indicate the position of the cracks ($v = 0$). The domain orientations are indicated with white arrows.

Contributions

We summarize here the most significant contributions of this work, which has been published as a research paper in (Abdollahi and Arias, 2011b):

1. We perform, to the best of our knowledge, the first simulation of Vickers indentation crack growth in ferroelectric single crystals with the goal of evaluating the effect of the microstructure on the fracture process. This is done by formulating a coupled phase-field model based on a modified variational formulation of brittle crack propagation and the material model to prevent crack formation and interpenetration in the compressed regions.

2. The simulation results show that radial cracks perpendicular to the poling direction of the material propagate faster than parallel ones, which is in agreement with experimental observations (Sun and Park, 2000; Pisarenko et al., 1985; Tobin and Pak, 1993; Wang and Singh, 1997; Lynch, 1998; Schneider and Heyer, 1999). This anisotropy in the fracture toughness follows from the fully coupled interactions between the material microstructure and the crack propagation. 90^o ferroelastic switching induced by the intense crack-tip stress field is observed near the parallel cracks, which is believed as the main fracture toughening mechanism in ferroelectric materials.

Open lines for research

We next discuss some open ideas for research derived from the work performed:

1. A more precise evaluation of the microstructure effect will be obtained by extending the proposed model to three dimensions and running longer simulations producing more extended cracks.

2. Although domain switching is claimed to be the main source of fracture toughness anisotropy, the intrinsic anisotropy of the crystal, i.e. the different surface energy in different cleavage planes, is bound to have an effect as well.

6 Crack initiation patterns at electrode edges in multilayer ferroelectric actuators

Multilayer ferroelectric actuators are ideal candidates for numerous applications in smart structures and adaptive systems in view of their small sizes, low driving voltages and quick response times. Applications include microprecision cutting machines, inkjet printer heads, laser printers, optical disk drives and laser tuning (Uchino and Takahashi, 1996; Pritchard et al., 2001), to mention a few. However, the structures of multilayer actuators often employ internal electrodes, which terminate inside the ferroelectric ceramic. In the vicinity of each terminated electrode edge, a non-uniform electric field is induced by the driving voltage, producing an incompatible strain field. A complex stress field arises from this incompatibility, which may lead to crack initiation and propagation around the electrode edge. Therefore, it is necessary to understand the fracture behavior of multilayer ferroelectric actuators to assure optimum reliability of the systems and guide the design. Towards this goal, numerous experimental and theoretical investigations have been carried out during the past decades. Experimental observations confirm that the cracks initiate mainly from the electrode edge and they can propagate through the ceramic, along the ceramic-electrode interface and perpendicular to the electrode edge (Uchino and Furuta, 1992; Furuta and Uchino, 1993; Aburatani et al., 1994; Lucato et al., 2001; Koh et al., 2004; Liu et al., 2005; Zhao et al., 2010). Early theoretical models were developed for fracture mechanics analysis of multilayer electrostrictive ceramics (Winzer et al., 1989; Yang and Suo, 1994; Hao et al., 1996; Gong and Suo, 1996; Ru et al., 1998). Related studies have been also conducted based on the linear theory of piezoelectricity (Ru, 2000; Ye and He, 2001; Li and Tang, 2003; Wang, 2005; Guo et al., 2006). However, the intrinsic nature of most piezoelectric materials demands the consideration of nonlinear electromechanical effects. To address this problem, nonlinear approaches were proposed taking into account the ferroelectric and ferroelastic behaviors (Kamlah and Bohle, 2001; Lucato et al., 2001; Elhadrouz et al., 2006; Zhao et al., 2010).

The above mentioned models for the fracture of multilayer actuators are useful to analyze the electromechanical fields near the electrode edge. Based on this analysis, some design criteria can be proposed regarding the geometry of the actuators and electrodes to reduce the probability of fracture from the electrode edge. However, these models do not study the crack propagation mechanisms of the actuators and these mechanisms are still unclear

due to the complex interactions between the propagating cracks, electromechanical fields and microstructure of the material near the electrode edge. The potential of the phase-field approach, presented in Section 5, to capture the complex interactions between the crack and the material microstructure motivates us to employ it for the fracture analysis of multilayer ferroelectric actuators. In particular, the objective of this section is to study the crack initiation at the electrode edge during the poling process. Considering different bonding conditions between the ceramic and electrode layers, different crack initiation patterns are obtained, which are useful to understand the fracture processes in this type of actuators.

The theory of the phase-field model is presented in Section 5, where the formulation encodes the asymmetric fracture response in tension and compression. This condition is essential for the simulation of the crack propagation at the electrode edge since high compressive stresses are induced in this region (Furuta and Uchino, 1993; Kamlah and Bohle, 2001).

A schematic of the computational model is presented in Fig. 21. All the material parameters, boundary conditions and loading are presented in detail in Appendix D. Here we consider three extreme assumptions for the bonding of the ceramic and electrode layers at the bottom boundary. The first model assumes that the ceramic layers and internal electrodes are firmly cofired together without considering any defects between the layers, i.e. the fully cofired model. As an intermediate assumption, the ceramic-electrode interface is considered to be fully cofired while there is no ceramic-ceramic bonding ahead of the electrode edge (Zhao et al., 2010). This model is called the partially cofired model. Finally, the third assumption considers fully separated layers on both interfaces. In fact this model represents a single layer of the multilayer actuator where the internal electrode is located at the surface of the actuator (Lucato et al., 2001). This model is called the surface electrode model.

Figure 22 presents snapshots of the crack propagation in a small neighborhood of the electrode edge for the three models. In all of the simulations, as the driving voltage V_d increases, the v field starts to decrease at the electrode edge until it reaches the threshold to be considered permanently fractured. By further increasing of the electric field, the v field evolves in a different direction from the electrode edge in each model. Figure 22(a) shows that the crack mainly propagates along the ceramic-ceramic interface ahead of the electrode edge in the fully cofired model. On the contrary, Fig. 22(b) indicates that a

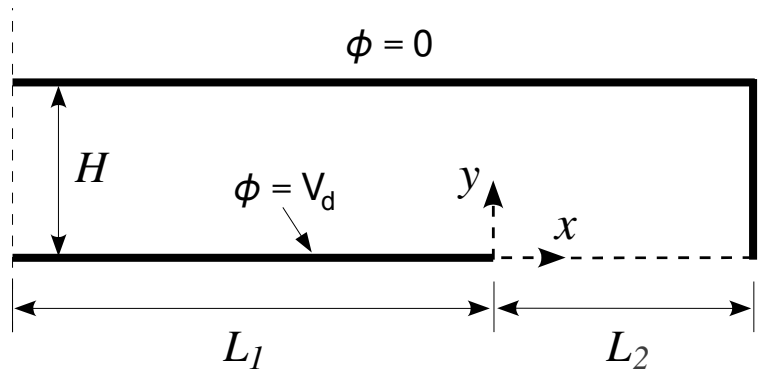

Figure 21: Schematic of the computational model for a single layer of the multilayer actuator. The electrodes are indicated with the thick lines and the origin of the coordinate system is located at the electrode edge. V_d is the driving voltage of the actuator.

preferential path for the crack propagation is along the ceramic-electrode interface in the partially cofired model. It is noteworthy that the experimental results in (Zhao et al., 2010) show a similar crack propagation path along the electrode-ceramic interface in a partially cofired actuator. As for the surface electrode model, it is interesting to observe in Fig. 22(c) that the crack propagates obliquely from the electrode into the material.

The crack initiation patterns presented in Fig. 22 also suggest a crack propagation scenario in multilayer ferroelectric actuators. The most common design of these actuators is that the ceramic layers and electrodes are fully cofired together. For this design, the simulation results show that the first crack initiation site is the ceramic-ceramic interface ahead of the electrode edge, see Fig. 22(a). If the crack propagates a certain distance along this interface, a new crack will initiate in the opposite direction along the electrode-ceramic interface, as also observed in Fig. 22(a). This fracture process can be explained as follows. Since the first crack gradually cuts the ceramic-ceramic interface into a traction-free surface, an interface gap is formed ahead of the electrode edge and the fully cofired actuator becomes a partially cofired one. Consequently, in the partially cofired actuator, the new crack initiates along the electrode-ceramic interface, as presented in Fig. 22(b). A sufficient propagation of the new crack changes the electrode-ceramic interface into a traction-free surface and the partially cofired actuator gradually converts to a surface electrode one. In this situation, the third mode of fracture will be activated, which is the oblique crack propagation in the surface electrode model, see Fig. 22(c). The above mentioned events reflect a crack

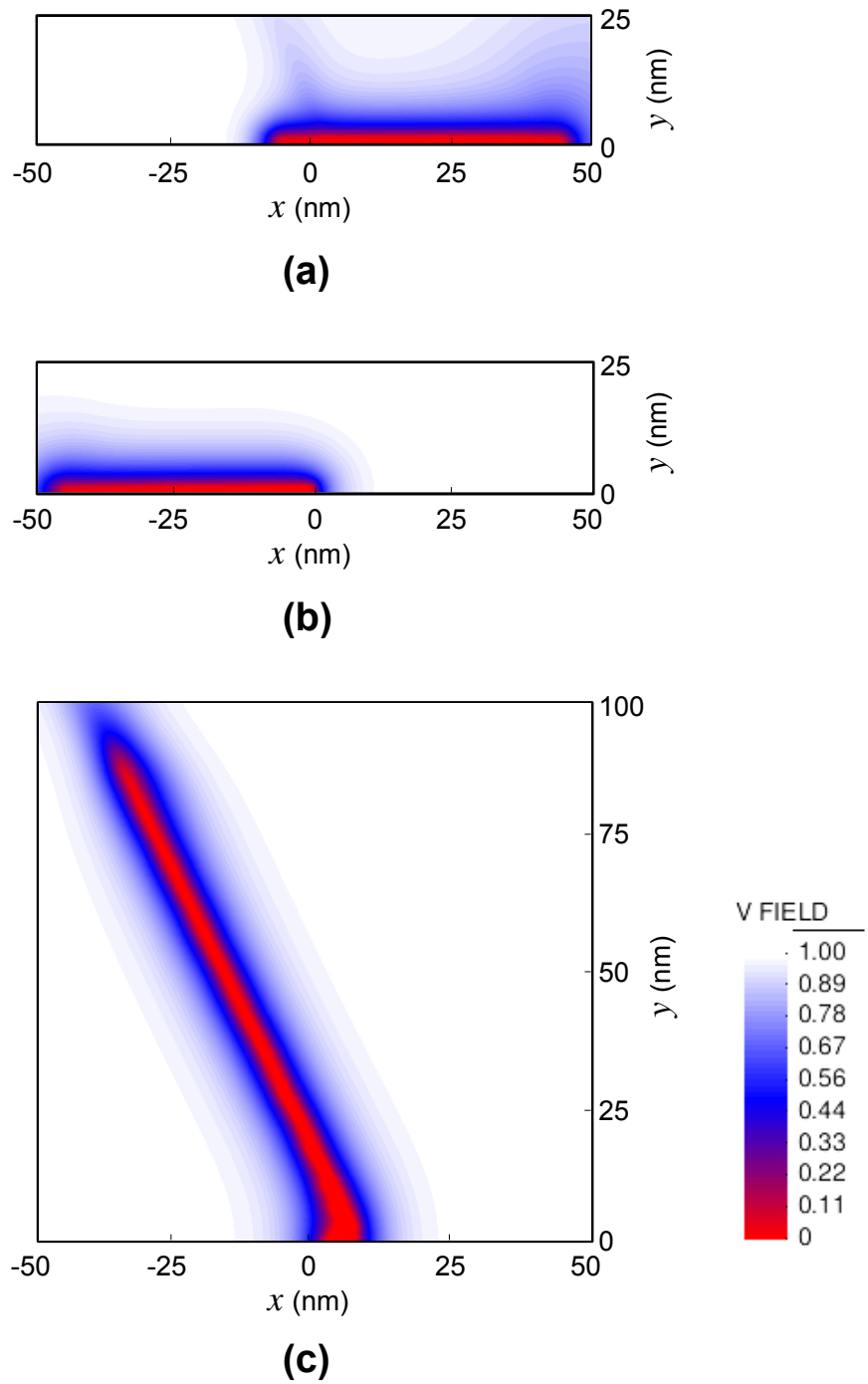

Figure 22: Crack initiation patterns in a small neighborhood of the electrode edge for the (a) fully cofired, (b) partially cofired, and (c) surface electrode models. The color contour indicates the distribution of v field representing the fracture area. Recall that the origin of the coordinate system is located at the electrode edge.

initiation process in multilayer ferroelectric actuators, which is schematically presented in Fig. 23. Interestingly, the experimental results show that the crack is initiated at the internal electrode edge, and it branches basically into three directions from the electrode edge which results in the delamination and oblique cracking of multilayer ferroelectric actuators (Uchino and Furuta, 1992; Furuta and Uchino, 1993; Aburatani et al., 1994). Our calculations suggests a mechanism explaining these observations. Note that far from these initiation sources, the direction of crack propagation can be affected by the presence of pores, domain walls or grain boundaries in polycrystals.

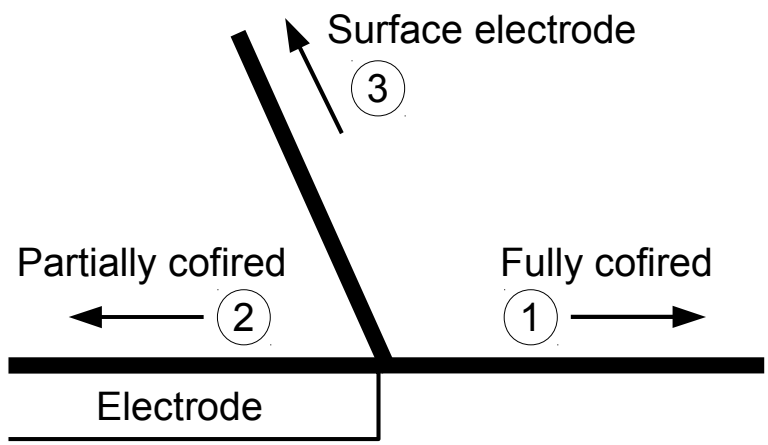

Figure 23: Schematic of the crack initiation events in multilayer ferroelectric actuators. The thick line is a schematic of the crack path and the arrows present the crack propagation directions from the electrode edge. The numbers indicate the sequence of crack initiation events from the fully cofired to the surface electrode model.

Contributions

We summarize here the most significant contributions of this work, which has been submitted for publication as a research paper in (Abdollahi and Arias, 2012a):

1. We have performed simulations of crack initiation and propagation at electrode edges in multilayer ferroelectric actuators by using a coupled phase-field model. The simulation results show different crack initiation patterns depending on the bonding conditions of the ceramic and electrode layers. These crack initiation events can reflect a fracture process in multilayer actuators. Furthermore, the obtained patterns can be

interpreted as initiation sources of experimentally observed crack branches near the electrode edge (Uchino and Furuta, 1992; Furuta and Uchino, 1993; Aburatani et al., 1994).

2. We also evaluate the effects of the ceramic layer thickness and length of the internal electrode on the crack initiation. The results show that the crack initiation becomes more difficult by decreasing the thickness of the ceramic layer and the length of the internal electrode. A similar behavior has been observed in experiments for crack initiation and propagation perpendicular to the electrode edge (Lucato et al., 2001).

Open lines for research

We next discuss some open ideas for research derived from the work performed:

1. Dielectric breakdown often occurs during the fracture of multilayer actuators via the formation of conducting tubular channels (Suo, 1993), which can release a large amount of thermal energy. This energy may affect the material properties or may induce a thermal stress near the electrode edge. Therefore, a thermo-electro-mechanical analysis is required to investigate this effect.

2. The formation and propagation of the tubular channels around the electrode edge can have an important effect on the electromechanical fields and the microstructure of the material, which needs to be investigated.

7 Phase-field model of fracture in ferroelectric polycrystals

To study the fracture process in ferroelectric polycrystals, the effect of polycrystalline microstructure should be considered by incorporating the differential fracture toughness of the bulk and the grain boundaries, and the different crystal orientations of the grains. To the best of our knowledge, no model has been proposed in the literature to study the interactions between the fracture process and the polycrystalline and domain structure in ferroelectric polycrystals. The related models (Landis, 2003; Li and Kuna, 2011) have only taken into account the grains orientations, but the effects of grain boundaries and grain size have not been considered. In (Verhoosel and Gutierrez, 2009), the grain microstructure is introduced to model inter- and transgranular crack propagation in linear piezoelectric polycrystals, thus not accounting for the effect of ferroelectric domain microstructures. The main objective of this section is to study the fracture processes in ferroelectric polycrystals in its full complexity, and in particular to evaluate the effects produced by the grain and ferroelectric domain microstructures on the fracture response of the material. For this purpose, we extend to polycrystals the phase-field model of fracture in ferroelectric single crystals presented in Section 3. The results obtained with this model prove its potential to capture complex interactions between the crack and the material microstructure.

The proposed model for fracture of ferroelectric polycrystals is based on two existing phase-field approaches for: (1) grain growth (Fan and Chen, 1997) and (2) fracture in ferroelectric single crystals (Abdollahi and Arias, 2011a). The first model provides realistic polycrystalline microstructures with different grain sizes, while the second models the complex interactions between the fracture processes and the ferroelectric domain formation and evolution. Following (Zhang and Bhattacharya, 2005b), the latter is extended to ferroelectric polycrystals. The resulting model couples three phase-fields describing (1) the polycrystalline , (2) the location of the cracks, and (3) the ferroelectric domain microstructure.

According to the phase-field model of grain growth (Fan and Chen, 1997), the total free energy of a heterogeneous system is stated as

$$F = \int_{\Omega} [f_0(\eta_1, \eta_2, ..., \eta_m) + \sum_{i=1}^{m} \frac{\kappa_i}{2} (\nabla \eta_i)^2] \, \mathrm{d}\Omega, \tag{17}$$

where f_0 is the local free energy density presented in detail in Appendix E. κ_i are the

gradient energy coefficients and field variables η_i indicate the grains where the minima of f_0 are located at $(\eta_1, \eta_2, ..., \eta_p)$ = (1, 0, ... , 0), (0, 1, ... , 0), ... , (0, 0, ... , 1). The grain boundaries are the regions of the domain where the gradient energy terms are non-zero. The evolution of the grains is governed by Ginzburg-Landau equations.

The total electromechanical enthalpy in Eq. (11) is extended here to study the crack propagation in ferroelectric polycrystals. For this purpose, the polycrystalline microstructure given by the model of grain growth is included in the formulation as follows. In the models of brittle polycrystalline materials, the fracture properties of the grain boundaries can be characterized by assuming a lower fracture toughness along these boundaries as compared to the grain interiors. Other works (Grah et al., 1996; Sukumar et al., 2003; Verhoosel and Gutierrez, 2009) have proven the validity of this assumption for the study of the intergranular and the transgranular modes of fracture. In the model of grain growth, the grain boundaries can be identified through a function ξ of the orientation field variables η_i defined as

$$\xi = \sum_{i=1}^{m} \eta_i^{2k}, \tag{18}$$

where k is a positive integer. The function ξ has a unit value inside the grains and smaller positive values at the grain boundaries. Through this function, we can easily assign a lower fracture toughness along the grain boundaries than in the grain interiors. The critical energy release rate in a polycrystal can be defined as

$$G_c^{poly} = G_c \, \mathscr{F}(\xi), \tag{19}$$

where G_c is the critical energy release rate of the bulk crystal, and the function $\mathscr{F}$ controls the weakening of the material at the grain boundaries. This function attains its maximum for $\xi = 1$ (inside the grains) and its minimum indicates the ratio of the critical fracture energy of the grain boundary to that of the grain interior. This ratio can be regulated in our model by an appropriate selection of the function $\mathscr{F}$ and setting the power k in Eq. (18) and the coefficients of the gradient energy (κ_i). Here, the function $\mathscr{F}$ is chosen to be proportional to ξ, i.e. $\mathscr{F}(\xi) = \xi$. The power of ξ is also assigned as $k = 1$ to avoid decreasing the fracture toughness towards zero along the grain boundaries, which is unphysical. We also assume that each grain is oriented along a different crystallographic direction. In 2D, the rotation angle θ is defined and its value is assigned randomly for

each orientation field variables η_i $(i = 1, ..., m)$. Using the orientation field and following the phase-field model of ferroelectric polycrystals (Zhang and Bhattacharya, 2005b), the electromechanical enthalpy density $\mathcal{H}$ in Eq. (9) can be extended to polycrystals. For this purpose, each of the energy terms in Eq. (9) is transformed from the local coordinate system of each individual grain to the global coordinate system of the polycrystal, θ being the angle between these two coordinate systems. It can be shown that all the energy terms except χ remain unchanged by this transformation. The modified energy density χ^{poly} is presented in Appendix E. By replacing the modified χ^{poly} and G_c^{poly} in Eq. (11), the electromechanical enthalpy density for a ferroelectric polycrystal takes the form

$$\begin{aligned}\mathcal{H}^{poly}(\boldsymbol{\varepsilon}, \boldsymbol{p}, \nabla\boldsymbol{p}, \boldsymbol{E}, v) =& (v^2 + \eta_\kappa)\,[U(\nabla\boldsymbol{p}) + W(\boldsymbol{p}, \boldsymbol{\varepsilon})] \\ &+ \chi^{poly}(\boldsymbol{p}) - \frac{\varepsilon_0}{2}|\boldsymbol{E}|^2 - \boldsymbol{E}\cdot\boldsymbol{p} + G_c^{poly}\left[\frac{(1-v)^2}{4\kappa} + \kappa|\nabla v|^2\right]. \qquad (20)\end{aligned}$$

The time evolution of the system along with a solution algorithm are presented in detail in Appendix E.

To perform numerical simulations, a rectangular domain is considered. First, the phase-field model of grain growth is used to obtain different polycrystalline microstructures. Two snapshots of the polycrystalline microstructure evolution are presented in Fig. 24(a) and 24(b). Grain boundaries are highlighted by darker regions in these figures. These two polycrystalline microstructures are selected for the fracture simulations in a fine- and a coarse-grain ferroelectric polycrystal, respectively.

For the fracture simulations, a monotonically increasing mechanical load is applied by pulling the top and bottom sides of the model with a uniform vertical mechanical displacement. All the material parameters are selected to fit the behavior of single crystals of barium titanate ($BaTiO_3$). Figures 24(a) and 24(b) present the final computed crack paths (when the sample is splitted into two parts) in the fine- and coarse-grain structures, respectively. It is obvious in Fig. 24(a) that the crack propagates mainly along the grain boundaries, demonstrating the intergranular mode of fracture in the fine-grain structure. On the other hand, transgranular crack propagation is observed in Fig. 24(b) where the crack propagates through the grains. Experimental observations in ferroelectric polycrystals also show this transition from intergranular fracture for small grains to transgranular fracture in the case of large grains (Kim et al., 1990; Meschke et al., 1997).

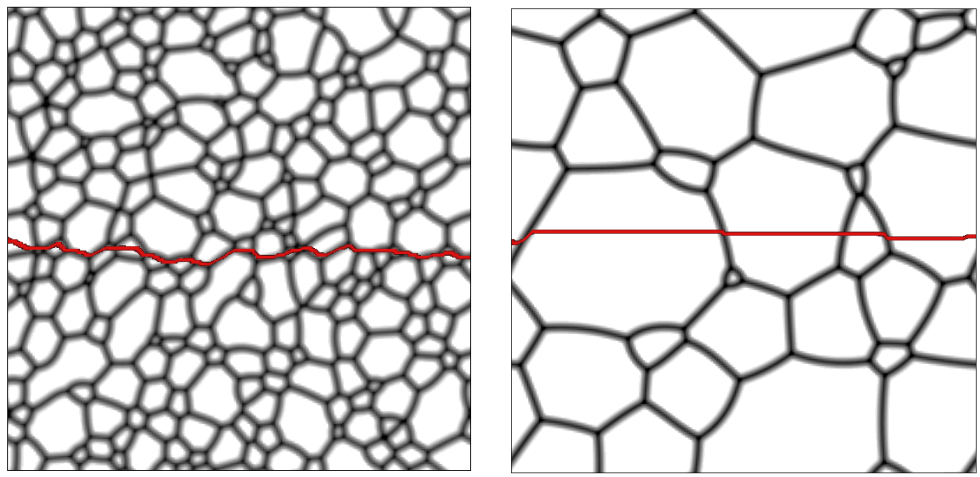

(a) (b)

Figure 24: Crack path in (a) fine-grain and (b) coarse-grain ferroelectric polycrystals. The points where $v = 0$ are depicted in red to indicate the crack position.

To evaluate the effect of the fracture toughening mechanisms, the evolution of the normalized crack length (the integral of the last term in Eq. (20) without the factor G_c^{poly}) is plotted in Fig. 25 as a function of the load step w. Both the fine- and coarse-grain graphs start from zero (intact model), and are almost identical until the cracks initiate at load step $w = 1.17$. After this point, the crack in the fine-grain structure starts to propagate abruptly, i.e. a small increase of the load leads to a big jump in the crack length. This is because after cutting the first grain, the crack starts to propagate faster along the grain boundaries with the lower fracture toughness. Interestingly, the abrupt propagation stops at load step $w = 1.2$ (point $\boldsymbol{a}$ in the fine-grain graph). Simulation results show that this crack arrest is due to crack deflection along the grain boundary. This phenomena is the so-called crack deflection toughening in intergranular mode of fracture (Faber and Evans, 1983; Kueck et al., 2008). The crack shows this behavior in other load steps $\boldsymbol{b}$ and $\boldsymbol{c}$.

Regarding the crack propagation in the coarse-grain microstructure, its crack-length graph in Fig. 25 shows a slower growth rate than the fine-grain structure. This is mainly due to the fact that, the transgranular mode of fracture in the coarse-grain structure allows the crack to interact with the ferroelectric domain microstructure inside the grains. Due to the high tensile stresses around the fracture zone, the polarization vectors start to rotate towards the vertical direction which leads to 90^o ferroelastic domain switching mentioned in Section

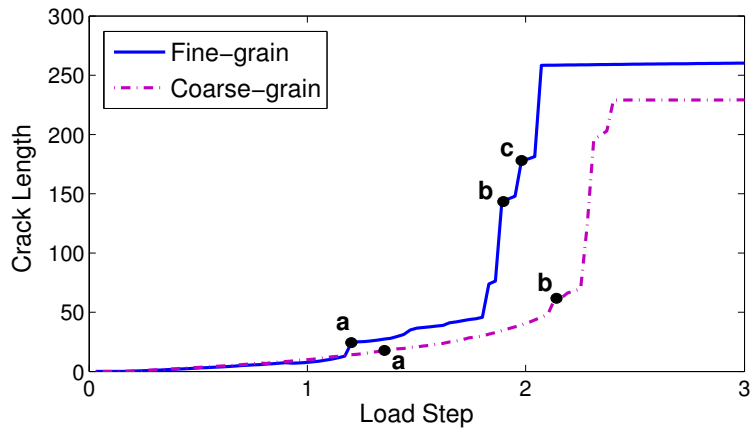

Figure 25: Evolution of the normalized crack length as a function of the load step.

3. Therefore the main toughening mechanism in a coarse-grain ferroelectric polycrystal is the domain switching-induced toughening. In contrast, 90^o ferroelastic switching is less pronounced in the fine-grain structure since the crack propagates faster along the grain boundaries with a lower applied load. Therefore the effective fracture toughness of the coarse-grain structure is higher than the fine-grain, which agrees with experiments (Meschke et al., 1997).

Contributions

We summarize here the most significant contributions of this work, which has been published as a research paper in (Abdollahi and Arias, 2012b):

1. We perform, to the best of our knowledge, the first simulation of crack propagation in ferroelectric polycrystals with the goal of qualitatively evaluating the effect of the grain size and ferroelectric domain microstructures on the fracture process. For this purpose, we extend to polycrystals a phase-field model of fracture in ferroelectric single-crystals by incorporating the differential fracture toughness of the bulk and grain boundaries, and different crystal orientations of the grains.

2. Simulation results show intergranular and transgranular crack propagations in fine- and coarse-grain structures, respectively. Crack deflection is observed as the main toughening mechanism in the intergranular mode of fracture in the fine-grain structure. On the other hand, as transgranular fracture is the dominant mode in coarse-

grain microstructures, the crack interacts with the ferroelectric domains inside the grains. In particular, 90^o ferroelastic domain switching results in a considerable fracture toughening effect. All these observations agree with experiment.

Open lines for research

We next discuss some open ideas for research derived from the work performed:

1. The relative physical size of the grains and ferroelectric domains should be considered for more realistic simulations. Besides the grain size, the model presents three lengthscales: (1) the width of the grain boundaries, (2) the width of the ferroelectric domain walls, and (3) the width of the smeared cracks. The first two lengthscales can be estimated experimentally. The latter is a numerical artifact, which could have a significant effect on the simulation results. A sensitivity analysis on the regularization parameter of the fracture phase-field relative to the other lengthscales of the problem would be necessary, as well as an extension to three dimensions.

2. Although domain switching is claimed to be the main toughening mechanism in coarse-grain ferroelectric polycrystals, the intrinsic anisotropy of the crystal in each grain is bound to have an effect as well.

8 Conducting crack propagation driven by electric fields in ferroelectric ceramics

Several experiments have reported electric-field induced crack growth of ferroelectric ceramics from insulating notches and related theories for calculating energy release rates (Lynch et al., 1995; Lucato et al., 2002; Liu et al., 2002; Lucato et al., 2003; Niefanger et al., 2004; Shieh et al., 2006; Westram et al., 2007; Westrain et al., 2007; Jiang and Fang, 2007; Jiang et al., 2009). However, theoretical approaches show that electric field loading, perpendicular to an insulating crack, decreases the total energy release rate, i.e. electric fields retard the crack propagation (Suo, 1991; Park and Sun, 1995; McMeeking, 1999, 2004; Landis, 2004a; Schneider, 2007; Li et al., 2008). This discrepancy indicates that the induced strain incompatibility around the notch is the main cause of crack propagation rather than electrostatic forces. In contrast, electric fields parallel to a conducting crack increase the total energy release rate, which enhance the crack propagation (Suo, 1991, 1993; Yang and Suo, 1994; Qian et al., 1998; Schneider, 2007). Experiments on conducting cracks also show the fracture of ferroelectric ceramics under purely electrical loading (Fu and Zhang, 2000; Zhang et al., 2003; Zhang and Gao, 2004; Zhang et al., 2004, 2007; Beom et al., 2009). Most of these experimental results imply that the major driving force to propagate the conducting cracks is the electrostatic force due to the accumulation of charges with the same sign at the crack tip. The fracture behavior of conducting cracks has been also investigated under combined mechanical and electrical loads (Heyer et al., 1998; Gehrig et al., 2008).

The above mentioned models for the conducting cracks are useful to analyze the electromechanical fields near the crack tips. Most of these models are based on simplified electrostrictive or linear piezoelectricity theories which do not consider the nonlinear effects of the domain switching in ferroelectrics. Related approaches have been developed to consider these effects and to investigate the toughening of conducting cracks due to domain switching (Rajapakse and Zeng, 2001; Jeong and Beom, 2004; Beom and Youn, 2004), which rely on a simple small-scale switching criterion (Hwang et al., 1995). However, all of these models assume fixed crack configurations and they are unable to study the crack propagation mechanisms in ferroelectric ceramics. In this section, we aim at extending the phase-field theory proposed in Section 5 to model conducting crack propagation in ferroelectric ceramics and investigating the crack propagation mechanisms under purely electrical loading.

In the framework of sharp-crack models, a conducting crack is equivalent to assuming that the crack surfaces are coated with perfectly conducting electrode. Therefore the electric potential all over the crack is constant and the electric field inside the crack gap is zero. This condition can also be obtained by filling the crack gap with a conducting fluid or electrolyte such as NaCl solution (Heyer et al., 1998; Gehrig et al., 2008) or silver paint (Zhang et al., 2003, 2004). The crack-gap filling electrolyte resembles an internal conducting layer with infinite permittivity. In the context of phase-field models, this layer can be defined in a smeared way by modifying the electro-mechanical enthalpy in Eq. (16) in such a way that the permittivity reaches infinity inside the fractured zone ($v = 0$). This is done by multiplying the vacuum permittivity ε_0 by the jump set function $1/(v^2 + \varepsilon_c^{-1})$, where ε_c is the relative permittivity of the fractured zone. Then the electro-mechanical enthalpy density in Eq. (16) is modified for a conducting crack as

$$W_c(\boldsymbol{\varepsilon}, \boldsymbol{p}, \phi, v) = (v^2 + \eta_\kappa)[U(\nabla \boldsymbol{p}) + W(\boldsymbol{p}, \boldsymbol{\varepsilon})] + \chi(\boldsymbol{p}) + \nabla\phi \cdot \boldsymbol{p} - \frac{1}{(v^2 + \varepsilon_c^{-1})} \frac{\varepsilon_0}{2} |\nabla\phi|^2, \quad (21)$$

If ε_c is chosen sufficiently large, the last term in Eq. (21) will represent the electrical enthalpy of a diffuse conducting layer, which is shown schematically in Fig. 26. The jump set function $1/(v^2 + \varepsilon_c^{-1})$ does not alter the vacuum permittivity outside of the fracture zone ($v = 1$) since ε_c^{-1} is an infinitesimal value. On the other hand, this function attains its maximum for $v = 0$, encoding the conditions of a conducting layer with the large relative permittivity ε_c inside the fractured zone. A semi-conducting layer is defined as a smooth transition between the insulating vacuum and conducting layers ($0 < v < 1$). When the regularization parameter κ tends to zero, this transition becomes sharper and the semi-conducting layer tends to disappear. It can be seen that, in the limit of vanishingly small regularization parameter, the proposed phase-field model recovers the conditions of the sharp conducting crack. Note that this formulation together with the energy density W_e in Eq. (15) account for the asymmetric behavior in tension and compression and encode also the free-polarization conditions, as discussed in Section 5. The governing equations, material parameters and a solution algorithm are presented in detail in Appendix C.

To perform numerical simulations, we consider a square domain presented in Fig. 27. The initial polarization $\boldsymbol{p}_0$ is along the positive horizontal direction. Similar to experimental

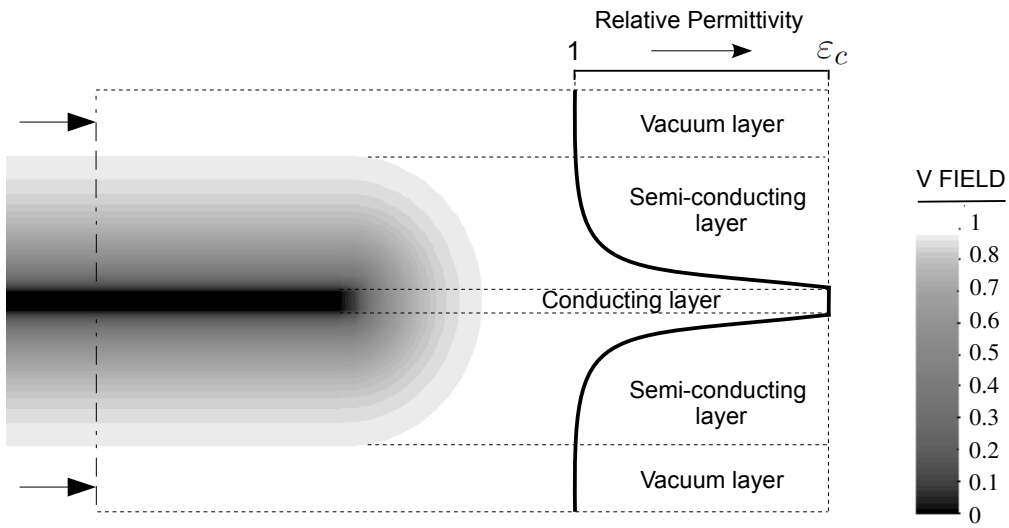

Figure 26: Schematic of a diffuse conducting layer.

setups and to facilitate the crack initiation, a sharp pre-notch is considered in the model parallel to the initial polarization. The model and notch dimensions are chosen as $L_1 = 10$ mm, $L_n = 5$ mm and $W = 50$ nm. To create a conducting notch, the electric potential is fixed to zero on the notch surface and left boundary of the model. Therefore, different electrical loadings can be applied in the horizontal direction by giving different values to the driving voltage V. The model is discretized with approximately 100,000 triangular finite elements of different sizes. The fine mesh with element size $h = 1$ nm is generated in a small square area of size $L_2 = 200$ nm around the notch, presented in Fig. 27(b), where fracture is expected. This element size is small enough for the regularization of the ferroelectric domain walls with a thickness of few nanometers Stemmer et al. (1995); Floquet et al. (1997). The rest of the domain is meshed with larger elements. An electric field $E = -V/L_1$ of up to 1.4 KV/mm is applied incrementally in the positive and negative directions by increasing the driving voltage V through $75,000$ time steps with a load function $V(t) = \pm At$, where $A = 18.75$ V/s, and a time step $\Delta t = 10^{-2}$ s. The initial data of the model are set as $\boldsymbol{u}_0 = \mathbf{0}$, $\phi_0 = 0$, and $v_0 = 1$.

Figure 28 presents two snapshots of the crack propagation in a small neighborhood of the notch tip under the positive electric field. As the electric field increases, the v field starts to decrease at two points of the circular tip until it reaches the threshold to be

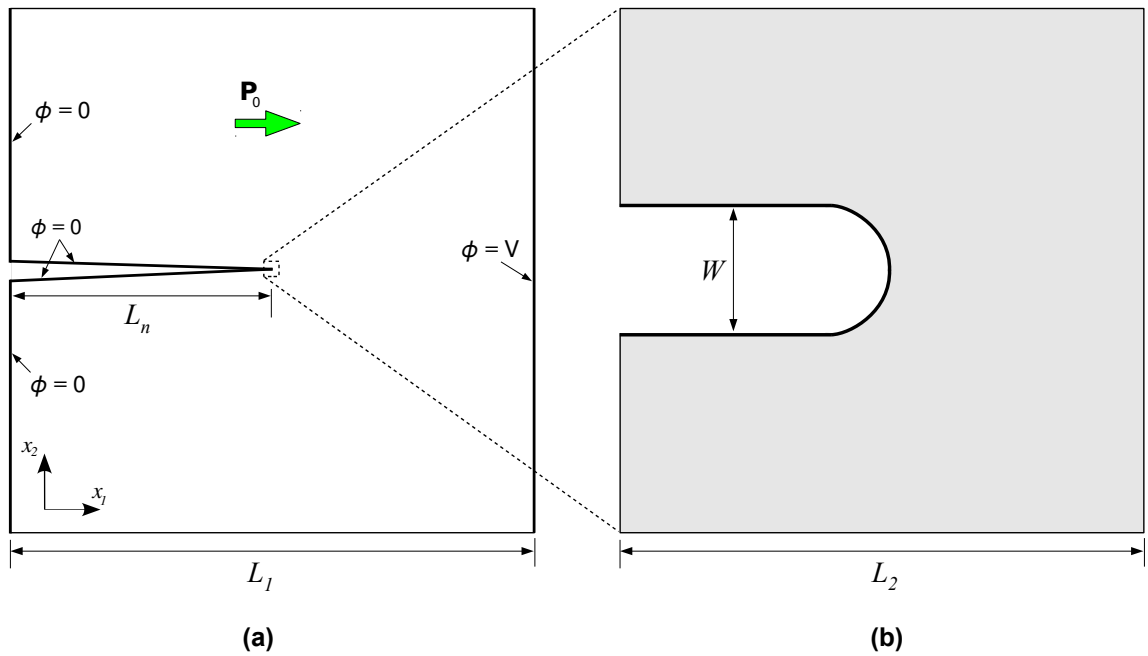

Figure 27: (a) Schematic of the computational domain and loading conditions. The initial polarization $\boldsymbol{p}_0$ is along the positive horizontal direction. A sharp pre-notch is considered in the model (b) small square area around the notch tip, where fracture is expected.

considered permanently fractured ($v < 0.02$). By further increasing of the electric field, the v field evolves in two directions from the notch tip. A similar oblique crack propagation and branching is also observed under the negative electric field which is presented in Fig. 29. The main difference is that the cracks under the positive field are more curved and tend to branch again by increasing the load. Interestingly, an oblique crack propagation is also observed in experiments of conducting cracks in ferroelectric ceramics under purely electrical loading (Zhang et al., 2004). Another experiment has also reported the formation of a micro-cracks network driven by electric fields (Gehrig et al., 2008). Our simulation results also show that the cracks are longer under the negative electric field, cf. Fig 28 and 29. Again, this is in agreement with experiments which have shown that electric fields in opposite to the initial polarization strongly facilitate the conducting fracture (Gehrig et al., 2008).

The origin of the observed crack patterns can be found in the domain switching during crack growth. Figure 30 presents snapshots of the domain evolution in an area around the

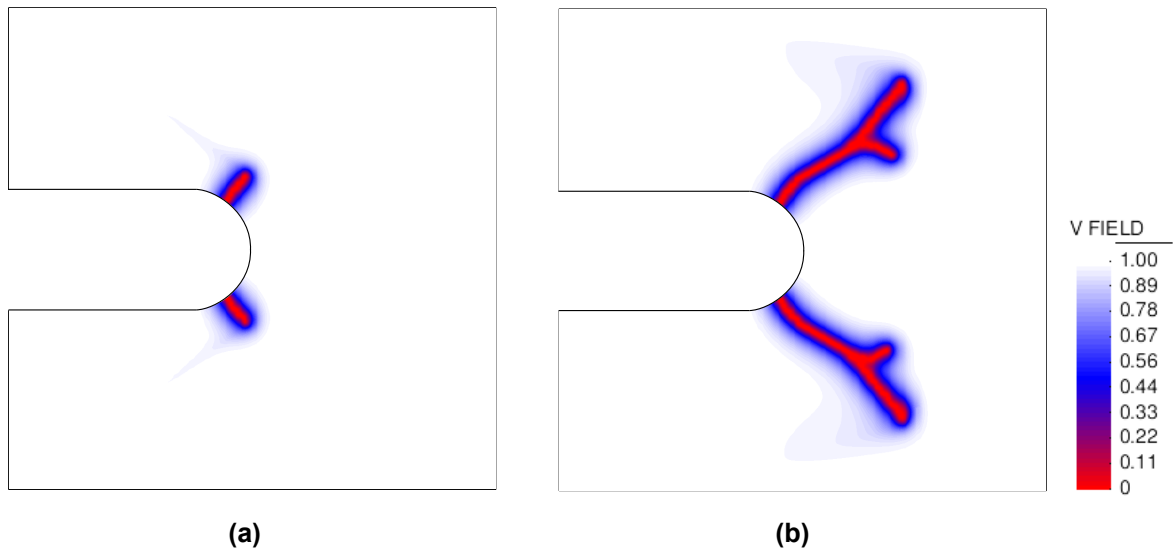

Figure 28: Two snapshots of the fracture evolution: contour plots of the field v under positive electric fields (a) $E = 1.12$ KV/mm (b) $E = 1.4$ KV/mm.

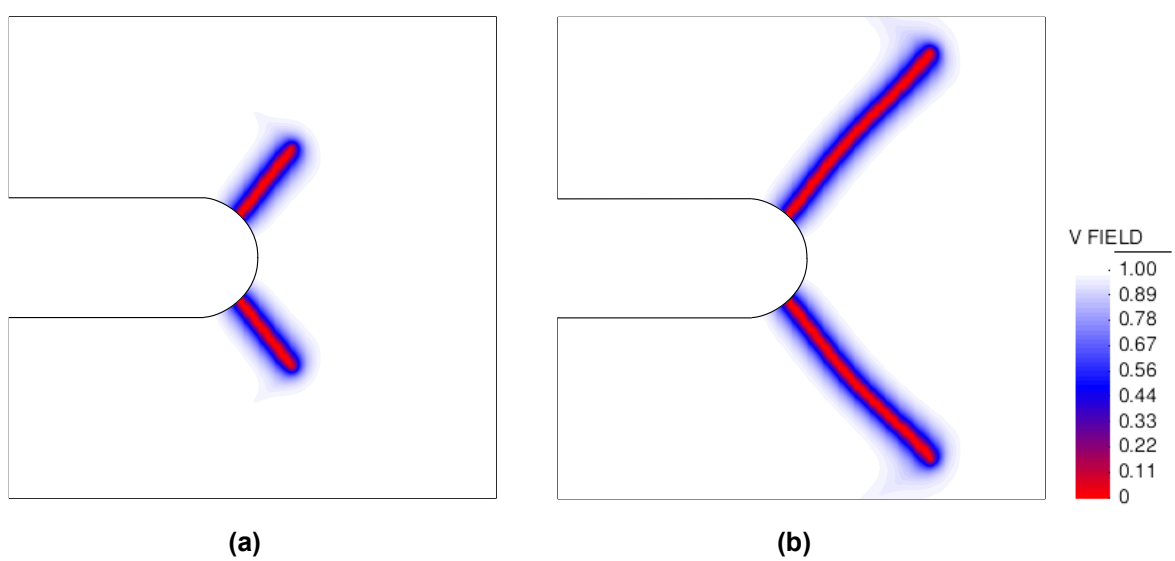

Figure 29: Two snapshots of the fracture evolution: contour plots of the field v under negative electric fields (a) $E =$ -1.12 KV/mm (b) $E =$ -1.4 KV/mm.

notch tip under positive and negative electric fields. Charge accumulation occurs around the cracks through the formation of tail-to-tail and head-to-head 90^o domains in Fig. 30(a) and (b), respectively. This charge accumulation with the same sign induces a high electric field at the crack tip, which in turn leads to a large electrostatic energy (last term in Eq. (21)) for driving the crack. The formation of new twins is responsible for the nucleation of small crack branches under the positive electric field, see Fig. 30(a). Polarization reversal in front of the notch is also obvious in Fig. 30(b) under the negative electric field.

Contributions

We summarize here the most significant contributions of this work, which has been prepared for publication as a research paper:

1. We perform, to the best of our knowledge, the first simulation of conducting crack propagation in ferroelectric ceramics under purely electrical loading. For this purpose, we extend to conducting cracks, a phase-field model of fracture in ferroelectric ceramics by introducing the electrical enthalpy of a diffuse conducting layer into the phase-field formulation.

2. Simulation results show an oblique crack propagation and crack branching from a conducting notch in a ferroelectric sample. Charge accumulation is observed as the main source to induce a large electrostatic force for driving the conducting cracks. A negative electric field induces a larger driving force with respect to the positive one. All these observations agree with experiment.

Open lines for research

We next discuss some open ideas for research derived from the work performed:

1. Dielectric breakdown often occurs during the propagation of conducting cracks, which can release a large amount of thermal energy. This energy may affect the material properties or may induce a thermal stress around the cracks. Therefore, a thermo-electro-mechanical analysis is required to study this effect.

2. Dielectric breakdown mechanisms can be modeled in a similar way to that of conducting crack propagation since a high electric field is considered to be the main cause of dielectric breakdown.

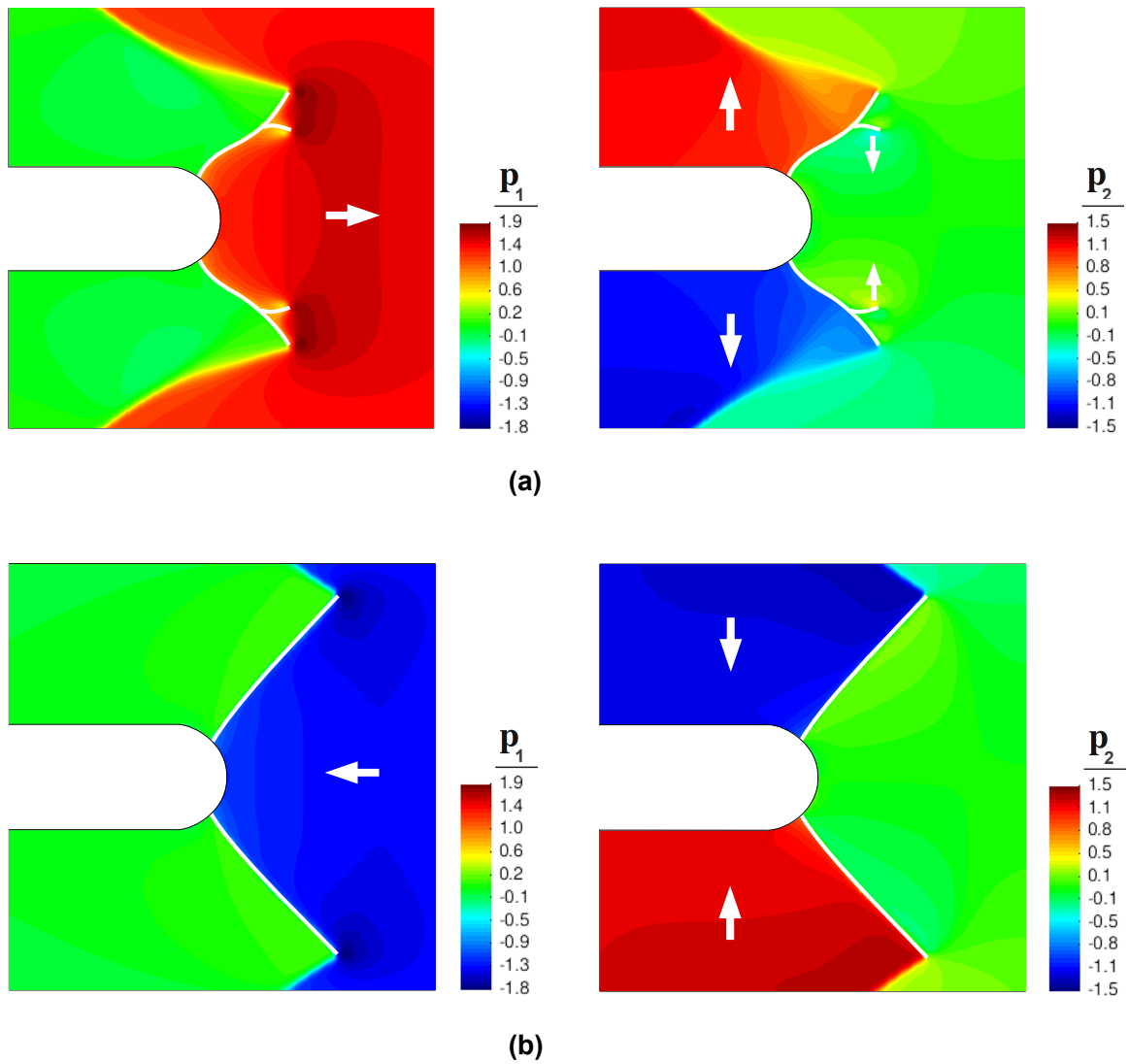

Figure 30: Snapshot of the microstructure evolution in an area near the notch tip under (a) positive and (b) negative electric fields with a magnitude of $|E| = 1.4$ KV/mm. The left and right columns show the horizontal and vertical components of the polarization, respectively. The white lines indicate the position of the cracks ($v = 0$). The domain orientations are indicated with white arrows.

9 Numerical simulation of 3-D crack propagation in ferroelectric single crystals

We extend the phase-field model of fracture in ferroelectric single crystals proposed in Section 3 to three dimensions for a more precise evaluation of the microstructure effect on the crack propagation. Here we consider a traction-free, free-polarization and permeable crack. The electro-mechanical enthalpy density of a possibly fractured ferroelectric for these conditions is stated in Eq. (9) as

$$\begin{aligned} h(\boldsymbol{\varepsilon}, v, \mathbf{p}, \nabla\mathbf{p}, \mathbf{E}) &= (v^2+\eta_\kappa)\left[U(\nabla\mathbf{p}) + W(\mathbf{p},\boldsymbol{\varepsilon})\right] - \frac{\varepsilon_0}{2}|\mathbf{E}|^2 - \mathbf{E}\cdot\mathbf{p} \\ &+ \chi(\mathbf{p}) + G_c\left[\frac{(1-v)^2}{4\kappa} + \kappa|\nabla v|^2\right], \end{aligned} \tag{22}$$

Following (Su and Landis, 2007), the energy functions U, W and χ are expanded in terms of three-dimensional components as

$$U(p_{i,j}) = \frac{a_0}{2}(p_{1,1}^2 + p_{2,2}^2 + p_{3,3}^2 + p_{1,2}^2 + p_{2,1}^2 + p_{1,3}^2 + p_{3,1}^2 + p_{2,3}^2 + p_{3,2}^2), \tag{23}$$

$$\begin{aligned} W(p_i, \varepsilon_{jk}) = &-\frac{b_1}{2}(\varepsilon_{11}p_1^2 + \varepsilon_{22}p_2^2 + \varepsilon_{33}p_3^2) \\ &-\frac{b_2}{2}\left((\varepsilon_{22}+\varepsilon_{33})p_1^2 + (\varepsilon_{11}+\varepsilon_{33})p_2^2 + (\varepsilon_{11}+\varepsilon_{22})p_3^2\right) \\ &- b_3\left((\varepsilon_{12}+\varepsilon_{21})p_1p_2 + (\varepsilon_{13}+\varepsilon_{31})p_1p_3 + (\varepsilon_{23}+\varepsilon_{32})p_2p_3\right) \\ &+ \frac{c_1}{2}(\varepsilon_{11}^2 + \varepsilon_{22}^2 + \varepsilon_{33}^2) \\ &+ c_2(\varepsilon_{11}\varepsilon_{22} + \varepsilon_{11}\varepsilon_{33} + \varepsilon_{22}\varepsilon_{33}) \\ &+ \frac{c_3}{2}(\varepsilon_{12}^2 + \varepsilon_{21}^2 + \varepsilon_{13}^2 + \varepsilon_{31}^2 + \varepsilon_{23}^2 + \varepsilon_{32}^2), \end{aligned} \tag{24}$$

$$\begin{aligned} \chi(p_i) = &\frac{a_1}{2}(p_1^2 + p_2^2 + p_3^2) + \frac{a_2}{4}(p_1^4 + p_2^4 + p_3^4) + \frac{a_3}{2}(p_1^2p_2^2 + p_2^2p_3^2 + p_1^2p_3^2) \\ &+ \frac{a_4}{6}(p_1^6 + p_2^6 + p_3^6) + \frac{a_5}{4}(p_1^4p_2^4 + p_2^4p_3^4 + p_1^4p_3^4), \end{aligned} \tag{25}$$

where all of the variables and parameters are defined in Section 3 and Appendix A. The governing equations, solution algorithm and normalizations are also presented in Appendix A. The normalized parameters for barium titanate ($BaTiO_3$) are given in Table 5.

Table 5: Normalized parameters

c_1'	c_2'	c_3'	b_1'	b_2'	b_3'	a_0'
185	111	74	1.4282	-0.185	0.8066	0.02

a_1'	a_2'	a_3'	a_4'	a_5'	ε_0'	G_c'
-0.007	-0.009	0.018	0.0261	5	0.131	15.6

For numerical simulations, a cubic domain is considered with the boundary conditions depicted in Fig. 31. The normalized dimensions of the domain are 200×200×200 and it is discretized with approximately 6,000,000 tetrahedral finite elements of size $h \simeq 2$. A monotonically increasing mechanical load is applied by pulling the top and bottom faces of the model with a uniform mechanical displacement such that $\mathbf{u}_{\pm} = (0, \pm w, 0)$, where + and - indicate the top and bottom faces of the model respectively and w is the pseudo-time. To facilitate the crack initiation, the x_2 component of mechanical displacement is also constrained at the top half and bottom half of the front face highlighted with yellow such that $u_{2\pm} = \pm w$. To avoid the compression of the model, the x_3 component of mechanical displacement is fixed on the right (highlighted with green) and left faces. The initial polarization $\mathbf{p}_{init} = (1, 0, 0)$ is assigned along the positive x_1 direction, see Fig. 31. As for the electrical boundary conditions, the electric potential on the front (yellow) and back faces is set to 0. It is also assumed that the normal component of the electric displacement vanishes on other faces and they satisfy the free-polarization boundary conditions. The simulation constants are chosen as follows. The tolerances to achieve steady states for ferroelectric domains and fracture processes to $\delta_{ferro} = 5 \times 10^{-3}$, $\delta_{vfield} = 2 \times 10^{-3}$, the threshold to detect the irreversibly fractured regions to $\alpha = 2 \times 10^{-2}$, the inverse mobilities to $\mu_p = 1$ and $\mu_v = 15$, the residual stiffness to $\eta_\kappa = 10^{-6}$ and the regularization parameter to twice the element size as $\kappa = 4$. One hundred load increments are performed in the simulation ($n = 100$) with the pseudo-time interval of $\Delta w^n = 5 \times 10^{-2}$. Also the normalized time step $\Delta t_m' = 0.1$ leads to convergent and accurate solutions for the semi-implicit integration of gradient flow equations. The simulations are carried out on parallel processors using the finite element library of the Kratos multi-physics package (Dadvand et al., 2010).

Figs. 32 and 33 present the four snapshots of the evolution of the microstructure and

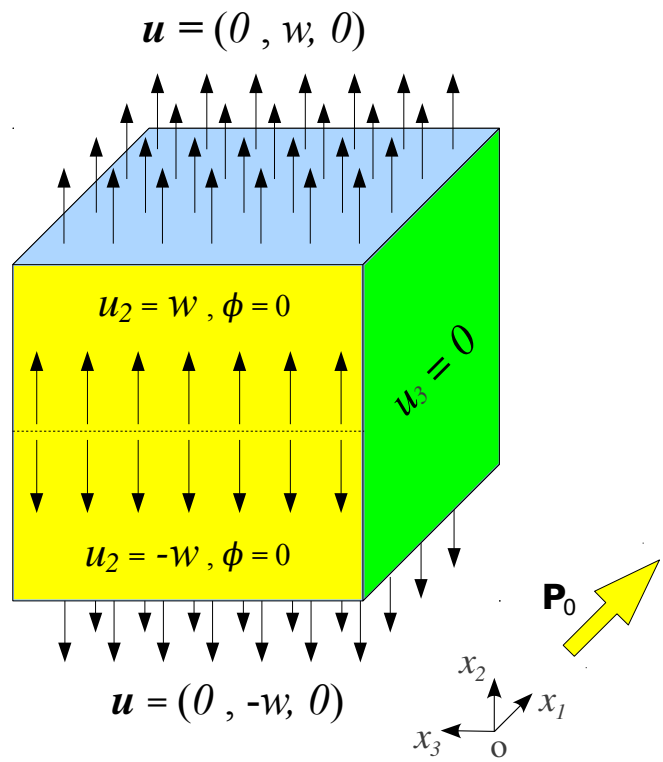

Figure 31: 3-D computational model with boundary conditions.

the crack. The left column shows the field v representing the fractured area and the right column shows the polarization magnitude $|\mathbf{p}|$, which highlights the domain structure. These figures indicate a similar interaction of the crack and ferroelectric domains reported in Section 3 but in this case in three dimensions. This interaction leads to the slow-fast crack propagation behavior. The snapshots in Fig. 32(b), Fig. 33(a) and Fig. 32(b) correspond to slow propagation periods arrested by the twins ahead of the crack represented with bold white arrows. These preliminary results verify the formulation and implementation of the 3-D model. Another purpose of performing this simulation is to optimize the performance of the parallel computing to obtain more sophisticated 3-D results in the future.

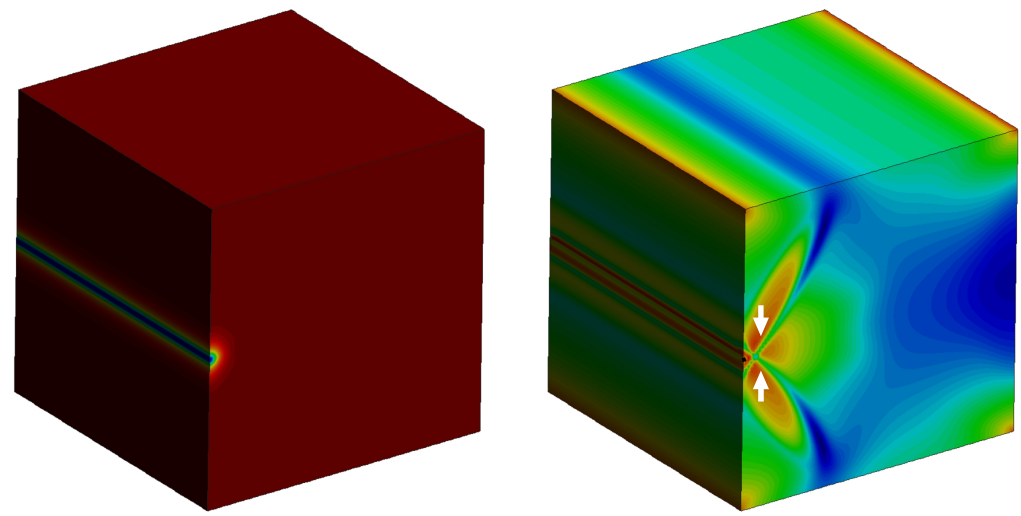

(a)

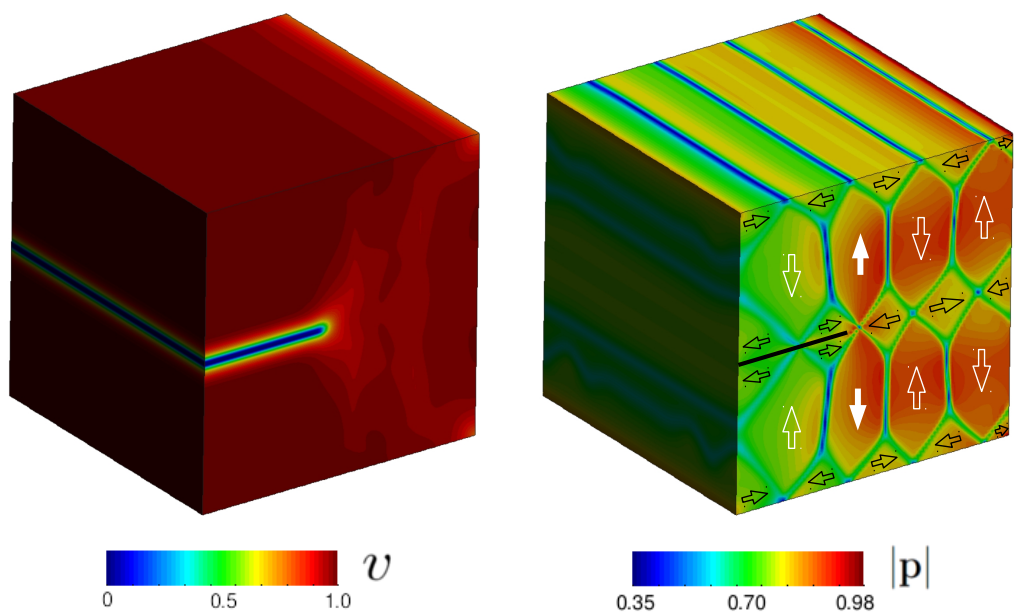

(b)

Figure 32: Two snapshots of the evolution of the microstructure and the permeable crack at load steps (a) $t = 1.5$, (b) $t = 4.35$. The left column shows the field v representing the fractured area, and the right column shows the polarization magnitude $|\mathbf{p}|$, which highlights the domain structure. Domain orientations are indicated with large arrows, which are bold white for the twins ahead of the crack. The points where $v = 0$ are represented in black in the polarization maps to show the crack position.

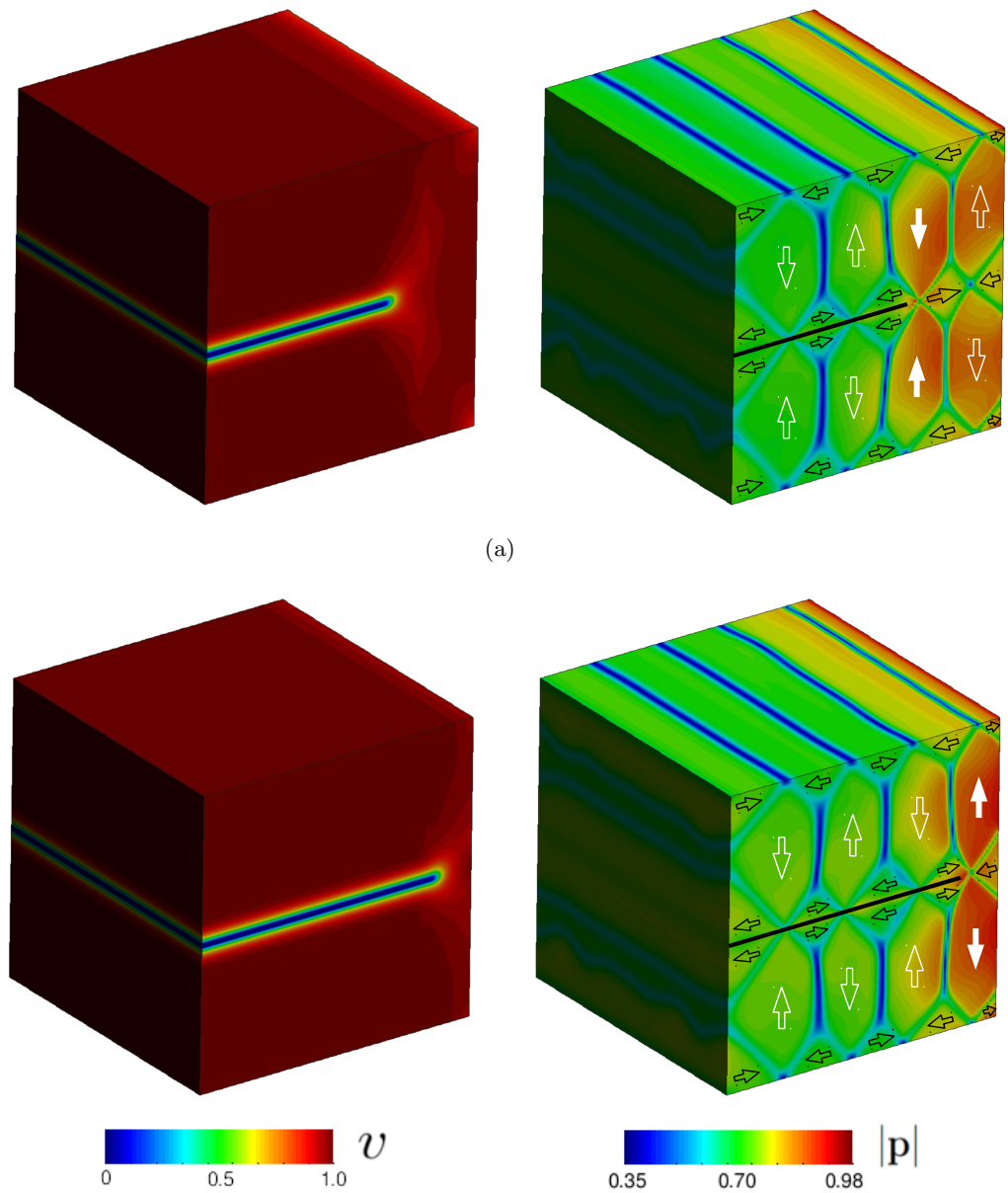

Figure 33: Two snapshots of the evolution of the microstructure and the permeable crack at load steps (a) $t = 4.55$, (b) $t = 4.65$. The left column shows the field v representing the fractured area, and the right column shows the polarization magnitude $|\mathbf{p}|$, which highlights the domain structure. Domain orientations are indicated with large arrows, which are bold white for the twins ahead of the crack. The points where $v = 0$ are represented in black in the polarization maps to show the crack position.

10 Conclusions

This section summarizes the main contributions and research ideas of the thesis. We perform, to the best of our knowledge, the first calculations for the fully coupled interaction between the crack propagation and the formation and evolution of microstructure in ferroelectric materials. For this purpose, a family of phase-field models is proposed in this thesis which is outlined as follows:

- *A phase-field model for the coupled nucleation and evolution of cracks and domains in ferroelectric single crystals*: The model naturally couples two energetic phase-field models for fracture and for the microstructure of ferroelectric single crystals. We exercise the model in plane polarization and plane strain simulations of a sample under either mechanical or combined electro-mechanical loading conditions.

- *Phase-field models to encode various electro-mechanical crack-face boundary conditions*: These models are based on a variational formulation of brittle fracture coupled with the linear theory of piezoelectricity and a phase-field model of ferroelectric domain evolution. This coupling encodes various electro-mechanical crack-face boundary conditions of a sharp-crack into the phase-field framework. We perform a set of simulations to compare the results of the proposed models with that of the corresponding sharp-crack models.

- *A developed phase-field model to explain anisotropic crack growth in ferroelectrics*: The model is developed by introducing a crack non-interpenetration condition in the variational approach to fracture accounting for the asymmetric behavior in tension and compression. We exercise the model under Vickers indentation loading and during the poling process of multilayer ferroelectric actuators.

- *A phase-field model to simulate intergranular and transgranular crack propagation in ferroelectric polycrystals*: The proposed phase-field model for ferroelectric single crystals is extended to polycrystals by incorporating the differential fracture toughness of the bulk and the grain boundaries, and the different crystal orientations of the grains. We exercise the model with fine- and coarse-grain microstructures.

- *A developed phase-field model to simulate conducting crack propagation driven by electric fields*: The model is developed by introducing the electrical enthalpy of a diffuse

conducting layer into the phase-field formulation of fracture in ferroelectric single-crystals. We exercise the model under purely electrical loading.

The main simulation results of the proposed models, which agree with experimental observations, are summarized in the following:

- The interaction of the microstructure and the crack leads to a slow-fast crack propagation behavior in ferroelectric single crystals (Fang et al., 2007).
- 90^o domain switching induced by an intense crack-tip stress field is the major mechanism behind the fracture toughening effect in ferroelectric materials (Meschke et al., 1997, 2000).
- There is not a clear shielding or weakening effect of the microstructure on the crack propagation for low applied electric fields (below the coercive field) parallel to the crack. (Sun and Park, 2000; Tobin and Pak, 1993).
- An enhanced crack propagation is obtained for parallel cracks under applied electric fields with the coercive magnitude (Schneider and Heyer, 1999).
- Radial cracks perpendicular to the poling direction of the material propagate faster than parallel ones (Sun and Park, 2000; Pisarenko et al., 1985; Tobin and Pak, 1993; Wang and Singh, 1997; Lynch, 1998; Schneider and Heyer, 1999).
- Cracks propagate mainly along the grain boundaries in fine-grain ferroelectric polycrystals, demonstrating the intergranular mode of fracture. On the other hand, transgranular crack propagation is observed in coarse-grain microstructures where cracks propagate through the grains (Kim et al., 1990; Meschke et al., 1997).
- Crack deflection is shown as the main toughening mechanism in the fine-grain microstructures (Faber and Evans, 1983; Kueck et al., 2008). Due to the ferroelectric domain switching mechanism, noticeable fracture toughness enhancement is also obtained for transgranular crack propagation and the effective fracture toughness of the coarse-grain microstructures is observed to be higher than the fine-grain (Meschke et al., 1997).
- An air-filled EC crack under the constraint of electrical breakdown behaves similar to a permeable crack (Schneider et al., 2003).

- A negative electric field (below the coercive field) enhances the crack propagation perpendicular to the initial polarization in ferroelectrics, while a positive electric field retards it (Ricoeur and Kuna, 2003; Wang and Singh, 1997; Shindo et al., 2002; Jiang et al., 2009).

- An oblique crack propagation and crack branching from a conducting notch is observed in a ferroelectric sample under purely electrical loading (Zhang et al., 2004). A negative electric field induces a larger driving force with respect to the positive one (Gehrig et al., 2008).

- Different crack initiation patterns are observed at electrode edges in multilayer ferroelectric actuators. The obtained patterns can be interpreted as initiation sources of experimentally observed crack branches near the electrode edge (Uchino and Furuta, 1992; Furuta and Uchino, 1993; Aburatani et al., 1994).

- Crack initiation becomes more difficult by decreasing the thickness of the ceramic layer and the length of the internal electrode in multilayer ferroelectric actuators (Lucato et al., 2001)

We also mention further conclusions from the simulation results:

- Impermeable conditions have the most retarding effect on the crack propagation while this is less significant for EC and permeable conditions. Furthermore, the crack growth rate for the EC conditions lies between that of the permeable and impermeable conditions.

- A water-filled crack shows a similar behavior to a permeable crack due to the high dielectric permittivity of water. The effect of electrical loads on the crack growth is more pronounced in silicon-oil and air-filled cracks due to the lower permittivities of these media.

- Impermeable and EC conditions have a significant influence on the polarization fields around the cracks.

- The effects of electrical conditions on ferroelectric domain structures around the cracks are significantly more than zero- and free-polarization conditions.

The work carried out in this thesis also leaves some open research lines for the future. We suggest the following lines:

- Experimental observations in (Fang et al., 2007) reveal that the crack propagates along the cleavage plane [101] in $BaTiO_3$, following a zig-zag path that matches the domain pattern. This can be included in our model by considering a lower surface energy or fracture toughness along the cleavage planes.

- Relative magnitude of the mobility parameters can have an important effect on the resulting response. A parametric study is needed for evaluating the effect of these parameters.

- A more precise evaluation of the microstructure effect will be obtained by extending the proposed models to three dimensions and running longer simulations producing more extended cracks.

- The relative physical size of the grains and ferroelectric domains should be considered for more realistic fracture simulations of ferroelectric polycrystals. Besides the grain size, the model presents three lengthscales: (1) the width of the grain boundaries, (2) the width of the ferroelectric domain walls, and (3) the width of the smeared cracks. The first two lengthscales can be estimated experimentally. The latter is a numerical artifact, which could have a significant effect on the simulation results. A sensitivity analysis on the regularization parameter of the fracture phase-field relative to the other lengthscales of the problem would be necessary.

- Dielectric breakdown often occurs via the formation of conducting tubular channels around electrodes and conducting cracks, which can release a large amount of thermal energy. This energy may affect the material properties or may induce a thermal stress. Therefore, a thermo-electro-mechanical analysis is required to investigate this effect. Furthermore, the formation and propagation of the tubular channels can have an important effect on the electromechanical fields and the microstructure of the material.

Bibliography

Abdollahi, A. and I. Arias (2011a). Phase-field modeling of the coupled microstructure and fracture evolution in ferroelectric single crystals. *Acta Materialia 59*(12), 4733–4746.

Abdollahi, A. and I. Arias (2011b). Phase-field simulation of anisotropic crack propagation in ferroelectric single crystals: effect of microstructure on the fracture process. *Modelling and Simulation in Materials Science and Engineering 19*(7), 074010.

Abdollahi, A. and I. Arias (2012a). Crack initiation patterns at electrode edges in multilayer ferroelectric actuators. *Smart Materials and Structures 21*, 094011.

Abdollahi, A. and I. Arias (2012b). Numerical simulation of intergranular and transgranular crack propagation in ferroelectric polycrystals. *International Journal of Fracture 174*(1), 3–15.

Abdollahi, A. and I. Arias (2012c). Phase-field modeling of crack propagation in piezoelectric and ferroelectric materials with different electro-mechanical crack conditions. *Journal of the Mechanics and Physics of Solids 60*, 2100–2126.

Aburatani, H., S. Harada, K. Uchino, A. Furuta, and Y. Fuda (1994). Destruction mechanisms in ceramic multilayer actuators. *Japanese Journal of Applied Physics 1 33*, 3091–3094.

Amor, H., J. J. Marigo, and C. Maurini (2009). Regularized formulation of the variational brittle fracture with unilateral contact: Numerical experiments. *Journal of the Mechanics and Physics of Solids 57*(8), 1209–1229.

Arias, I., S. Serebrinsky, and M. Ortiz (2006). A phenomenological cohesive model of ferroelectric fatigue. *Acta Materialia 54*(4), 975–984.

Belytschko, T., H. Chen, J. X. Xu, and G. Zi (2003). Dynamic crack propagation based on loss of hyperbolicity and a new discontinuous enrichment. *International Journal for Numerical Methods in Engineering 58*(12), 1873–1905.

Benes, M., V. Chalupecky, and K. Mikula (2004). Geometrical image segmentation by the Allen-Cahn equation. *Applied Numerical Mathematics 51*(2-3), 187–205.

Beom, H. G. and S. N. Atlurib (2003). Effect of electric fields on fracture behavior of ferroelectric ceramics. *Journal of the Mechanics and Physics of Solids 51*, 1107–1125.

Beom, H. G., K. M. Jeong, J. Y. Park, S. Lin, and G. H. Kim (2009). Electrical failure of piezoelectric ceramics with a conductive crack under electric fields. *Engineering Fracture Mechanics 76*, 2399–2407.

Beom, H. K. and S. K. Youn (2004). Electrical fracture toughness for a conducting crack in ferroelectric ceramics. *International Journal of Solids and Structures 41*(1), 145–157.

Bourdin, B. (2007). Numerical implementation of the variational formulation for quasi-static brittle fracture. *Interfaces and Free Boundaries 9*, 411–430.

Bourdin, B., G. A. Francfort, and J. J. Marigo (2000). Numerical experiments in revisited brittle fracture. *Journal of the Mechanics and Physics of Solids 48*(4), 797–826.

Bourdin, B., G. A. Francfort, and J. J. Marigo (2008). The variational approach to fracture. *Journal of Elasticity 91*(1-3), 5–148.

Camacho, G. T. and M. Ortiz (1996). Computational modelling of impact damage in brittle materials. *International Journal for Numerical Methods in Engineering 33*(20-22), 2899–2938.

Dadvand, P., R. Rossi, and E. Onate (2010). An object-oriented environment for developing finite element codes for multi-disciplinary applications. *Archives of Computational Methods in Engineering 17*(3), 253–297.

Dayal, K. and K. Bhattacharya (2007). A real-space non-local phase-field model of ferroelectric domain patterns in complex geometries. *Acta Materialia 55*(6), 1907–1917.

Deeg, W. F. J. (1980). *The analysis of dislocation, crack, and inclusion problems in piezoelectric solids*. Ph. D. thesis, Stanford University.

DeSimone, A. and R. D. James (2002). A constrained theory of magnetoelasticity. *Journal of the Mechanics and Physics of Solids 50*, 283–320.

DeSimone, A., R. V. Kohn, S. Müller, F. Otto, and R. Schäfer (2001). Two-dimensional modeling of soft ferromagnetic films. *Proceedings of the Royal Society A 457*, 2983–2991.

Devonshire, A. F. (1949). Theory of barium titanate .1. *Philosophical Magazine 40*(309), 1040–1063.

Devonshire, A. F. (1951). Theory of barium titanate .2. *Philosophical Magazine 42*(333), 1065 –1079.

Elhadrouz, M., T. B. Zineb, and E. Patoor (2006). Finite element analysis of a multilayer piezoelectric actuator taking into account the ferroelectric and ferroelastic behaviors. *International Journal of Engineering Science 44*, 996–1006.

Faber, K. T. and A. G. Evans (1983). Intergranular crack-deflection toughening in silicon-carbide. *Journal of the American Ceramic Society 66*(6), C94–C96.

Fan, D. and L. Q. Chen (1997). Computer simulation of grain growth using a continuum field model. *Acta Materialia 45*(2), 611–622.

Fang, D., S. L. Y. Jiang, and C. T. Sun (2007). Interactions between domain switching and crack propagation in poled BaTiO3 single crystal under mechanical loading. *Acta Materialia 55*(17), 5758–5767.

Floquet, N., C. M. Valot, M. T. Mesnier, J. C. Niepce, L. Normand, A. Thorel, and R. Kilaas (1997). Ferroelectric domain walls in BaTiO3: Fingerprints in XRPD diagrams and quantitative HRTEM image analysis. *Journal de Physique III 7*, 1105–1128.

Francfort, G. A. and J. J. Marigo (1998). Revisiting brittle fracture as an energy minimization problem. *Journal of the Mechanics and Physics of Solids 46*(8), 1319–1342.

Fu, R., C. F. Qian, and T. Y. Zhang (2000). Electrical fracture toughness for conductive cracks driven by electric fields in piezoelectric materials. *Applied Physics Letters 76*(1), 126–128.

Fu, R. and T. Y. Zhang (2000). Effects of an electric field on the fracture toughness of poled lead zirconate titanate ceramics. *Journal of the American Ceramic Society 83*(5), 1215–1218.

Furuta, A. and K. Uchino (1993). Dynamic observation of crack-propagation in piezoelectric multilayer actuators. *Journal of the American Ceramic Society 76*, 1615–1617.

Gao, H. J., T. Y. Zhang, and P. Tong (1997). Local and global energy release rates for an electrically yielded crack in a piezoelectric ceramic. *Journal of the Mechanics and Physics of Solids 45*(4), 491–510.

Gehrig, F., H. Jelitto, and G. A. Schneider (2008). Fracture criterion for a conducting crack in poled PZT-PIC 151 investigated by stable crack growth. *Acta Materialia 56*(2), 222–229.

Gong, X. and Z. Suo (1996). Reliability of ceramic multilayer actuators: A nonlinear finite element simulation. *Journal of the Mechanics and Physics of Solids 44*, 751–769.

Grah, M., K. Alzebdeh, P. Y. Sheng, M. D. Vaudin, K. J. Bowman, and M. Ostoja-Starzewski (1996). Brittle-intergranular failure in 2D microstructures: Experiments and computer simulations. *Acta Materialia 44*(10), 4003–4018.

Griffith, A. A. (1921). The phenomena of rupture and flow in solids. *Philosophical Transactions of the Royal Society of London Series A-221*, 163–198.

Guo, X. H., D. N. Fang, A. K. Soh, H. C. Kim, and J. J. Lee (2006). Analysis of piezoelectric ceramic multilayer actuators based on an electro-mechanical coupled meshless method. *Acta Mechanica Sinica 22*, 34–39.

Hackemann, S. and W. Pfeiffer (2003). Domain switching in process zones of pzt: characterization by microdiffraction and fracture mechanical methods. *Journal of the European Ceramic Society 23*(1), 141–151.

Han, X., X. Li, and S. X. Mao (2002). Toughening and weakening in ferroelectric ceramics by domain-switching process under mixed electric and mechanical loading. *Metallurgical and Materials Transactions A 33*(9), 2835–2845.

Hao, T. H., X. Gong, and Z. Suo (1996). Fracture mechanics for the design of ceramic multilayer actuators. *Journal of the Mechanics and Physics of Solids 44*, 23–48.

Hao, T. H. and Z. Y. Shen (1994). A new electric boundary-condition of electric fracture-mechanics and its applications. *Engineering Fracture Mechanics 47*(6), 793–802.

Haug, A. and R. M. McMeeking (2006). Cracks with surface charge in poled ferroelectrics. *European Journal of Mechanics A/Solids 25*(1), 24–41.

Heyer, V., G. A. Schneider, H. Balke, J. Drescher, and H. A. Bahr (1998). A fracture criterion for conducting cracks in homogeneously poled piezoelectric pzt-pic 151 ceramics. *Acta Materialia 46*(18), 6615–6622.

Huber, J. E. (2005). Micromechanical modelling of ferroelectrics. *Current Opinion in Solid State and Materials Science 9*(3), 100–106.

Hwang, S. C., C. S. Lynch, and R. M. McMeeking (1995). Ferroelectric/ferroelastic interactions and a polarization switching model. *Acta Materialia 43*(5), 2073–2084.

Jacqmin, D. (1999). Calculation of two-phase Navier-Stokes flows using phase-field modeling. *Journal of Computational Physics 155*(1), 96–127.

Jeong, K. M. and H. G. Beom (2004). Conducting crack growth in ferroelectric ceramics subjected to electric loading. *Smart Materials and Structures 13*(2), 275.

Jiang, Y. and D. Fang (2007). In situ observation of electric-field-induced domain switching and crack propagation in poled PMNT62/38 single crystals. *Materials Letters 61*(28), 5047–5049.

Jiang, Y., Y. Zhang, B. Liu, and D. Fang (2009). Study on crack propagation in ferroelectric single crystal under electric loading. *Acta Materialia 57*, 1630–1638.

Jones, L. J., S. M. Motahari, M. VarlioglU, U. Lienert, J. V. Bernier, M. Hoffman, and E. Uestuendag (2007). Crack tip process zone domain switching in a soft lead zirconate titanate ceramic. *Acta Materialia 55*(16), 5538–5548.

Kamlah, M. (2001). Ferroelectric and ferroelastic piezoceramics - modeling of electromechanical hysteresis phenomena. *Continuum Mechanics and Thermodynamics 13*(4), 219–268.

Kamlah, M. and U. Bohle (2001). Finite element analysis of piezoceramic components taking into account ferroelectric hysteresis behavior. *International Journal of Solids and Structures 38*, 605–633.

Kanzig, W. (1957). Ferroelectrics and antiferroelectrics. In F. Seitz, T. P. Das, D. Turnbull, and E. L. Hahn (Eds.), *Solid State Physics*, pp. 5. Academic Press.

Kim, S. B., D. Y. Kim, J. J. Kim, and S. H. Cho (1990). Effect of grain-size and poling on the fracture mode of lead zirconate titanate ceramics. *Journal of the American Ceramic Society 73*(1), 161–163.

Koh, J. H., S. J. Jeong, M. S. Ha, and J. S. Song (2004). Electric field induced fracture mechanism and aging of piezoelectric behavior in Pb(MgNb)O-3-Pb(ZrTi)O-3 multilayer ceramic actuators. *Ceramics International 30*, 1863–1867.

Krill, C. E. and L. Q. Chen (2002). Computer simulation of 3-D grain growth using a phase-field model. *Acta Materialia 50*(12), 3057–3073.

Kueck, A. M., D. K. Kim, Q. M. Ramasse, L. C. De Jonghe, and R. O. Ritchie (2008). Atomic-resolution imaging of the nanoscale origin of toughness in rare-earth doped SiC. *Nano Letters 8*(9), 2935–2939.

Kuna, M. (2010). Fracture mechanics of piezoelectric materials - where are we right now? *Engineering Fracture Mechanics 77*(2), 309–326.

Landau, L. (1937). *On the theory of phase transitions.* Gordon and Breach.

Landis, C. M. (2003). On the fracture toughness of ferroelastic materials. *Journal of the Mechanics and Physics of Solids 51*, 1347–1369.

Landis, C. M. (2004a). Energetically consistent boundary conditions for electromechanical fracture. *International Journal of Solids and Structures 41*(22-23), 6291–6315.

Landis, C. M. (2004b). Non-linear constitutive modeling of ferroelectrics. *Current Opinion in Solid State and Materials Science 8*, 59–69.

Li, J. Y. (2009). On the depolarization energy of ferroelectrics. *Mechanics of Materials 41*(10), 1125–1132.

Li, Q. and M. Kuna (2011). Evaluation of electromechanical fracture behavior by configurational forces in cracked ferroelectric polycrystals. *Computational Materials Science*. DOI: 10.1016/j.commatsci.2011.01.050.

Li, W. and C. M. Landis (2011). Nucleation and growth of domains near crack tips in single crystal ferroelectrics. *Engineering Fracture Mechanics 78*(7), 1505–1513.

Li, W. Y., R. M. McMeeking, and C. M. Landis (2008). On the crack face boundary conditions in electromechanical fracture and an experimental protocol for determining energy release rates. *European Journal of Mechanics A-Solids 27*(3), 285–301.

Li, X. F. and G. J. Tang (2003). Electroelastic analysis for a piezoelectric layer with surface electrodes. *Mechanics Research Communications 30*, 345–351.

Li, Y. L., L. E. Cross, and L. Q. Chen (2005). A phenomenological thermodynamic potential for BaTiO3 single crystals. *Journal of Applied Physics 98*, 064101.

Linder, C. and C. Miehe (2012). Effect of electric displacement saturation on the hysteretic behavior of ferroelectric ceramics and the initiation and propagation of cracks in piezoelectric ceramics. *Journal of the Mechanics and Physics of Solids* (0), –. DOI: 10.1016/j.jmps.2012.01.012.

Lines, M. and A. Glass (1979). *Principles and applications of ferroelectrics and related materials*. Clarendon Press.

Liu, B., D. Fang, and K.-C. Hwang (2002). Electric-field-induced fatigue crack growth in ferroelectric ceramics. *Materials Letters 54*(5-6), 442–446.

Liu, T. Q., W. S. Oates, S. Wan, and C. S. Lynch (2005). Crack initiation at electrode edges in PZN-4.5PT single crystals. *Journal of Intelligent Material Systems and Structures 16*, 373–379.

Lucato, S. L. D. E., H. A. Bahr, V. B. Pham, D. C. Lupascu, H. Balke, J. Rodel, and U. Bahr (2002). Electrically driven cracks in piezoelectric ceramics: experiments and fracture mechanics analysis. *Journal of the Mechanics and Physics of Solids 50*, 2333–2353.

Lucato, S. L. D. E., H. A. Bahr, V. B. Pham, D. C. Lupascu, H. Balke, J. Rodel, and U. Bahr (2003). Crack deflection in piezoelectric ceramics. *Journal of the European Ceramic Society 23*, 1147–1156.

Lucato, S. L. D. E., D. C. Lupascu, M. Kamlah, J. Rodel, and C. S. Lynch (2001). Constraint-induced crack initiation at electrode edges in piezoelectric ceramics. *Acta Materialia 49*, 2751–2759.

Lynch, C. S. (1998). Fracture of ferroelectric and relaxor electro-ceramics: Influence of electric field. *Acta Materialia 46*(2), 599–608.

Lynch, C. S., L. Chen, Z. Suo, R. M. McMeeking, and W. Yang (1995). Crack-growth in ferroelectric ceramics driven by cyclic polarization switching. *Journal of Intelligent Material Systems and Structures 6*, 191–198.

McMeeking, R. M. (1999). Crack tip energy release rate for a piezoelectric compact tension specimen. *Engineering Fracture Mechanics 64*(2), 217–244.

McMeeking, R. M. (2004). The energy release rate for a griffith crack in a piezoelectric material. *Engineering Fracture Mechanics 71*(7-8), 1149–1163.

McMeeking, R. M. and C. M. Landis (2002). A phenomenological multi-axial constitutive law for switching in polycrystalline ferroelectric ceramics. *International Journal of Engineering Science 40*(14), 1553–1577.

Meschke, F., A. Kolleck, and G. A. Schneider (1997). R-curve behaviour of BaTiO3 due to stress-induced ferroelastic domain switching. *Journal of the American Ceramic Society 17*(9), 1143–1149.

Meschke, F., O. Raddatz, A. Kolleck, and G. A. Schneider (2000). R-curve behavior and crack-closure stresses in barium titanate and (mg,y)-psz ceramics. *Journal of the American Ceramic Society 83*(2), 353–361.

Miehe, C., F. Welschinger, and M. Hofacker (2010a). A phase field model of electromechanical fracture. *Journal of the Mechanics and Physics of Solids 58*(10), 1716–1740.

Miehe, C., F. Welschinger, and M. Hofacker (2010b). Thermodynamically consistent phase-field models of fracture: Variational principles and multi-field FE implementations. *International Journal for Numerical Methods in Engineering 83*(10), 1273–1311.

Moes, N., J. Dolbow, and T. Belytschko (1999). A finite element method for crack growth without remeshing. *International Journal for Numerical Methods in Engineering 46*(1), 131–150.

Niefanger, R., V.-B. Pham, G. A. Schneider, H.-A. Bahr, H. Balke, and U. Bahr (2004). Quasi-static straight and oscillatory crack propagation in ferroelectric ceramics due to moving electric field: experiments and theory. *Acta Materialia 52*(1), 117–127.

Oliver, J., A. E. Huespe, M. D. G. Pulido, and E. Chaves (2002). From continuum mechanics to fracture mechanics: the strong discontinuity approach. *Engineering Fracture Mechanics 69*(2), 113–136.

Park, S. B. and C. T. Sun (1995). Fracture criteria for piezoelectric ceramics. *Journal of the American Ceramic Society 78*(6), 1475–1480.

Parton, V. Z. (1976). Fracture mechanics of piezoelectric materials. *Acta Astronautica 3*(9-10), 671–683.

Pisarenko, G. G., V. M. Chushko, and S. P. Kovalev (1985). Anisotropy of fracture toughness of piezoelectric ceramics. *Journal of the American Ceramic Society 68*(5), 259–265.

Pojprapai, S., L. J. Jones, T. Vodenitcharova, J. V. Bernier, and M. Hoffman (2011). Investigation of the domain switching zone near a crack tip in pre-poled lead zirconate titanate ceramic via in situ X-ray diffraction. *Scripta Materialia 64*(1), 1–4.

Pritchard, J., C. R. Bowen, and F. Lowrie (2001). Multilayer actuators: review. *British Ceramic Transactions 100*, 265–273.

Qian, T.-Y., C.-F. Tong, and P. Zhang (1998). Linear electro-elastic analysis of a cavity or a crack in a piezoelectric material. *International Journal of Solids and Structures 35*(17), 2121–2149.

Rajapakse, R. K. N. D. and X. Zeng (2001). Toughening of conducting cracks due to domain switching. *Acta Materialia 49*, 877–885.

Ratz, A., A. Ribalta, and A. Voigt (2006). Surface evolution of elastically stressed films under deposition by a diffuse interface model. *Journal of Computational Physics 214*(1), 187–208.

Ricoeur, A. and M. Kuna (2003). Influence of electric fields on the fracture of ferroelectric ceramics. *Journal of the European Ceramic Society 23*(8), 1313–1328.

Rosato, C., D. Miehe, and C. Linder (2011). New finite elements with embedded strong discontinuities for the modeling of failure in electromechanical coupled solids. *Computer Methods in Applied Mechanics and Engineering 200*(1-4), 141–161.

Ru, C. Q. (2000). Exact solution for finite electrode layers embedded at the interface of two piezoelectric half-planes. *Journal of the Mechanics and Physics of Solids 48*, 693–708.

Ru, C. Q., X. Mao, and M. Epstein (1998). Electric-field induced interfacial cracking in multilayer electrostrictive actuators. *Journal of the Mechanics and Physics of Solids 46*, 1301–1318.

Schneider, G. A. (2007). Influence of electric field and mechanical stresses on the fracture of ferroelectrics. *Annual Review of Materials Research 37*, 491–538.

Schneider, G. A., F. Felten, and R. M. McMeeking (2003). The electrical potential difference across cracks in PZT measured by Kelvin Probe Microscopy and the implications for fracture. *Acta Materialia 51*(8), 2235–2241.

Schneider, G. A. and V. Heyer (1999). Influence of the electric field on vickers indentation crack growth in BaTiO3. *Journal of the European Ceramic Society 19*(6-7), 1299–1306.

Schrade, D., R. Mueller, B. X. Xu, and D. Gross (2007). Domain evolution in ferroelectric materials: A continuum phase field model and finite element implementation. *Computer Methods in Applied Mechanics and Engineering 196*(41-44), 4365–4374.

Sekerka, R. F. (2004). Morphology: from sharp interface to phase field models. *Journal of Crystal Growth 264*(4), 530–540.

Sheng, J. S. and C. M. Landis (2007). Toughening due to domain switching in single crystal ferroelectric materials. *International Journal of Fracture 143*(2), 161–175.

Shieh, J., J. E. Huber, and N. A. Fleck (2006). Fatigue crack growth in ferroelectrics under electrical loading. *Journal of the European Ceramic Society 26*, 95–109.

Shindo, Y., H. Murakami, K. Horiguchi, and F. Narita (2002). Evaluation of electric fracture properties of piezoelectric ceramics using the finite element and single-edge precracked-beam methods. *Journal of the American Ceramic Society 85*(5), 1243–1248.

Shu, Y. C. and K. Bhattacharya (2001). Domain patterns and macroscopic behaviour of ferroelectric materials. *Philosophical Magazine B 81*(12), 2021–2054.

Song, Y. C., A. K. Soh, and Y. Ni (2007). Phase field simulation of crack tip domain switching in ferroelectrics. *J. Phys. D: Appl. Phys. 40*(4), 1175–1182.

Steinbach, I. (2009). Phase-field models in materials science. *Modelling and Simulation in Materials Science and Engineering 17*(7).

Stemmer, S., S. K. Streiffer, F. Ernst, and M. Ruhle (1995). Atomistic structure of 90-degrees domain-walls in ferroelectric PbTiO3 thin-films. *Philosophical Magazine 71*(3), 713–724.

Su, Y. and C. M. Landis (2007). Continuum thermodynamics of ferroelectric domain evolution: Theory, finite element implementation, and application to domain wall pinning. *Journal of the Mechanics and Physics of Solids 55*(2), 280–305.

Sukumar, N., D. J. Srolovitz, T. J. Baker, and J. H. Prevost (2003). Brittle fracture in polycrystalline microstructures with the extended finite element method. *International Journal for Numerical Methods in Engineering 56*(14), 2015–2037.

Sun, C. T. and S. B. Park (2000). Measuring fracture toughness of piezoceramics by vickers indentation under the influence of electric fields. *Ferroelectrics 248*(1-4), 79–95.

Suo, Z. (1991). Mechanics concepts for failure in ferroelectric ceramics. Volume 24, pp. 1–6.

Suo, Z. (1993). Models for breakdown-resistant dielectric and ferroelectric ceramics. *Journal of the Mechanics and Physics of Solids 41*, 1155–1176.

Tieresten, H. F. (1969). *Linear piezoelectric plate vibrations*. Plenum Press.

Tobin, A. G. and Y. E. Pak (1993). Effects of electric fields on fracture behavior of pzt ceramics. *Proc. SPIE Smart Struct. Mater 1916*, 78–86.

Uchino, K. and A. Furuta (1992). Destruction mechanism of multilayer ceramic actuators. In M. Liu and A. Safari and A. Kingon And G. Haertling (Ed.), *ISAF 92 : Proceedings of the 8th IEEE International Symposium on Applications of Ferroelectrics*, pp. 195–198.

Uchino, K. and S. Takahashi (1996). Multilayer ceramic actuators. *Current Opinion in Solid State and Materials Science 1*, 698–705.

Vendik, O. G. and S. P. Zubko (2000). Ferroelectric phase transition and maximum dielectric permittivity of displacement type ferroelectrics ($Ba_xSr_{1-x}TiO_3$). *Journal of Applied Physics 88*, 5343–5350.

Verhoosel, C. V. and M. A. Gutierrez (2009). Modelling inter- and transgranular fracture in piezoelectric polycrystals. *Engineering Fracture Mechanics 76*(6), 742–760.

Wang, H. Y. and R. N. Singh (1997). Crack propagation in piezoelectric ceramics: Effects of applied electric fields. *Journal of Applied Physics 81*(11), 7471–7479.

Wang, J. and M. Kamlah (2009). Three-dimensional finite element modeling of polarization switching in a ferroelectric single domain with an impermeable notch. *Smart Materials and Structures 18*, 104008.

Wang, J. and M. Kamlah (2010). Effect of electrical boundary conditions on the polarization distribution around a crack embedded in a ferroelectric single domain. *Engineering Fracture Mechanics 77*(18), 3658–3669.

Wang, J. and C. M. Landis (2006). Effects of in-plane electric fields on the toughening behavior of ferroelectric ceramics. *Journal of Mechanics of Materials and Structures 1*(6), 1075–1095.

Wang, J. and T. Y. Zhang (2007). Phase field simulations of polarization switching-induced toughening in ferroelectric ceramics. *Acta Materialia 55*(7), 2465–2477.

Wang, X. (2005). *Phase field models and simulations of vesicle bio-membranes.* Ph. D. thesis, Pennsylvania State University.

Wang, Y. L., A. K. Tagantsev, D. Damjanovic, N. Setter, V. K. Yarmarkin, A. I. Sokolov, and I. A. Lukyanchuk (2007). Landau thermodynamic potential for BaTiO3. *Journal of Applied Physics 101*, 104115.

Westrain, I., W. S. Oates, D. C. Lupascu, J. Roedel, and C. S. Lynch (2007). Mechanism of electric fatigue crack growth in lead zirconate titanate. *Acta Materialia 55*, 301–312.

Westram, I., D. Lupascu, J. Roedel, B. Laskewitz, and M. Kamlah (2007). Electric-field-induced crack initiation from a notch in a ferroelectric ceramic. *Journal of the American Ceramic Society 90*, 2849–2854.

Winzer, S. R., N. Shankar, and A. P. Ritter (1989). Designing cofired multilayer electrostrictive actuators for reliability. *Journal of the American Ceramic Society 72*, 2246–2257.

Xu, B. X., D. Schrade, D. Gross, and R. Mueller (2010). Phase field simulation of domain structures in cracked ferroelectrics. *International Journal of Fracture 165*, 163–173.

Xu, B. X., D. Schrade, R. Mueller, and D. Gross (2009). Micromechanical analysis of ferroelectric structures by a phase field method. *Computational Materials Science 45*(3), 832–836.

Xu, X. P. and A. Needleman (1994). Numerical simulations of fast crack-growth in brittle solids. *Journal of the Mechanics and Physics of Solids 42*(9), 1397–1434.

Yang, L. and K. Dayal (2011a). Effect of lattice orientation, surface modulation, and applied fields on free-surface domain structure in ferroelectrics. *Acta Materialia 59*(17), 6594–6603.

Yang, L. and K. Dayal (2011b). Microstructure and stray electric fields at surface cracks in ferroelectrics. *Submitted for publication*.

Yang, W. and Z. Suo (1994). Cracking In Ceramic Actuators Caused By Electrostriction. *Journal of the Mechanics and Physics of Solids 42*, 649–663.

Yang, W. and T. Zhu (1998). Switch-toughening of ferroelectrics subjected to electric fields. *Journal of the Mechanics and Physics of Solids 46*(2), 291–311.

Ye, R. Q. and L. H. He (2001). Electric field and stresses concentrations at the edge of parallel electrodes in piezoelectric ceramics. *International Journal of Solids and Structures 38*, 6941–6951.

Zhang, T. Y. and C. F. Gao (2004). Fracture behaviors of piezoelectric materials. *Theoretical and Applied Fracture Mechanics 41*(1-3), 339–379.

Zhang, T.-Y., G. Liu, T. Wang, and P. Tong (2007). Application of the concepts of fracture mechanics to the failure of conductive cracks in piezoelectric ceramics. *Engineering Fracture Mechanics 74*(7), 1160–1173.

Zhang, T. Y., G. N. Liu, and Y. Wang (2004). Failure behavior and failure criterion of conductive cracks (deep notches) in piezoelectric ceramics II: experimental verification. *Acta Materialia 52*, 2025–2035.

Zhang, T. Y., T. H. Wang, and M. H. Zhao (2003). Failure behavior and failure criterion of conductive cracks (deep notches) in thermally depoled PZT-4 ceramics. *Acta Materialia 51*(16), 4881–4895.

Zhang, W. and K. Bhattacharya (2005a). A computational model of ferroelectric domains. part i: model formulation and domain switching. *Acta Materialia 53*(1), 185–198.

Zhang, W. and K. Bhattacharya (2005b). A computational model of ferroelectric domains. part ii: grain boundaries and defect pinning. *Acta Materialia 53*(1), 199–209.

Zhao, X. J., B. Liu, and D. N. Fang (2010). Study on electroelastic field concentration around the electrode tip in multilayer ferroelectric actuators of two designs and their optimizations. *International Journal of Plasticity 26*, 533–548.

Zhu, T. and W. Yang (1997). Toughness variation of ferroelectrics by polarization switch under non-uniform electric field. *Acta Materialia 45*(11), 4695–4702.

Zhu, T. and W. Yang (1999). Fatigue crack growth in ferroelectrics driven by cyclic electric loading. *Journal of the Mechanics and Physics of Solids 47*(1), 81–97.

Appendix A

Paper # 1: "Phase-field modeling of the coupled microstructure and fracture evolution in ferroelectric single crystals"

ATTENTION ¡

Abdollahi, A., Arias, I. *Phase-field modeling of the coupled microstructure and fracture evolution in ferroelectric single crystals* Acta Materialia Volume 59, Issue 12, July 2011, P. 4733–4746

doi:10.1016/j.actamat.2011.03.030

Pages 86 to 100 of the thesis are available at the editor's web

http://www.sciencedirect.com/science/article/pii/S1359645411001777

Appendix B

Paper # 2: "Phase-field modeling of crack propagation in piezoelectric and ferroelectric materials with different electro-mechanical crack conditions"

ATTENTION¡

Abdollahi, A., Arias, *I. Phase-field modeling of crack propagation in piezoelectric and ferroelectric materials with different electro-mechanical crack conditions***.** Journal of the Mechanics and Physics of Solids Vol. 60, # 12, December 2012, P. 2100–2126

doi:10.1016/j.jmps.2012.06.014

Pages 102 to 130 of the thesis are available at the editor's web

http://www.sciencedirect.com/science/article/pii/S0022509612001354

Appendix C

Paper # 3: "Phase-field simulation of anisotropic crack propagation in ferroelectric single crystals: effect of microstructure on the fracture process"

ATTENTION ¡

Abdollahi, A., Arias, I. *Phase-field simulation of anisotropic crack propagation in ferroelectric single crystals: effect of microstructure on the fracture process*
Modelling and Simulation in Materials Science and Engineering
Vol. 19, P. 1-13

doi:10.1088/0965-0393/19/7/074010

Pages 131 to 146 of the thesis are available at the editor's web

http://iopscience.iop.org/0965-0393/19/7/074010

Appendix D

Paper # 4: "Crack initiation patterns at electrode edges in multilayer ferroelectric actuators"

ATTENTION ¡

Abdollahi, A., Arias, I. ***Crack initiation patterns at electrode edges in multilayer ferroelectric actuators.*** Smart Materials and Structures 2012, Vol 21, #9, 094011, 10 p.

doi:10.1088/0964-1726/21/9/094011

Pages 148 to 159 of the thesis are available at the editor's web

http://iopscience.iop.org/0964-1726/21/9/094011

Appendix E

Paper # 5: "Numerical simulation of intergranular and transgranular crack propagation in ferroelectric polycrystals"

ATTENTION ¡

Abdollahi, A., Arias, I. *Numerical simulation of intergranular and transgranular crack propagation in ferroelectric polycrystals* International Journal of Fracture. March 2012, Volume 174, #1, pp 3-15

doi: 10.1007/s10704-011-9664-0

Pages 161 to 174 of the thesis are available at the editor's web

http://link.springer.com/article/10.1007%2Fs10704-011-9664-0